1 of 1

NASA CONTRACTOR
REPORT

NASA CR-61365

RESULTS OF A STUDY OF MACH NUMBER AND REYNOLDS NUMBER EFFECTS ON THE CROSSFLOW DRAG CHARACTERISTICS OF OGIVE-CYLINDERS AND OGIVE-CYLINDER-FRUSTUM-CYLINDERS AT ANGLES OF ATTACK TO 30 DEGREES

By J. E. Foley
Chrysler Corporation
Space Division
Huntsville, Alabama

October 22, 1971

Prepared for

NASA-GEORGE C. MARSHALL SPACE FLIGHT CENTER
Marshall Space Flight Center, Alabama 35812

TECHNICAL REPORT STANDARD TITLE PAGE

1. REPORT NO.	2. GOVERNMENT ACCESSION NO.	3. RECIPIENT'S CATALOG NO.
NASA CR-61365		

4. TITLE AND SUBTITLE

RESULTS OF A STUDY OF MACH NUMBER AND REYNOLDS NUMBER EFFECTS ON THE CROSSFLOW DRAG CHARACTERISTICS OF OGIVE-CYLINDERS AND OGIVE-CYLINDER-FRUSTUM-CYLINDERS AT ANGLES OF ATTACK TO 30 DEGREES

5. REPORT DATE: October 22, 1971

6. PERFORMING ORGANIZATION CODE:

8. PERFORMING ORGANIZATION REPORT #: TN-AP-71-527

7. Author(s): by J. E. Foley

9. PERFORMING ORGANIZATION NAME AND ADDRESS

Chrysler Corporation Space Division
Huntsville, Alabama

10. WORK UNIT NO.:

11. CONTRACT OR GRANT NO.: NAS 8-21152

13. TYPE OF REPORT & PERIOD COVERED: CONTRACTOR REPORT

12. SPONSORING AGENCY NAME AND ADDRESS

NASA
Washington, D. C.

14. SPONSORING AGENCY CODE:

15. SUPPLEMENTARY NOTES

16. ABSTRACT

An analysis has been made to determine the effects of Mach number and Reynolds number on the local and total crossflow drag characteristics of ogive-cylinders and ogive-cylinder-frustum-cylinders at angles of attack to 30 degrees. The analysis is based on force data obtained in the MSFC 14 in. TWT and the LTV 4 ft. HSWT, and pressure data obtained in the MSFC 14 in. TWT, at Mach numbers 014, 0.8, 1.2, and 2.0, and a wide range of Reynolds numbers. Results indicate that the "streamwise" Reynolds number, $VD/\nu \sin\alpha$, is an important correlation parameter in the subcritical Reynolds number range at imcompressible speeds and that the crossflow Mach number correlates compressibility effects.

17. KEY WORDS

18. DISTRIBUTION STATEMENT

Unclassified-Unlimited

E. D. Geissler
Dir, Aero-Astrodynamics Lab, MSFC

19. SECURITY CLASSIF. (of this report)	20. SECURITY CLASSIF. (of this page)	21. NO. OF PAGES	22. PRICE
Unclassified	Unclassified	68	$ 3.00

MSFC - Form 3292 (May 1969)

FOREWORD

This work was accomplished for the Marshall Space Flight Center under Contract No. NAS 8-21152, Subcontract No. LTV Purchase Order P-451008-AER.

The present study is a part of the overall "Non-Linear-Lift" research program being conducted by MSFC to determine scale effects on the aerodynamic characteristics of bodies of revolution at large angles of attack.

TABLE OF CONTENTS

LIST OF ILLUSTRATIONS

LIST OF ILLUSTRATIONS (continued)

SYMBOLS AND NOMENCLATURE

A_{Ref}	Reference area, $\pi D^2/4$
A_{Plan}	Planform area
c_{d_c}	Local crossflow drag coefficient, $\frac{\text{local crossflow drag per unit length}}{q \sin^2\alpha \, d}$
C_{D_C}	Total crossflow drag coefficient, $\frac{\text{total crossflow drag}}{q \sin^2\alpha \, A_{Plan}}$
C_N	Total normal force coefficient, $\frac{\text{normal force}}{q \, A_{Ref}}$
C_N'	Local normal force coefficient, $\partial C_N'/\partial(X/D)$
C_{N_α}'	Local normal force slope, $\partial C_N'/\partial\alpha$
C_p	Pressure coefficient, $\frac{P - P_\infty}{q}$
CP/D	Center of pressure
d	Local body diameter
D	Maximum body diameter
M	Free-stream Mach number
M_C	Crossflow Mach number
P	Static pressure
P_∞	Free-stream static pressure
q	Free-stream dynamic pressure
Re_C	Crossflow Reynolds number, $\frac{VD \sin\alpha}{\nu}$
Re_D	Free-stream Reynolds number, $\frac{VD}{\nu}$
Re_S	Streamwise Reynolds number, $\frac{VD}{\nu \sin\alpha}$
V	Free-stream velocity
X	Model axial station, measured from nose vertex

X_s	Axial location of initial cross-flow separation
α	Angle of attack
θ	Meridian angle, measured from windward plane of symmetry
ν	Kinematic viscosity
ϕ_m	Model roll angle

INTRODUCTION

The non-linear variations of the force characteristics of slender bodies of revolution with angle of attack have long been recognized to be primarily due to the effects of boundary layer separation induced by the crossflow. Munk[1] (1924) first pointed out a useful analogy between the development of the crossflow along a body of revolution at angle of attack and the development of the crossflow about a two-dimensional circular cylinder impulsively started from rest. This analogy is based on a simplified one-dimensional approach to the flow over a body of revolution at angle of attack, as illustrated in figure 1. A plane lamina of air, perpendicular to the axis of the body, is considered to be moving with constant velocity in the stream direction. This lamina sees the body as a segment of a circular cylinder, suddenly introduced as the lamina passes the nose of the body, and moving in the plane of the lamina at a velocity $V\sin\alpha$. Neglecting the effect of the changing cylinder radius at the nose, this situation is identical to the classical flow about a two-dimensional circular cylinder impulsively started from rest to a velocity $V\sin\alpha$, with the crossflow distance $X/D \tan\alpha$ for the body of revolution being equivalent to the distance $S/D = V\sin\alpha\ \Delta t/D$ traveled by the impulsively started cylinder. The experimentally determined flow about the impulsively started cylinder is described by Goldstein[2] for a range of Reynolds numbers as being characterized by the symmetrical development of a pair of vortices on the lee side of the cylinder, fed by vortex sheets emanating from the point of boundary layer separation on the cylinder. This flow is illustrated in figure 1, at various stages of development, as applied to the case of the body of revolution at angle of attack.

The above description of the crossflow phenomenon has been exploited theoretically and empirically by many investigators (e.g. references 3 through 7) in the development of methods to predict the resulting forces on bodies of revolution at angle of attack. The empirical methods generally consist of adding to the predicted local potential normal force distribution, which accounts for the forces generated by the nose, a local crossflow drag coefficient determined from impulsively-started and/or steady-state experimental drag data for two-dimensional circular cylinders. Theoretical methods utilize a "lumped" vorticity approximation for the vortices in a "slender body" potential flow field. The methods have met with various degrees of success but none are capable of accurate predictions over a practical range of Mach numbers, Reynolds numbers and body shapes.

A basic shortcoming of previous studies has been a lack of systematic experimental data on the effect of these variables. In an attempt to fill this void, the Marshall Space Flight Center (MSFC) instituted a "Non-Linear-Lift" research program to experimentally define the effects of Mach number, Reynolds number and body geometry on the flow about bodies of revolution

at angle of attack. The program consists of force, pressure, surface flow visualization and flow field survey tests conducted in the MSFC 14 in. TWT and LTV 4 ft. HSWT facilities on three different configurations over a wide range of Mach and Reynolds numbers.

This report is primarily concerned with a crossflow drag analysis of pressure data obtained on two configurations (an ogive/cylinder and an ogive/cylinder/frustum/cylinder) in the MSFC 14 in. TWT and of the force data obtained on these configurations in both the MSFC 14 in. TWT and the LTV 4 ft. HSWT at Mach numbers 0.4, 0.8, 1.2 and 2.0.

ACKNOWLEDGMENT

The author wishes to acknowledge the cooperation of P. Ramsey and J. Weaver of MSFC in making available related data and their general support of the objectives of this study. LTV HSWT test engineers were also very helpful in identifying the cause of certain data anomalies and provided additional data to resolve these discrepancies.

CONFIGURATIONS, MODELS, TESTS

The three configurations being investiaged in the MSFC "Non-Linear-Lift" research program are illustrated in figure 2. They consist of a simple ogive-cylinder (O/C), an ogive-cylinder-frustum-cylinder (O/C/F/C) and a typical Saturn V configuration.

One-half in. and one in. diameter force models of each configuration were tested in the MSFC 14 in. TWT and two and four in. diameter models were tested in the LTV 4 ft. HSWT. Tests were conducted in both facilities at Mach numbers 0.4, 0.8, 1.2, 2.0, 3.0, 4.0 and 5.0, at angles of attack to approximately 30° and at the maximum and minimum Reynolds number capabilities of the facilities. The resulting Reynolds number ranges are illustrated in the M/Re_D chart of figure 3. Details of the LTV models, test procedures and the basic data are reported in reference 8.

One-half in. and one in. diameter pressure models of the O/C and O/C/F/C configurations were tested in the MSFC 14 in. TWT at Mach numbers 0.4, 0.8, 1.2 and 2.0, at nominal angles of attack of 0, 5, 10, 15, 20 and 25°, and at the maximum and minimum Reynolds number conditions. The M/Re_D conditions for the pressure tests are also illustrated in figure 3. The pressure models were instrumented with a high density orifice array in order to obtain the required data in a practical amount of wind tunnel occupancy time. The orifice arrays generally consisted of seven longitudinal rows of orifices at 15° increments of meridional angle in one quadrant and two rows of orifices in an adjacent quadrant as illustrated in the following figure. The model was tested in roll positions of 0° and 90°, and the data transposed and combined (assuming symmetrical flow) to give the meridional distribution shown. Details of these models, test procedures, and resulting data are reported in reference 9.

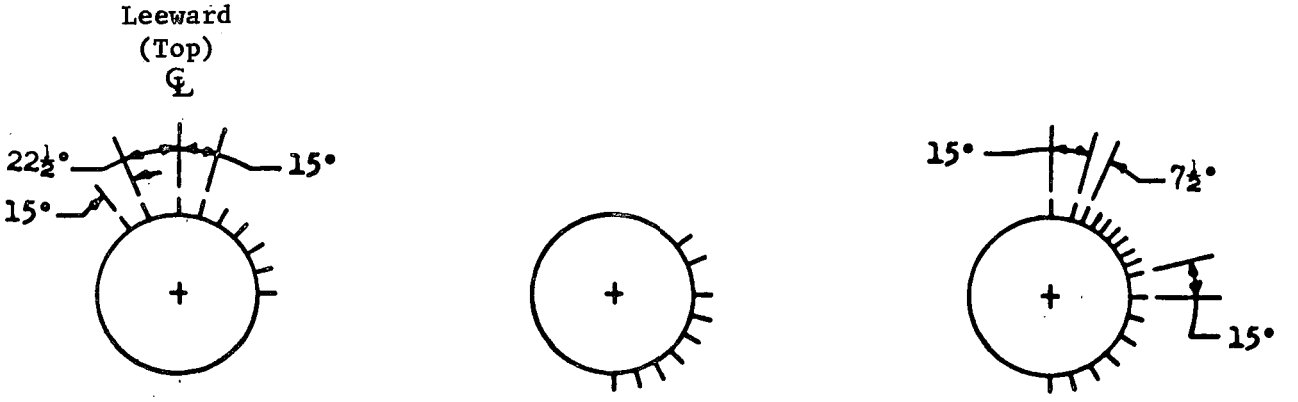

Orifice Array at $\phi_m = 0$

Orifice Array at $\phi_m = 90°$

Combined & Transposed Orifice Array

FORCE DATA AND ANALYSIS

Force data from the MSFC and LTV tests were provided for use in this analysis as aerodynamic coefficients C_N and CP/D, at angles of attack of 5, 10, 15, 20, 25 and 30° for each configuration at all of the Mach/Reynolds number conditions tested. This data had been corrected for apparent flow angularities by shifting the measured angles of attack such that $C_N = 0$ at $\alpha = 0$. These data for the O/C and O/C/F/C configurations at M = 0.4, 0.8, 1.2, and 2.0 are shown in figures 4 and 5.

Comparison of the corrected data with the basic data from the LTV test (reference 8), however, showed that the flow angularity corrections were excessive at Mach number 0.4. This is illustrated in figure 4(a) where both the corrected and the basic LTV data are shown for the O/C configuration. The maximum flow angularity corrections for M = 0.4 were on the order of 3° and cannot realistically be attributed to tunnel flow. The basic data also showed erratic trends with free stream Reynolds number at all angles of attack, which further increased the concern for accuracy of the data. These data anomalies were discussed with LTV test engineers who indicated that the probable cause was a result of "amplifier lag" in the data system in use at the time, and aggravated by low balance outputs at Mach number 0.4.

The LTV test program at Mach numbers 0.4 and 0.8 was recently rerun, reference 21, using an improved data system and balances more consistent with the model loads at these conditions. A preliminary evaluation of this data showed that the indicated flow angularities were reduced to the order of 0.25° except for the O/C/F/C configuration at Mach number 0.4 which ranged to 0.7° for the 2 inch diameter model. The erratic trends of normal force vs. Reynolds number at M = 0.4 were largely eliminated for the ogive-cylinder and Saturn V configurations. The O/C/F/C configuration at Mach number 0.4, showed unusual trends at low angles of attack for the 2 inch diameter model which were not present in the original data. At Mach number 0.8, the rerun data for the O/C and O/C/F/C compared very well with the original test, but rerun data for the Saturn V configuration was approximately 10% lower than the original data.

The rerun data was not available in time to be included in this analysis, and due to the anomalies in the original M = 0.4 data at high Reynolds numbers (LTV), only the low Reynolds number (MSFC) data is considered in the analysis of the force data at M = 0.4. The data at Mach number 0.8 and above is apparently free of significant data anomalies, at least for the O/C and O/C/F/C configurations of interest here, and is included.

Side Force Data and Flow Asymmetries

Although a detailed consideration of the side force data on the subject configurations is beyond the scope of this report, it should be noted that significant flow asymmetries and resultant side forces were observed at certain conditions in both the LTV force tests and the MSFC pressure tests. The side force data from the LTV tests at Mach numbers 0.4 and 0.8 showed large side forces at some Reynolds numbers ($C_{y_{Max}}$ on the order of .5 to 1.0) which developed at angles of attack above approximately 20°. Asymmetries in the MSFC pressure data were also observed for M = 0.4 and 0.8, and to a lesser extent at M = 1.2, at angles of attack of 15° and above. The pressure data asymmetries are thought to be related to the pressure orifice arrangement although there are indications that flow asymmetries at these conditions could be expected, independent of the particular orifice arrangement. The pressure asymmetries are discussed in greater detail in a later section.

A detailed investigation of the side forces on bodies of revolution with ogive noses has recently been reported by Pick (reference 10) at Mach numbers from 0.5 to 1.1. It was found that large side forces were developed on these bodies at angles of attack also above 20°. The magnitude of the side force was a strong function of nose shape and Mach number, decreasing with increasing Mach number or with increasing nose bluntness. The direction of the side force, once it developed, varied randomly with model roll angle and was attributed to small variations in model geometry.

The development of the flow asymmetries causing the side forces can be related to asymmetrical flow phenomena on two dimensional cylinders in transverse incompressible flow using the impulsively started cylinder analogy described in the introduction. According to Sarpkaya's experiments (reference 7) on impulsively started cylinders at Reynolds numbers from 10^4 to 10^5, the symmetrical development of vortices behind the cylinder continues for a non-dimensional time increment of $Vt/D \cong 4$ at which time asymmetries in the flow pattern begin to develop. Based on the impulse analogy this would correspond to $\frac{X}{D} \tan\alpha = 4$ where asymmetries would first be expected on a constant diameter body of revolution at angle of attack and for a 10 caliber body (X/D = 10) would indicate an angle of attack of $\alpha = \tan^{-1} 0.4 = 24°$ for first flow asymmetry. This is approximately the angle of attack at which side forces are first observed on these bodies of revolution. The agreement between the predicted angles of attack for first flow asymmetry based on Sarpkaya's data for impulsive cylinders and the actual values observed is remarkable considering the differences in the flow situations.

The development of the flow asymmetries found in experiments with impulsively started cylinders and slender bodies at angle of attack is consistent with the theoretical prediction that the location of a pair of symmetric vortices on the lee side of these bodies is unstable for anti-symmetrical disturbances (reference 2). It is probably this instability of vortex pairs which is the basic cause of the flow asymmetries and the "small" geometric irregularities (or other flow disturbances) simply act to trigger the instability.

Effect of Reynolds Number on Normal Force and Center of Pressure Characteristics

The data presented in figures 4 and 5 show some very significant influences of Reynolds number and Mach number on the characteristics of these configurations. The greatest effect of Reynolds number is observed for the O/C configuration at M = 0.4, even excluding the high Reynolds number LTV data. The normal force coefficients versus Reynolds number at the higher angles of attack exhibit all the features of the classical variation of drag coefficient with Reynolds number of two-dimensional circular cylinders in incompressible transverse flow (e.g. reference 2). There is a subcritical maximum associated with laminar boundary layer separation and a minimum value at a critical Reynolds number associated with transition of the boundary layer to turbulent flow. The subcritical maximum normal force coefficients are approximately twice the minimum values at the higher angles of attack.

The center of pressure for the O/C at M = 0.4 also shows large variations with Reynolds number. Largest CP/D variations occur at an angle of attack of 20° where the CP/D at subcritical Reynolds numbers is located at 5.5 calibers from the base, and moves forward to 6.9 calibers at the critical Reynolds number.

Data for the O/C at higher Mach numbers exhibit a decreasing effect of Reynolds number with increasing Mach number. At M = 2.0, significant Reynolds number effects are confined to angles of attack of 10 and 15° where the crossflow Mach number ($M_C = M \sin\alpha$) is .35 and .52 respectively. This is also consistent with circular cylinder data (references 11, 12) which show little effect of Reynolds number above M_C = 0.4 to 0.5.

Data for the ogive/cylinder/frustum/cylinder shown in figure 5 indicate very small effects of Reynolds number as compared with the ogive/cylinder configuration. This is due to the combination of (1) a small forward cylinder planform area which reduces the contribution of its crossflow drag to the total normal force, (2) the large, 25°, slope of the frustum which delays crossflow separation effects on the frustum to angles of attack above 25°, and (3) the relatively short aft cylinder length, with flow at the forward end controlled to a large extent by axial flow pressure distribution and a large potential carryover normal force from the frustum. These factors are illustrated later using the integrated pressure data from the MSFC pressure tests.

Correlation of O/C Normal Force Characteristics

Correlations of the O/C normal force data were made for the purpose of gaining some insight into the effects of Mach number and Reynolds number, and to develop correlation parameters for use in the analysis of the local normal force and pressure data. As indicated above, the M = 0.4 data shows the greatest sensitivity to Reynolds number. At this Mach number no compressibility effects should be present, and these data were thus used to isolate the effects of Reynolds number. The data was reduced to crossflow drag coefficients according to the equation.

$$C_{D_C} = \frac{C_N - C_{N_\alpha}\alpha}{\sin^2\alpha} \frac{A_{Ref.}}{A_{Plan}} \qquad (1)$$

The inviscid normal force slope, C_{N_α}, was taken to be the slender body theory value of 2.0 rad^{-1} and was in close agreement with the experimental data.

According to Allens theory (reference 3), the crossflow drag coefficient at incompressible speeds should be a function of the crossflow Reynolds number Re_C

$$Re_C = \frac{VD\sin\alpha}{\nu}$$

A correlation of the M = 0.4, O/C crossflow drag data with crossflow Reynolds number, C_{D_C} (Re_C) is shown in figure 6 for various values of free stream Reynolds numbers based on diameter, Re_D, and for angles of attack of 10, 15, 20, 25 and 30°. This correlation was developed using the normal force data represented by the faired (solid) curves of figure 4 (a), for Re_D between 10^5 and 4 x 10^5. The lack of any correlation of crossflow drag with crossflow Reynolds number in figure 6 is obvious.

It was pointed out by Schindel (reference 6) that body lengths parallel to the free stream (i.e. streamwise lengths) are approximations of particle paths, as indicated in the sketch below, and should represent appropriate lengths for determination of boundary layer transition. A Reynolds number based on a characteristic body length parallel to the freestream should therefore provide an approximate correlation of boundary layer transition and its effect on the crossflow drag characteristics. This hypothesis was tested by correlating the O/C crossflow drag data at M = 0.4 as a function of a "streamwise" Reynolds number, $Re_S = \frac{VD}{\nu \sin\alpha}$. This Reynolds number is based on the streamwise length of the cylindrical portion of body, $D/\sin\alpha$. The correlation is shown in figure 7 and it is seen that the streamwise Reynolds number does in fact correlate the crossflow drag data quite well.

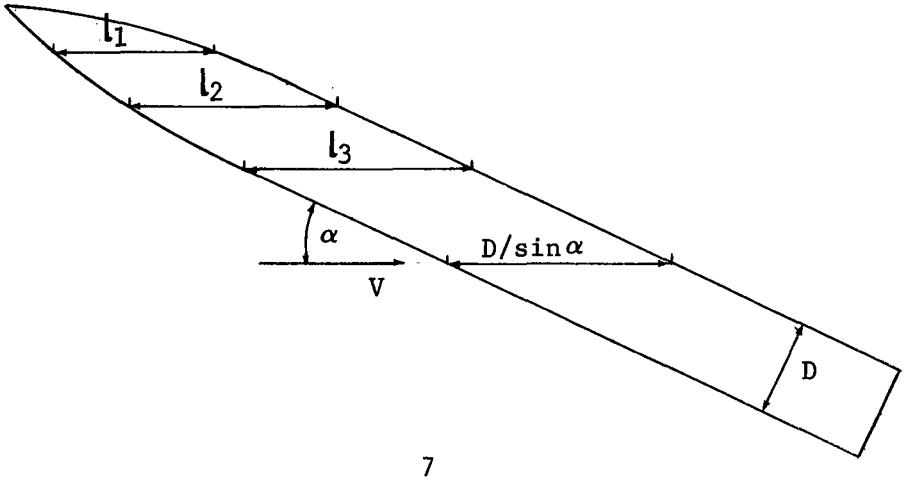

The effect of compressibility on crossflow drag coefficient was investigated by plotting the data vs crossflow Mach number at two free stream Reynolds numbers, $Re_D = 2 \times 10^5$ and 5×10^6, representative of the minimum and maximum values of the test range. The results, shown in figure 8, were developed from $C_N(\alpha)$ data for each free stream Mach number and Reynolds number, at angles of attack from 10 to 30^o. The high Reynolds number (LTV) data at M = 0.4 was excluded for the previously stated reasons.

Crossflow Mach number correlates the compressibility effects on crossflow drag coefficients very well for the high Reynolds number data ($Re_D = 5 \times 10^6$) at $M_\infty = 0.8$ and above. These data are in the supercritical Reynolds number range and should be relatively insensitive to Reynolds number. The low Reynolds number data ($Re_D = 2 \times 10^5$) is not correlated by crossflow Mach number at M = 0.4 and 0.8. This data is in the subcritical Reynolds number range where the large effects of Reynolds number were found to be correlated by the "streamwise" Reynolds number, Re_s, and an improved correlation of compressibility effects could be expected for subcritical Reynolds numbers if it were developed for constant values of the streamwise Reynolds number.

The streamwise Reynolds number cannot be considered to be a universal correlation parameter, of course, even at incompressible speeds, as it does not consider the effects of nose shape, is not appropriate at low angles of attack where $Re_s \Rightarrow \infty$, and does not consider the effects of finite cylinder length which are known to be quite significant an angles of attack approaching 90^o. The above correlations do, however, show the superiority of the streamwise Reynolds number over the crossflow Reynolds number as a correlation parameter and should lead to an improved understanding of the effects of Reynolds number on the crossflow separation phenomena.

Although direct measurements of the actual state of the boundary layer were not available for the conditions of these tests, the crossflow drag correlations infer that for the angle of attack range $20 \leq \alpha \leq 30^o$, the MSFC test conditions corresponded to a fully laminar boundary layer at the lowest Reynolds numbers and that transition occurred on the body at the highest Reynolds numbers. Also, a preliminary evaluation of the rerun LTV data infers a fully turbulent boundary layer at the higher Reynolds number conditions.

PRESSURE DATA

The pressure data, on which the local crossflow drag analysis is based, was obtained on models with high orifice density in order to obtain the large amount of data required in a practical amount of wind tunnel occupancy time. The models were basically instrumented with 7 longitudinal rows of orifices at 15° azimuthal increments in one quadrant and 2 longitudinal rows of orifices at intermediate azimuth angles in an adjacent quadrant as described on page 3. This arrangement was selected based on the assumption of symmetrical flow and no orifice effects on the resulting pressure data such that the data at model roll positions of 0 and 90° could be transposed and combined to give a detailed pressure distribution on one side of the model.

The pressure data and the local and total force and moment characteristics resulting from integrating the pressure distributions over the surface of the models are reported in their entirety in reference 9. Inspection of these data revealed large asymmetries in the pressure data and poor correlation of integrated pressure data with the results of the force test for the 0/C configuration (figure 4) at the lower Mach numbers and higher angles of attack. Limited surface flow visualization tests at M = 0.4 utilizing the actual one in. dia. ogive/cylinder pressure model confirmed the existence of severe flow asymmetries at sub-critical Reynolds number, apparently induced by the pressure orifices.

Effect of Pressure Orifices on Total Normal Force

A comparison of the force and integrated pressure data as a function of Reynolds number is illustrated in figure 9 for the ogive/cylinder configuration. In general, the pressure models indicate lower normal force at sub-critical Reynolds numbers and higher normal forces at supercritical Reynolds numbers as compared with the force model data. This type of result is very similar to the effect of roughness on the drag characteristics of circular cylinders in transverse flow (reference 2) and indicates that the orifices on the pressure model acted as surface roughness elements. Agreement of force data with integrated pressure data for the 0/C/F/C configuration was good at all conditions indicating little effect of orifices for this configuration. This is consistant with the low sensitivity to Reynolds number for this configuration and is due to the geometry of the configuration as discussed on page 6.

Effect of Pressure Orifices on Surface Flow and Pressure Distributions

The effect of the orifices on the surface flow patterns at the conditions where pressure asymmetries were the greatest, i.e. the ogive/cylinder at M = 0.4, Re_D = .23 x 10^6, and 24.5° angle of attack, is illustrated in figure 10. The

clean (left) side of the model exhibits a laminar primary separation which is quite regular back to a model joint at station X/D = 4.45. The model joint causes a small perturbation in the separation line at the joint, followed by another perturbation at X/D ≅ 5.0. The second perturbation in the separation line appears to be accompanied by the discharge of the left vortex, as evidenced by the sudden change in the location and eventual disappearance of the secondary separation line associated with the left vortex. The separation line on the high orifice density (right) side indicates perturbations associated with the orifices at X/D between 1.0 and 2.0. At X/D between 2.0 and 5.0, there is an obvious interaction of the orifices with the secondary separation line. It is believed that these perturbations in the primary and secondary separation lines hindered the development of the right side vortex and resulted in lower normal forces being developed on the pressure model as compared with the force model at these conditions. It is also likely that the model joint precipitated the discharge of the left vortex, modifying the flow over the rear of the model and further affecting the correlation of the force and integrated pressure data.

The asymmetry in the pressure distributions on the lee side of the pressure model is illustrated in the pressure contours of figure 11 for the same conditions as above. Asymmetry develops at X/D between 2 and 3 and persists to varying degrees downstream of this region. The maximum pressure asymmetry ($\Delta C_p \cong 0.4$) occurs at X/D between 4 and 5 with the development of an intense low pressure cell on the left side (negative θ) of the model just prior to discharge of the left vortex. Poor development of the right vortex is evidenced by the flatter contours on the right side and generally higher pressure levels. The two regions of oil accumulation indicated in the top view of figure 10 and shown on the pressure contour in figure 11 appear to be directly related to the low pressure cells induced by the vortices and indicate a severe asymmetry in vortex positions. The closely spaced isobars at roll positions (ϕ) between 50 and 60°, aft of X/D = 2.5 on the right side of the model are associated with the secondary separation line.

The surface flow visualization pictures for M = 0.4 at Reynolds number $Re_D = .39 \times 10^6$ showed small asymmetries consistent with the small asymmetries in the pressure data at the higher Reynolds number. The O/C/F/C configuration at Mach number 0.4 showed comparable pressure asymmetries on the forward cylinder at the same Reynolds number, based on local diameter, as the ogive/cylinder model. The frustum and aft cylinder of the O/C/F/C generally showed smaller pressure asymmetries due to the predominantly inviscid influence of the 25° frustum.

Flow on the Lee Side of the O/C/F/C Configuration

A significant feature of the flow on the lee side of the O/C/F/C configuration is illustrated by the data of figure 12, where the leeward meridian pressure distributions are shown at 25° angle of attack for each Mach number and compared to the zero angle of attack pressure distributions. The maximum pressures associated with the lee side cylinder/frustum compression corner at 25° angle of attack are the same or higher than at zero angle of attack for all Mach numbers, and the extent of axial flow boundary layer separation at zero angle of attack for M = 1.2 and 2.0 is much diminished at 25° angle of attack. This illustrates how the vortex pair generated by the forebody induces a downflow toward the body in the leeward stagnation plane at high angle of attack, maintaining and accentuating the effect of the compression corner, and reducing the extent of axial separation through thinning of the boundary layer by outflow from the leeward stagnation line.

The location of the vortices at Mach number 0.8 can be seen in the Schlieren photograph of figure 13, taken at an angle of attack of 24.5° and Reynolds number $Re_D = 0.67 \times 10^6$. The center of the vortices appear as the dividing line between the dark and light regions above the body. An asymmetric vortex pair is indicated on the nose by the appearance of two distinct vortices, one originating on the ogive nose and one just aft of the ogive nose. This Schlieren was taken of the actual pressure model and the asymmetric forebody vortices are attributed to the asymmetric orifice array. The forward cylinder vortex pair is "released" from the body just aft of the frustum and is convected away in the free stream direction while a second pair of vortices is generated on the aft cylinder.

Surface flow for the above condition is visualized by the fluorescent oil flow photographs shown in figure 14. These pictures were taken using a model with a single row of dummy orifices in an investigation of orifice effects. The orifices are on the lee meridian in these pictures and no significant asymmetries are apparent here, although when the orifices were in the vicinity of the side meridian they did cause asymmetries in the region of the nose. The effect of the forebody vortices at 24.5° angle of attack is indicated by the strong induced outflow from the leeward meridian on the forward cylinder and frustum. The induced flow thins the boundary layer on the lee side, preventing axial flow separation and causing the high peak pressures in the cylinder/frustum compression corner.

The primary crossflow separation line (origin of the vortex feeding sheet) of the forebody begins at the model nose and is terminated on the frustum by axial flow separation induced by the adverse pressure gradient of the recompression on the aft cylinder. This termination of the feeding sheet "frees" the forebody vortices and allows them to be convected away from the body. The aft cylinder vortices are generated by a new primary crossflow separation which begins at approximately .75 calibers downstream of the frustum. This vortex pair grows rapidly in strength as evidenced by the strong outflow and secondary separation lines which develop between 1.0 and 1.5 calibers downstream of the frustum.

This vortex induced downflow has been recognized as a significant factor in determining the heating rates on the lee side of bodies at large angles of attack as similar effects have been found to persist to high supersonic Mach numbers. The strong compression noted above at the cylinder/frustum juncture on the lee side would indicate very high heating rates at this point and similar effects would be expected on any lee side protuberances under the influence of a similar vortex induced flow.

LOCAL CROSSFLOW DRAG CORRELATION

Although the pressure data was found to be significantly affected by the presence of the pressure orifices, it was felt that a correlation of this data on the basis of the local crossflow drag coefficients would be useful in determining the general effect of Mach number, Reynolds number and body geometry on the crossflow drag characteristics.

The local crossflow drag coefficient is defined as the difference between the total local normal force at angle of attack and the local normal force due to inviscid (potential) flow, nondimensionalized by the local diameter and crossflow dynamic pressure,

$$c_{d_c} = \frac{C'_N - C'_{N_\alpha}\alpha}{\sin^2\alpha} \frac{\pi D}{4d} \qquad (2)$$

The impulsively started cylinder analogy suggests that the local crossflow drag coefficients should be a function of the distance parameter $\frac{S}{D} = \frac{X}{D} \tan\alpha$,i.e. $c_{d_c} = c_{d_c}(\frac{X}{D} \tan\alpha)$. A modification to this analogy has been proposed to account for the fact that at low or moderate angle of attack the crossflow separation does not occur at the nose but at some distance aft of the nose depending on the nose shape, angle of attack, Mach number and Reynolds number. This modified method suggests that the axial distance should be measured from the axial location of first crossflow separation, i.e. $c_{d_c} = c_{d_c}(\Delta\frac{X}{D} \tan\alpha)$ where $\Delta\frac{X}{D} = \frac{X}{D} - \frac{X}{D}_s$. It has also been suggested (references 13 and 14) that the crossflow drag can be correlated simply by X/D, based on limited results for specific configurations. The latter two correlations, i.e. $c_{d_c}(X/D)$ and $c_{d_c}(\Delta X/D \tan\alpha)$, are explored here in investigating the effects of Mach number, Reynolds number and configuration geometry on the local crossflow drag characteristics.

Local Inviscid Normal Force Distributions

The local inviscid normal force distributions, $C'_{N_\alpha}(X/D)$ used in the crossflow drag correlation were developed empirically from the experimental data at an angle of attack of 5°. This approach was taken as an expediency and because of the uncertainties involved in the application of the various theoretical methods to the body shapes and Mach numbers of interest.

The local normal force distributions at $\alpha = 5°$ for each of the four Reynolds numbers, for a given configuration and Mach number, were examined

and a curve faired through the data using theoretical results as a guide to the fairing. This procedure is illustrated in figure 15 where the $\alpha = 5^{o}$ normal force distributions for each Reynolds number and the resulting "inviscid" distributions are shown. The normal force data for the highest Reynolds number was weighted the most in arriving at the faired inviscid distribution.

A crossflow drag analysis was performed only for the aft cylinder of the O/C/F/C configuration. It was found that the forward cylinder characteristics were adequately described by the O/C alone, and that the local normal force characteristics of the frustum region were not amenable to a crossflow analysis, leaving only the aft cylinder characteristics to be evaluated by a crossflow drag correlation.

The total normal force characteristics of the frustum section would not be expected to be significantly affected by non-linearities due to angle of attack for the conditions of this test as the maximum angle of attack is essentially the same as the frustum angle, i.e. 25^{o}. This was found to be true for the integrated normal force on the frustum and also for the frustum plus carryover normal force, even though the local normal force distributions were highly sensitive to angle of attack. The sensitivity of the local normal force distributions in the frustum region is illustrated by the data in figure 16, showing the normal force distributions, C_N'/α, for the maximum Reynolds number condition at each Mach number. The distributions at $\alpha = 5^{o}$ are not at all similar to the higher angle of attack distributions. At $\alpha = 5^{o}$, the large negative values of local normal force just forward of the frustum at M = 1.2 and 1.96, and the high positive peaks for all Mach numbers at the cylinder/frustum compression corner are due to the effects of axial flow separation induced by the adverse longitudinal pressure gradient. The expansion and recompression region just aft of the frustum is also affected by axial flow separation and is very sensitive to angle of attack. The variations in normal force distributions at the higher angles of attack tend to become more uniform and actually are more representative of expected inviscid distributions. The forward and aft cylinders, in the regions not influenced by the frustum, show the typical effects of increasing non-linear normal force with angle of attack due to crossflow separation.

The integrated normal force coefficients for the frustum, the frustum plus carryover regions, and the total vehicle are shown versus angle of attack in figure 17. The frustum plus carryover region was arbitrarily taken as between X/D = 3.4 and 6.0 and includes the effects of axial flow separation forward and aft of the frustum. Both the frustum and frustum plus carryover normal force characteristics are very linear with angle of attack at all Mach numbers while the total vehicle characteristics are quite non-linear with angle of attack.

The "inviscid" normal force distributions used for the crossflow drag analysis of the O/C/F/C aft cylinder were determined in a manner similar to the ogive-cylinder and the resulting distributions are shown in figure 16.

Local Crossflow Drag Correlation, Ogive-Cylinder Configuration

The local crossflow drag coefficients, derived according to equation (2), are presented vs. model station for the O/C configuration in figure 18 at the minimum and maximum Reynolds numbers tested at each Mach number. Data are presented for nominal angles of attack of 5, 10, 15, 20 and 25 degrees. The actual values of angle of attack, corrected for sting deflection, were used in the computation of the crossflow drag coefficients and were generally within 1/2 degree of the nominal values. The crossflow drag coefficients are somewhat erratic due to orifice effects and tunnel disturbances and is particularly severe at $\alpha = 5^o$ due to small normal force coefficient increments, $(C_N - C_{N_\alpha}\alpha)$, being magnified by the $1/\sin^2\alpha$ term in computing c_{d_c}. The low angle of attack crossflow drag coefficients are also very sensitive to the assumed inviscid normal force distributions for the same reason, although it should be noted that a change in the inviscid normal force distribution, $\Delta C_{N_\alpha} = .11$, which would change c_{d_c} at $\alpha = 5^o$ by 1.0 would change c_{d_c} at $\alpha = 15^o$ by only .11 and by only .04 at $\alpha = 25^o$. The values of c_{d_c} at $\alpha = 5^o$ are generally reasonable levels and tend to confirm the adequacy of the empiric method used here to determine the inviscid local normal force distributions.

Figure 18 illustrates the typical build-up of crossflow drag coefficient with model station, although the location of initial build-up, the build-up rate, and the peak values are strong functions of the test variables. The local crossflow drag distributions at M = 0.4 indicate the largest influence of Reynolds number, as was the case with the total normal force characteristics discussed previously. At 25° angle of attack and minimum Reynolds number ($Re_D = .11 \times 10^6$), c_{d_c} reaches a peak value of 1.5 at X/D = 4.0 and approaches a "steady state" value of about 1.3, while for the maximum Reynolds number ($Re_D = .39 \times 10^6$), c_{d_c} reaches a peak value of only .57 at X/D = 5.0 and approaches a steady state value of approximately 0.5. The effect of angle of attack on the peak c_{d_c} at M = 0.4 is interesting in that the minimum Reynolds number data shows a peak c_{d_c} which increases with angle of attack while the peak c_{d_c} decreases with angle of attack for the maximum Reynolds number case.

The sensitivity of peak c_{d_c} to Reynolds number decreases with increasing Mach number and at M = 2.0, a peak c_{d_c} of 1.6 is representative for both the minimum and maximum Reynolds numbers at angles of attack of 15° and above. The value of the peak c_{d_c} was correlated as function of the streamwise Reynolds number, $Re_s = Re_D/\sin\alpha$, and the results are shown in figure 19 for M = 0.4 and 0.8 where Reynolds number effects are most significant. The streamwise Reynolds number correlates the data quite well and inspection of the data trends indicates that correlation on the basis of either free stream Reynolds number Re_D or crossflow Reynolds number $Re_D \sin\alpha$ would be much poorer. Comparison of the data for M = 0.4 and 0.8 indicates a relatively small effect of Mach number in this range. The maximum crossflow

Mach number for this data is $M_c = 0.34$ ($M = 0.8$, $\alpha = 25^o$), and is below the commonly accepted critical Mach number of 0.4 (reference 11) for circular cylinders. It should be noted, however, that Jones (reference 12) found a rather gradual increase in the drag coefficient of circular cylinders with increasing Mach number between 0.2 and 0.4 at $Re_D = 7.5 \times 10^6$. Similar effects of Mach number could be expected at lower Reynolds numbers and crossflow Mach number effects may be present in the high angle of attack data at $M = 0.8$.

The opposing effects of angle of attack on peak c_{d_c} at the minimum and maximum Reynolds numbers at $M = 0.4$, noted earlier, is seen to be associated with the "bucket" in the c_{d_c} (Re_s) curve. The maximum Reynolds number data, $Re_D = .39 \times 10^6$, approaches the bucket from the supercritical side with increasing angle of attack while the minimum Reynolds number data, $Re_D = .11 \times 10^6$ recedes from the bucket on the subcritical side. The axial location of the initial crossflow separation was derived from the c_{d_c} distributions such as those shown in figure 18, by fairing the data at each angle of attack and identifying the point where $c_{d_c} \Rightarrow 0$ as the location of initial crossflow separation. This approach yields a direct measure of the axial location for the onset of viscous (i.e. separation) effects. Jorgensen (reference 15) developed a method for determining the axial location of boundary layer separation using the surface pressure distributions and the same technique was applied by Tinling (reference 16). The vortex sheet must be rolled up, i.e. the vorticity must be concentrated in a core, and the resulting vortices must be of a sufficient strength before they will induce a measureable effect on the pressure distributions. The pressure distribution method is therefore not an accurate means of determining the location of the onset of viscous effects. Jorgensen's and Tinling's results indicate more aft separation locations particularly at low angle of attack and subsonic speeds.

The separation locations obtained above were used to develop a correlation of c_{d_c} as a function of $\frac{\Delta X}{D} \tan \alpha$, the correlation parameter inferred by the impulsive cylinder analogy. The data for $X_s(\alpha)$ in figure 20 showed no consistent effects of Reynolds number, therefore all the data has been faired into one curve for each Mach number. The faired $X_s(\alpha)$ curves were then used to replot the $c_{d_c}(X/D)$ data c_{d_c} ($\frac{\Delta X}{D} \tan \alpha$). These results are presented in figure 21 and it can be seen that the location of the peak c_{d_c} is correlated fairly well by $\frac{\Delta X}{D} \tan \alpha$, with the peak c_{d_c} generally occurring at $\frac{\Delta X}{D} \tan \alpha$ between 1.0 and 1.5.

Local Crossflow Drag Correlation, O/C/F/C Aft Cylinder

An analysis of the local crossflow drag coefficients on the aft cylinder of the O/C/F/C configuration was performed in the same manner as for the

ogive-cylinder configuration, and the resulting local crossflow drag coefficients are presented as a function of model station in figure 22. The data at the forward end of the aft cylinder is quite irregular and reflects the strong interaction of the axial flow and the crossflow in the expansion and recompression region behind the flare and, as discussed in a previous section, is best considered as a carryover of the "linear" frustum load.

At M = 0.4 and 0.8, the local crossflow drag at the minimum Reynolds number condition is still increasing rapidly at the aft end of the cylinder while the high Reynolds number data has reached a maximum and near steady state level over the last 2 to 3 calibers of the body. The maximum Reynolds number data is consistent with the surface flow visualization pictures at M = 0.8, $\alpha = 25^{o}$, shown in figure 14, which showed crossflow separation developing at about .75 caliber aft of the frustum, a subsequent rapid development of vortices, and uniform flow over the rear of the body. No flow visualization was available for the minimum Reynolds number cases and it can only be speculated that either the aft cylinder vortices are developing over a greater length or that a third pair of vortices are developing at the end of the body.

A correlation of the peak crossflow drag coefficients is presented in figure 23. At M = 0.4, the peak crossflow drag is again correlated by the streamwise Reynolds number and indicates a critical Reynolds number somewhat lower than the ogive-cylinder configuration. The cases where the local crossflow drag coefficient is still increasing at the end of the body (indicated by the vertical line beneath the symbol) seem to be associated with subcritical Reynolds numbers. At M = 0.8, the correlation of peak local crossflow drag is inconclusive although the high angle of attack data indicates peak values on the order of 1.0, independent of Reynolds number.

Location of the initial crossflow separation is shown in figure 24 and indicates less influence of angle of attack than the ogive-cylinder data. This is attributed to the frustum in acting as a blunt nose, tending to fix the location of crossflow separation.

Local crossflow drag is presented vs. the parameter $\Delta \frac{X}{D} \tan \alpha$ in figure 25 and yields a better crossflow drag correlation than X/D, with the exception of the low Reynolds number data at M = 0.4 and 0.8.

CONCLUSIONS

An analysis has been made of force and pressure data obtained on an ogive-cylinder and an ogive-cylinder-frustum-cylinder at Mach numbers 0.4, 0.8, 1.2, and 2.0 for a wide range of Reynolds numbers and angles of attack to 30°. This analysis was directed at establishing the effects of Reynolds number, Mach number and configuration on the crossflow drag characteristics of bodies of revolution at large angles of attack.

Some of the force and pressure data was found to have been adversely affected by test techniques used for the tests. The force data obtained at M = 0.4 in the LTV HSWT exhibited some extraneous trends which have been attributed to "amplifier-lag" in the data system, aggravated by low balance outputs at this test condition. These data have been re-run using an improved data system and balances sized for the low model loads at M = 0.4 and 0.8 but were not available in time to be included in this analysis.

The pressure data obtained in the MSFC 14 in. TWT was found to have been affected at low speeds by the asymmetrical, high orifice density of the pressure models. Severe flow asymmetries were found at the higher angles of attack and intermediate Reynolds numbers, particularly at M = 0.4 and 0.8, and are attributed in part to the asymmetrical orifice arrangement. Force data on "smooth" axisymmetric models have shown large side forces which were attributed to "small" random variations in geometry, but might more directly be attributed to the basic instability of the vortical flow field. The direction of the asymmetries appears to be controlled by "small" model irregularities and the angle of attack at which the asymmetries appears is decreased by "large" model irregularities, as represented by the orifices of the pressure model.

The large effects of Reynolds number and Mach number on the total normal force characteristics of the ogive-cylinder are similar to the classical effects of these parameters on the drag characteristics of two-dimensional circular cylinders. At low (subcritical) Reynolds number, these effects are correlated by a crossflow drag analysis in terms of a "streamwise" Reynolds number, $Re_D/\sin \alpha$, and the crossflow Mach number. At high (super-critical) Reynolds number, the normal forces appear to be independent of Reynolds number and the crossflow drag is correlated by crossflow Mach number alone. A local crossflow drag analysis for the ogive-cylinder generally indicated the applicability of the "impulsive cylinder" analogy in that the form of the local crossflow drag distribution is fairly well correlated by the "impulsive cylinder" distance parameter, $\left(\frac{X}{D} - \frac{Xs}{D}\right) \tan \alpha$.

The ogive-cylinder-frustum-cylinder total normal force characteristics were relatively insensitive to Reynolds number for the range tested, and was found to be more associated with the geometry of the configuration. Local

normal force characteristics of the forebody (ogive-cylinder) were quite sensitive to Reynolds number but contributed little to the total force because of the small planform area of the forebody. Normal force characteristics of the frustum are dominated by linear, potential flow due to the large frustum angle which precluded significant crossflow separation (viscous effects). Local normal force characteristics of the aft cylinder do show significant non-linearities and Reynolds number effects near the end of the body but have a smaller effect on the total normal forces of this configuration due to the limited regions over which they act.

RECOMMENDATIONS

The present, rather cursory, analysis of force and pressure data obtained in the MSFC "Non-Linear-Lift" program has served to determine the applicability of certain crossflow drag correlation parameters and point out particular features of the interactions of Mach number, Reynolds number, and body shape on the total and local aerodynamic characteristics of these configurations.

Analysis of the force data indicates gratifying correlations of Mach number and Reynolds number effects for the limited conditions that were investigated. A complete analysis and correlation of the force data is therefore recommended, including the rerun data from the latest LTV tests and all side force and yawing moment data. Also, the rather extreme sensitivity of the aerodynamic characteristics at incompressible speeds should be confirmed by additional tests in a low turbulence facility with a large range in operating Reynolds numbers such as the Langley 3.5 x 7' low turbulence pressure tunnel. Existing models could be used and would yield baseline incompressible Reynolds number effects in a high quality airstream. Additional force tests to investigate compressibility effects in more detail are also very desirable.

The pressure data, while yielding basic information of Reynolds number and Mach number effects on the ogive-cylinder and ogive-cylinder-frustum-cylinder normal force and crossflow drag distributions, was not of sufficient quality or detail to define the important features of the flow at conditions near the onset of viscous effects at low and moderate angles of attack. Analysis of the high angle of attack pressure data was hampered by high density orifice effects and asymmetric flows. Additional pressure tests are therefore recommended to more accurately quantify the non-linear local aerodynamics of these configurations. Single row of orifice models of larger size than existing models should be used, and surface flow visualization data also obtained on the actual pressure model to insure that the pressure data is free of interactions with orifices or model irregularities. These tests should be limited to Reynolds number and Mach number conditions where specific flow regimes, indicated by the present analysis and future force data analysis, can be investigated in detail.

REFERENCES

1. Munk, M. "The Aerodynamic Forces on Airship Hulls", NACA Report 184, 1924.

2. Goldstein, S. "Modern Development in Fluid Dynamics", Dover Publications, Inc., New York, 1965.

3. Allen, H. J. and Perkins, E. W. "Characteristics of Flow over Inclined Bodies of Revolution." NACA RM A50L07, March 1951.

4. Kelly, H. R. "The Estimation of Normal Force and Pitching Moment Coefficient for Blunt Based Bodies of Revolution at Large Angles of Attack", U. S. Naval Ordnance Test Station, Tech. Memo. 998, July 1953.

5. Hill, J. A. F. "A Nonlinear Theory of the Lift on Slender Bodies of Revolution". Proceedings U. S. Navy Symposium on Aeroballistics, NAVORD Rpt. 5338, October 1954.

6. Schindel, L. H. "Vortex Separation on Slender Bodies of Elliptic Cross Section". Massachusetts Institute of Technology, Aerophysics Laboratory, Tech. Rpt. 138, August, 1967.

7. Sarpkaya, T. "Separated Flow about Lifting Bodies and Impulsive Flow about Cylinders", AIAA Jour., Vol. 4, No. 3, March 1966.

8. Box, D. M. "Static Stability Tests on a Number of Bodies of Revolution in the Mach Number Range of .4 to 5.0", LTV Aerospace Corp., Vought Aeronautics Div., Report No. HSWT Test 225, Nov., 1966.

9. Chianese, F. "Results of an Experimental Investigation to Obtain Surface Pressure Distributions on Four Models - Two Variable Cross Sections of Two Different Scales" Chrysler Corp. Space Div., Tech. Note TN-AP-68-368, November 1968.

10. Pick, G. S. "Investigation of Side Forces on Ogive-Cylinder Bodies at High Angles of Attack in the M = 0.5 to 1.1 Range". AIAA Paper No. 71-570, June 1971.

11. Gowen, F. E. and Perkins, E. W. "Drag of Circular Cylinders for a Wide Range of Reynolds Numbers and Mach Numbers", NACA TN 2960, June, 1953.

12. Jones, G. W. and Cincotta, J. J. "Aerodynamic Forces on a Stationary and Oscillating Circular Cylinder at High Reynolds Numbers", NASA TR R-300, Feb., 1969.

13. Perkins, E. W. and Jorgensen, L. H. "Comparison of Experimental and Theoretical Normal-Force Distributions on an Ogive-Cylinder at Mach Number 1.98" NACA TN 3716, May, 1956.

14. Mello, J. F. "Investigation of Normal Force Distributions and Wake Vortex Characteristics of Bodies of Revolution at Supersonic Speeds" Jour. Aero/Space Sci., Vol. 26, No. 3, March, 1959.

15. Jorgensen, L. H. and Perkins, E. W. "Investigation of Some Wake Vortex Characteristics of an Inclined Ogive-Cylinder Body at Mach Number 2.0" NACA Report 1371, 1958.

16. Tinling, B. E. and Allen, C. Q. "An Investigation of the Normal-Force and Vortex-Wake Characteristics of an Ogive-Cylinder Body at Subsonic Speeds", NASA TN D-1297, April, 1962.

17. Struck, H. G. "Analytical Determination of Pressure Distributions on Blunt-Based Bodies of Revolution Under Influence of the Wake, at Small Angles of Attack in Subsonic Flow by the Use of Surface Singularities." Marshall Space Flight Center Internal Note R-AERO-IN-18-64. July 10, 1964.

18. Mendelson, R. S. and Newman, S. R. "IBM 7094 Program, Van Dyke's Modified Hybrid Theory." Chrysler Corp., Space Division Tech. Note TN-AE-64-30. Oct., 1965.

19. Taylor, J. W. "IBM 7094 Program for the Second-Order Shock-Expansion Theory." Chrysler Corp., Space Div. Tech. Note TN-AE-65-112. Feb., 1966.

20. Meyer, P.K. "The Aerodynamic Analysis of Bodies of Revolution at Supersonic and Hypersonic Velocities Using Modified Newtonian Flow." Chrysler Corp., Missile Div. Tech. Note AME TN-17-60.

21. **Box, D. M. "Transonic Data Validation Runs on a Number of Bodies of Revolution in the Mach Range of 0.4 to 1.2." Vought Aeronautics Corp., HSWT Test C-71-6. November 1971**

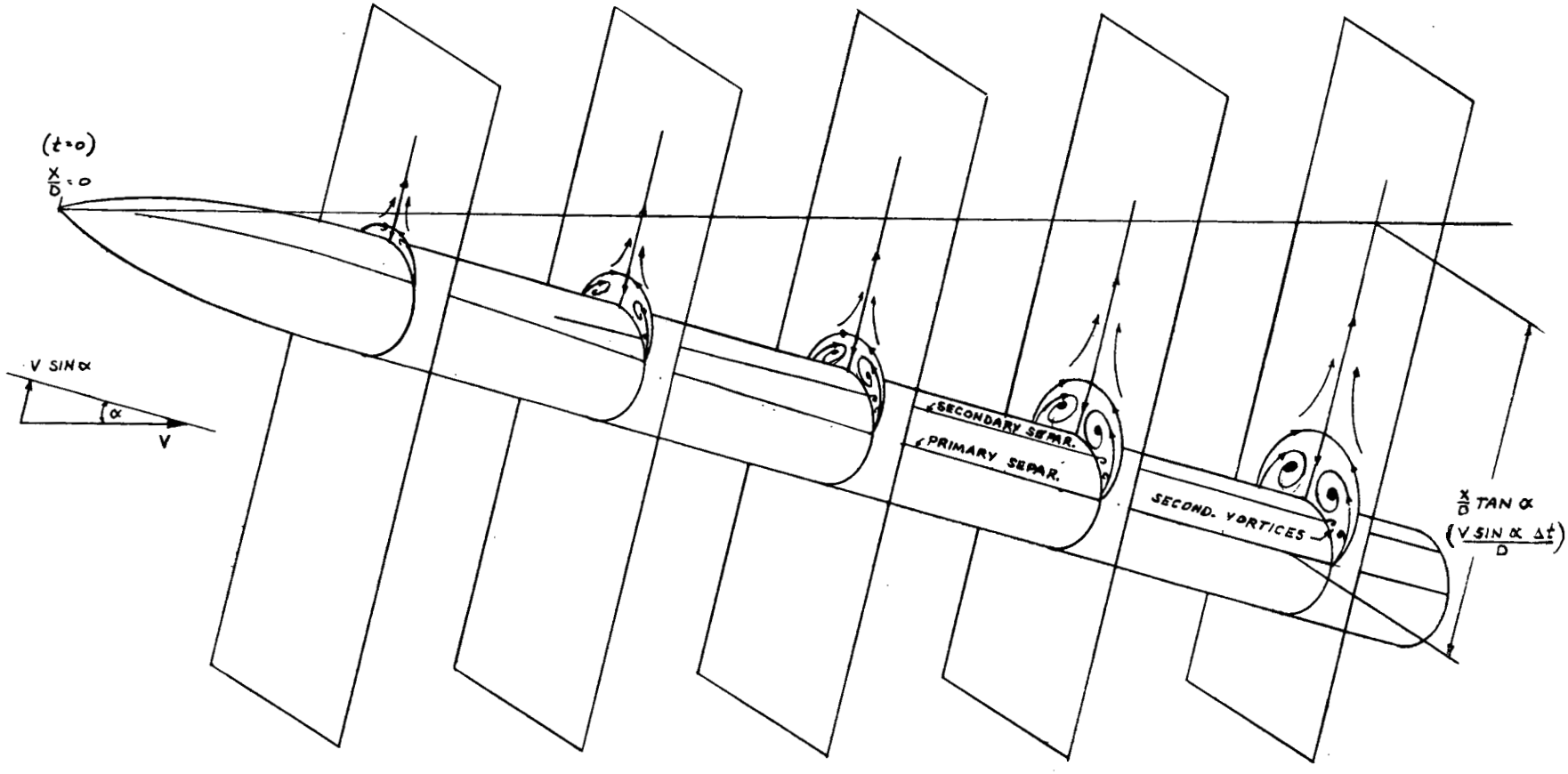

Figure 1. Crossflow About a Body of Revolution at Angle of Attack

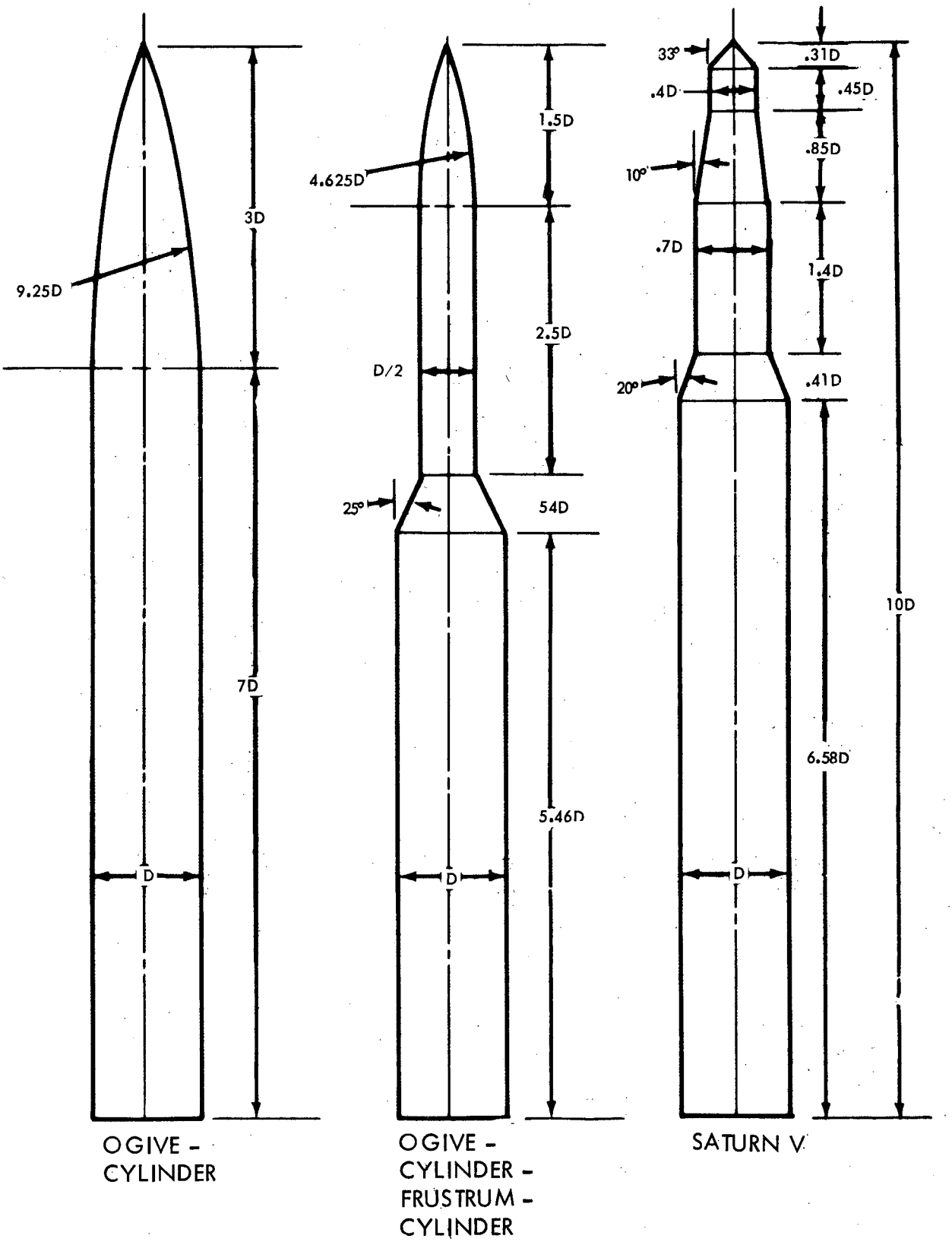

Figure 2. MSFC "Non-Linear-Lift" Study Configurations

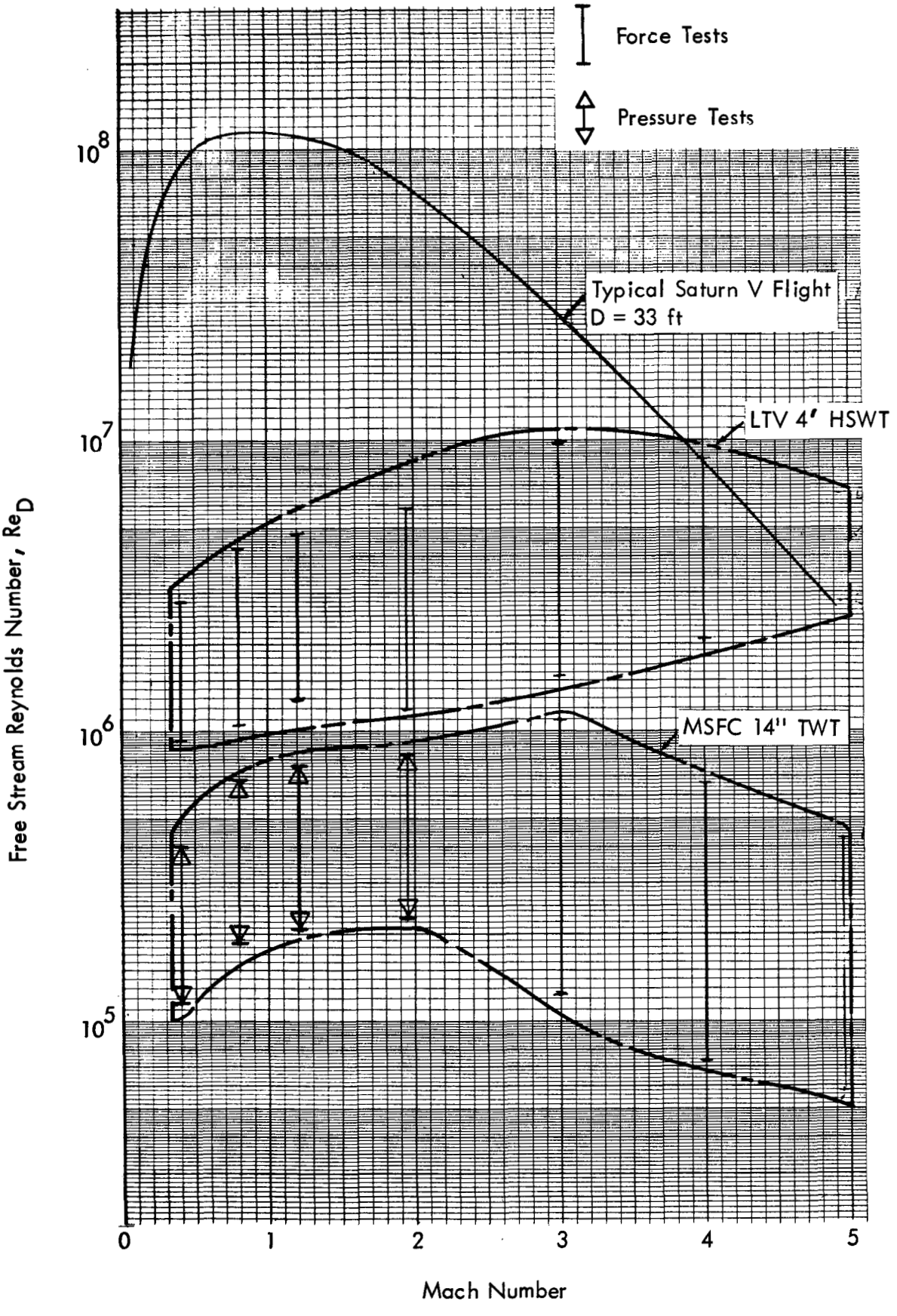

Figure 3. Mach/Reynolds No. Test Conditions - MSFC "Non-Linear-Lift" Research Program

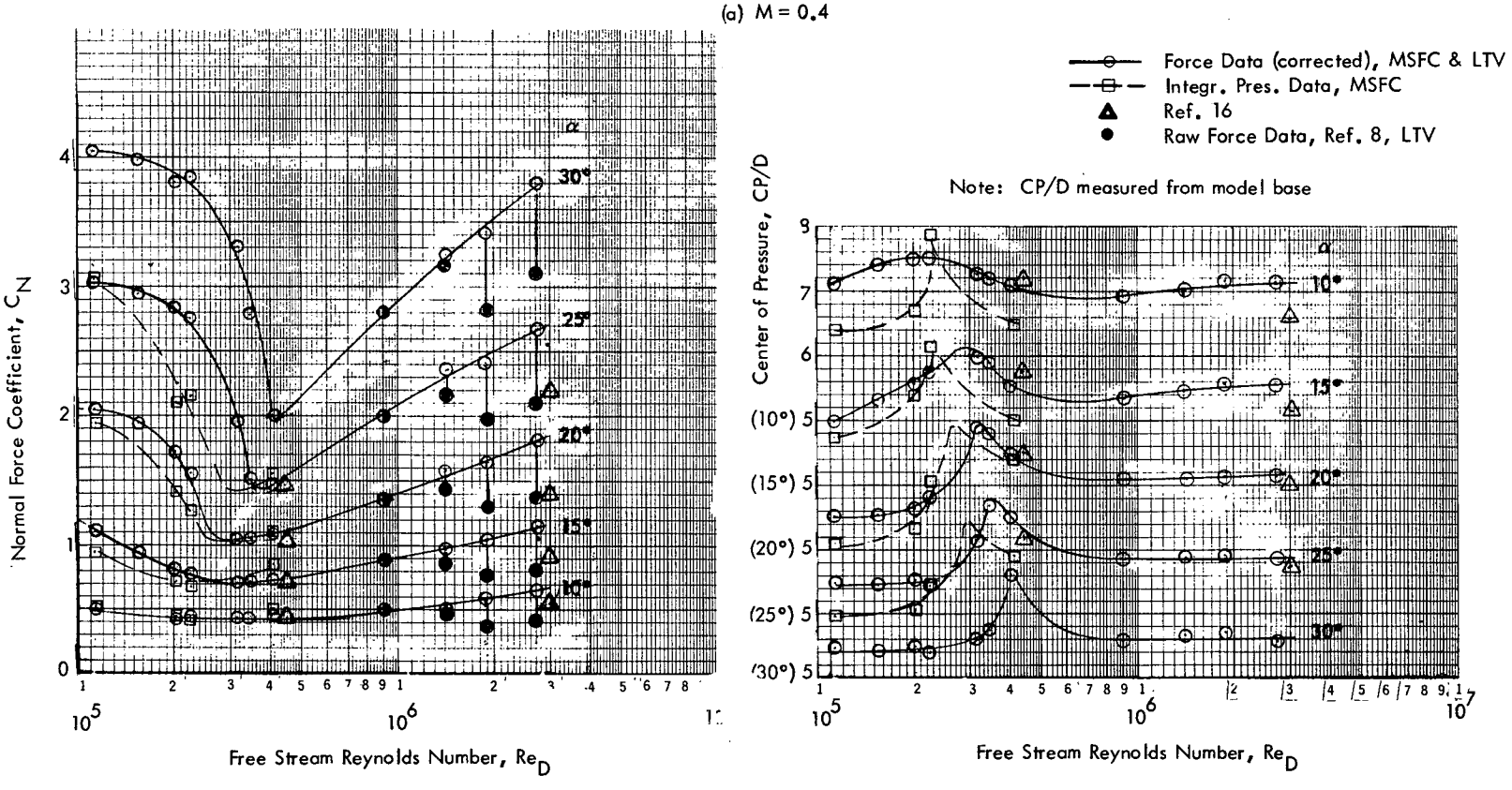

Figure 4. Ogive-Cylinder Normal Force and Center of Pressure

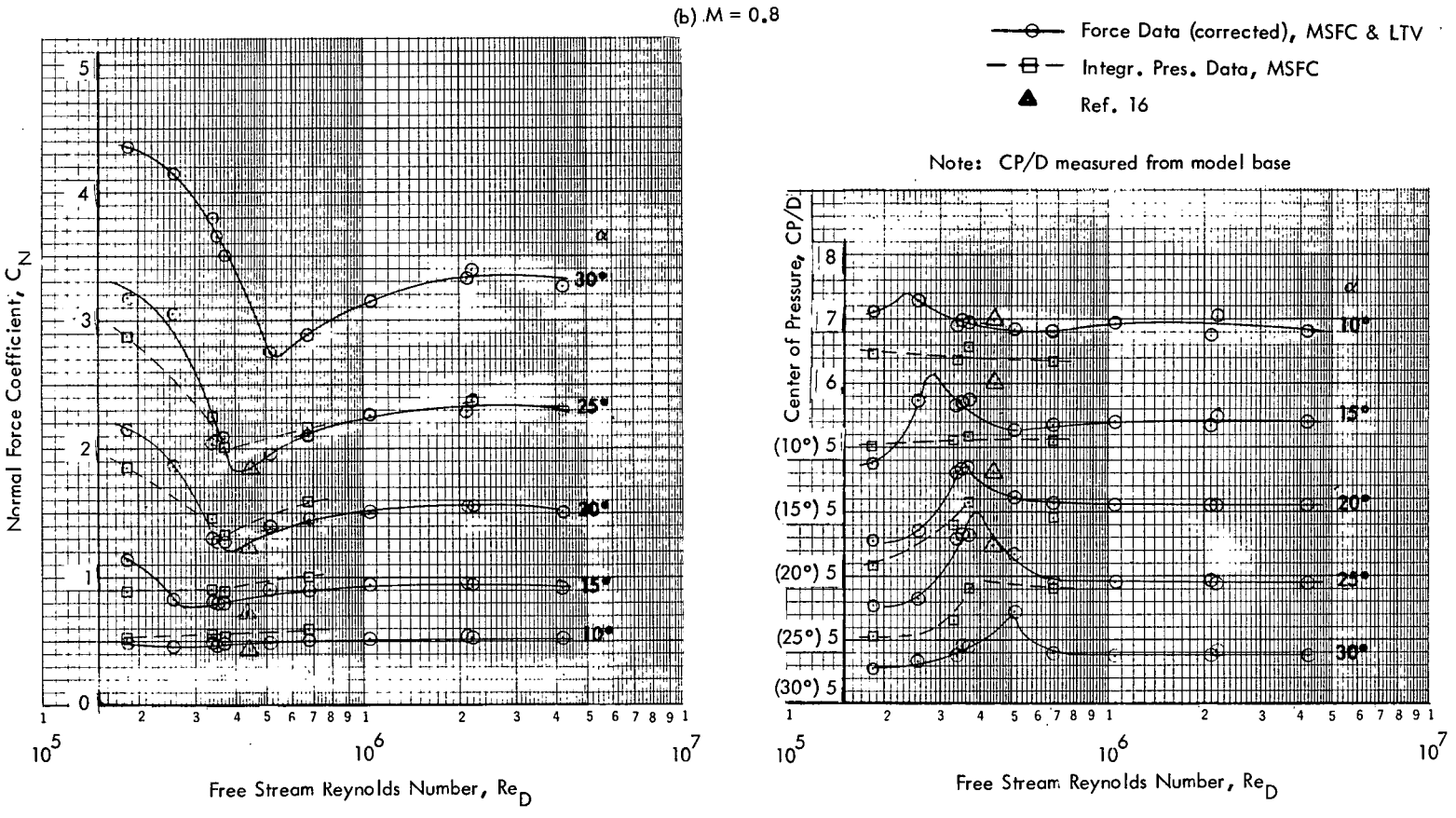

Figure 4. Ogive-Cylinder Normal Force and Center of Pressure (continued)

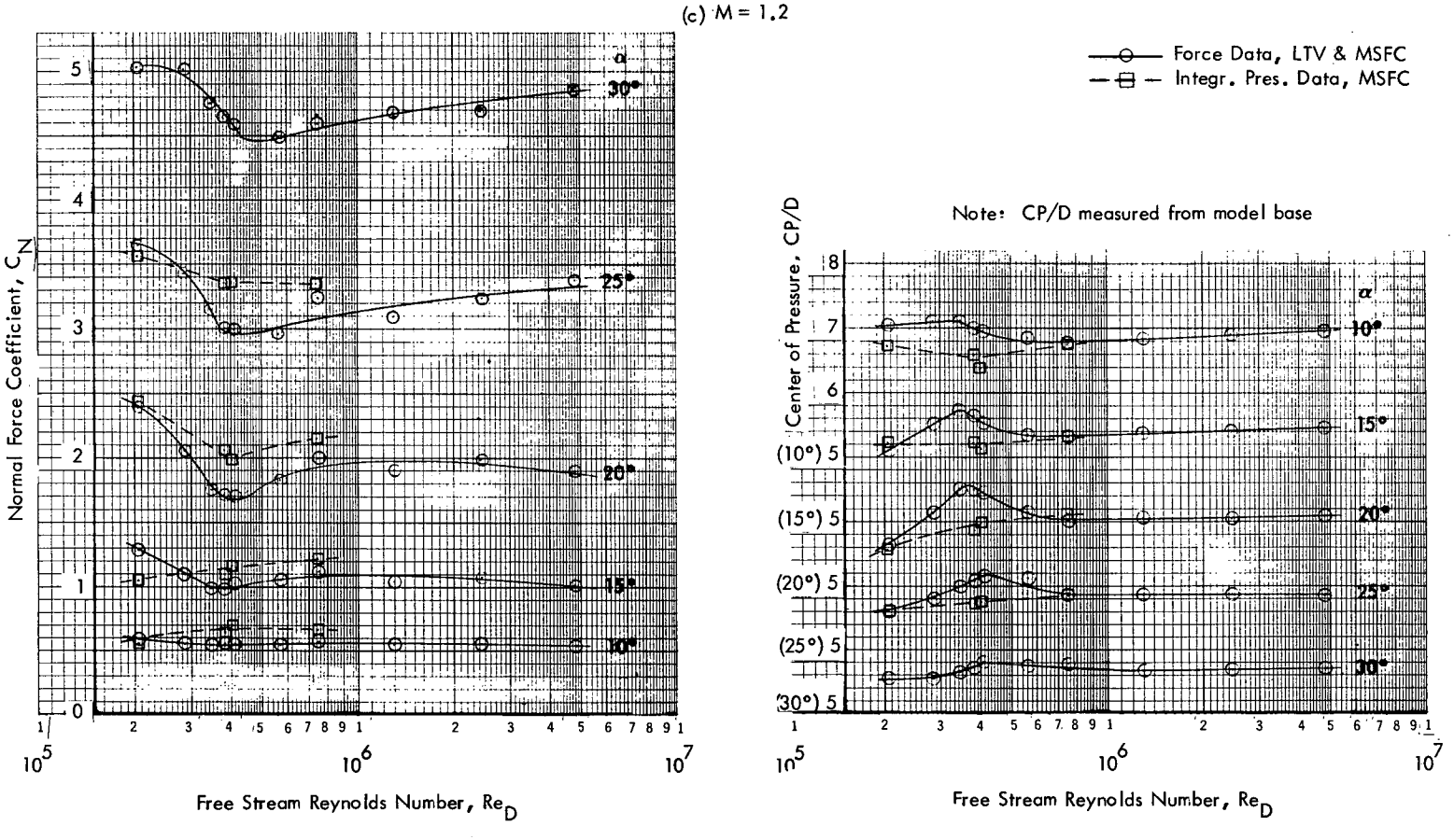

Figure 4. Ogive-Cylinder Normal Force and Center of Pressure (continued)

(d) M = 2.0

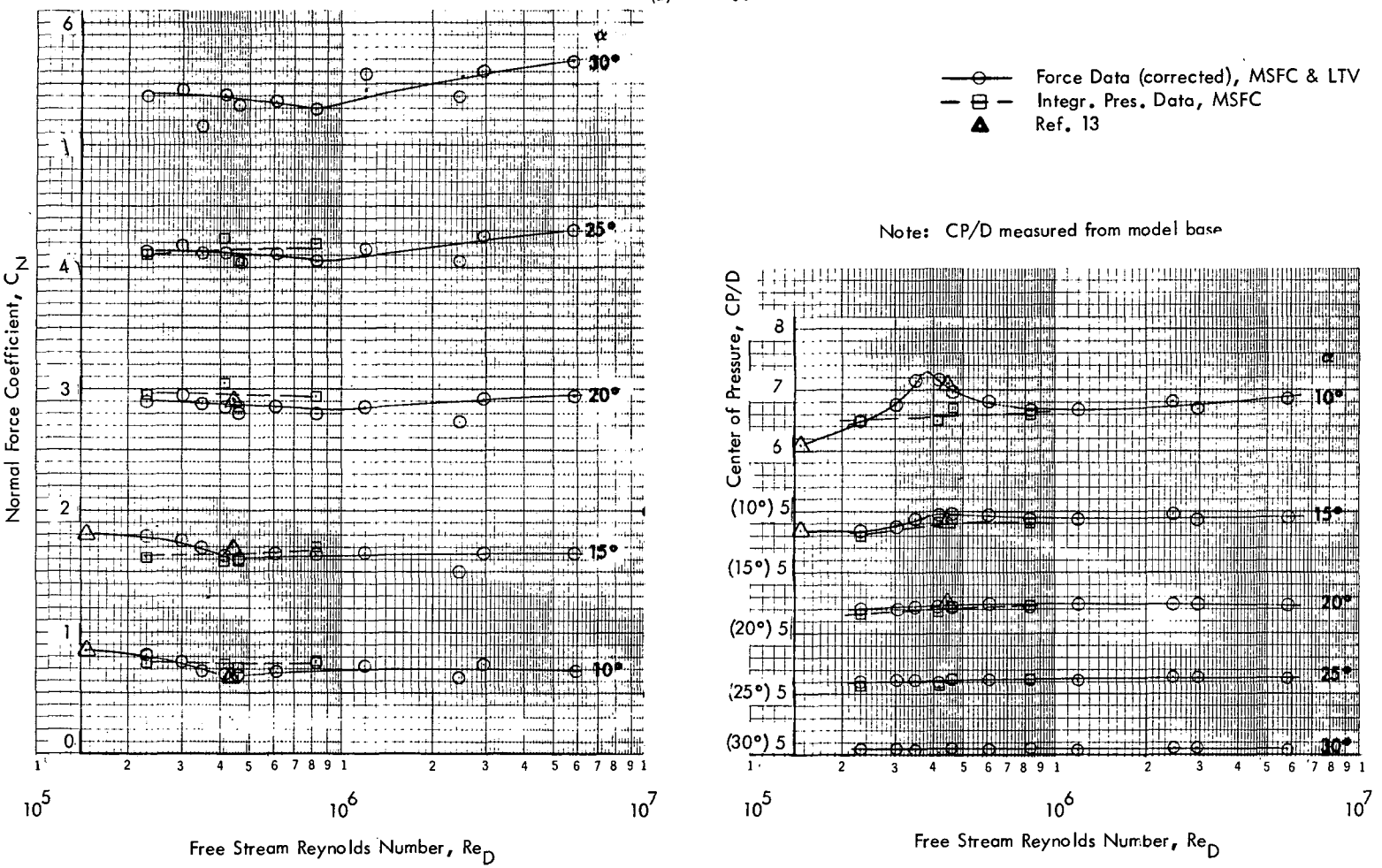

Figure 4. Ogive-Cylinder Normal Force and Center of Pressure (concluded)

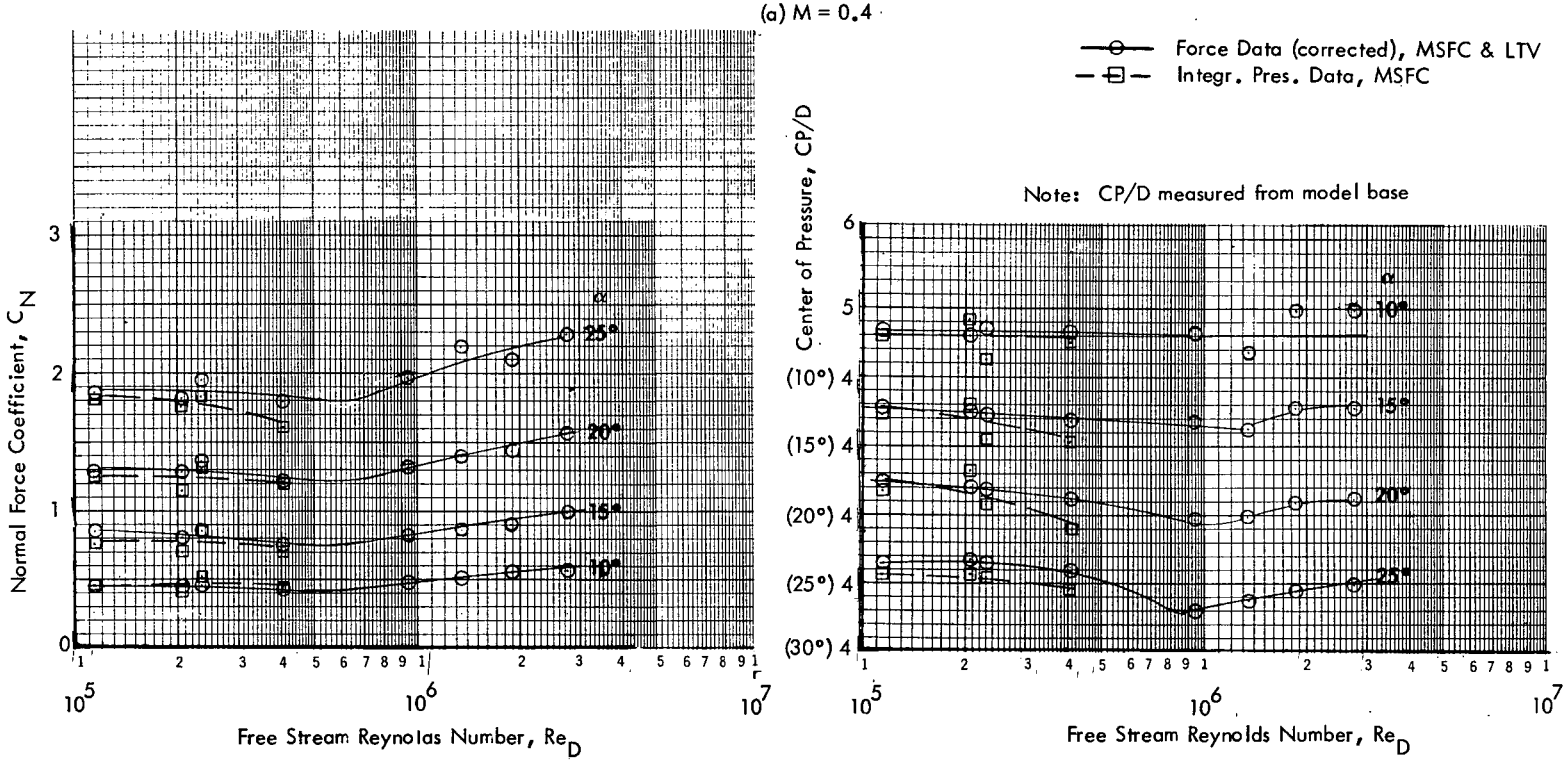

Figure 5. Ogive-Cylinder-Frustum-Cylinder Normal Force and Center of Pressure

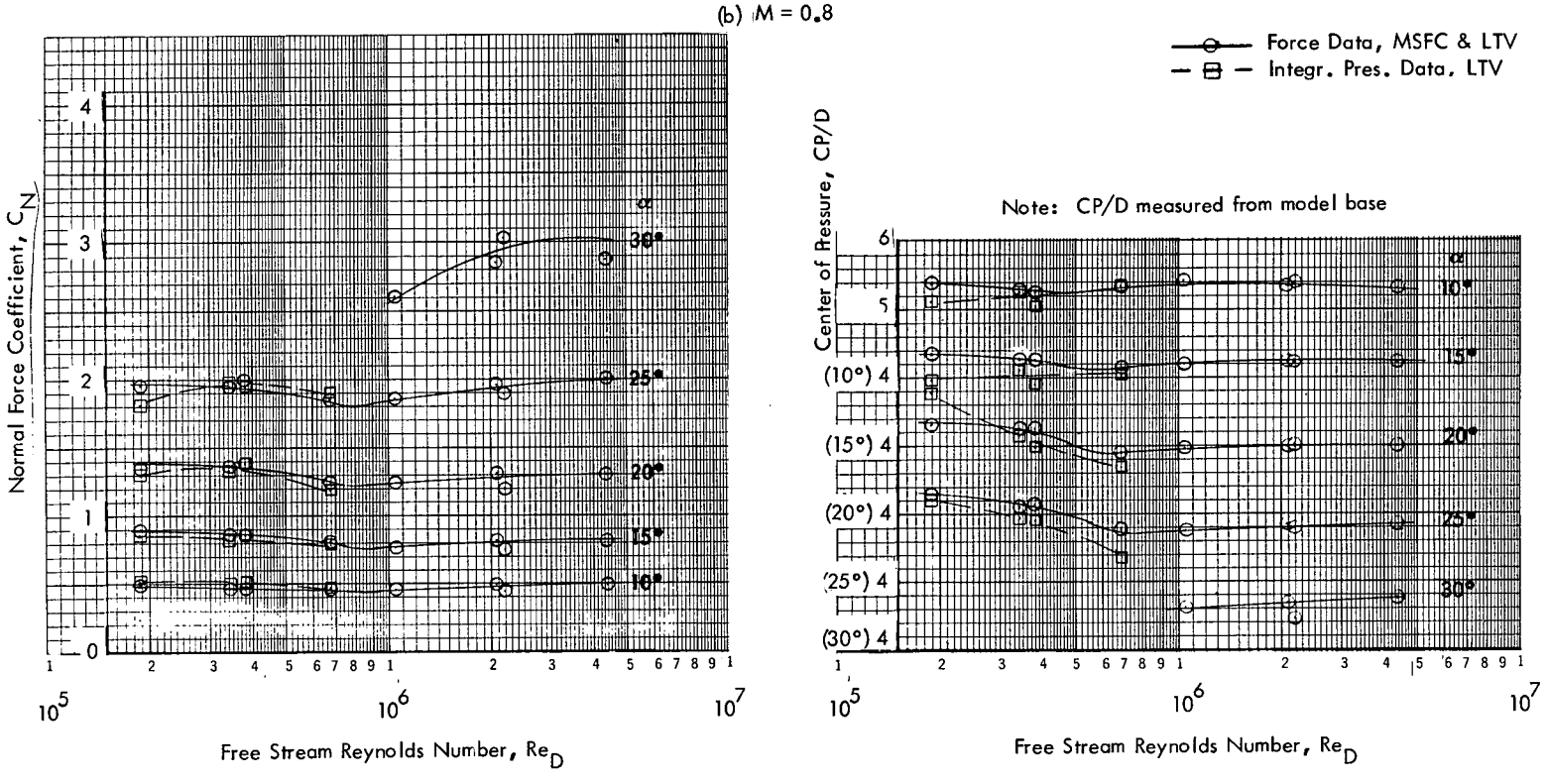

Figure 5. Ogive-Cylinder - Frustum-Cylinder Normal Force and Center of Pressure (continued)

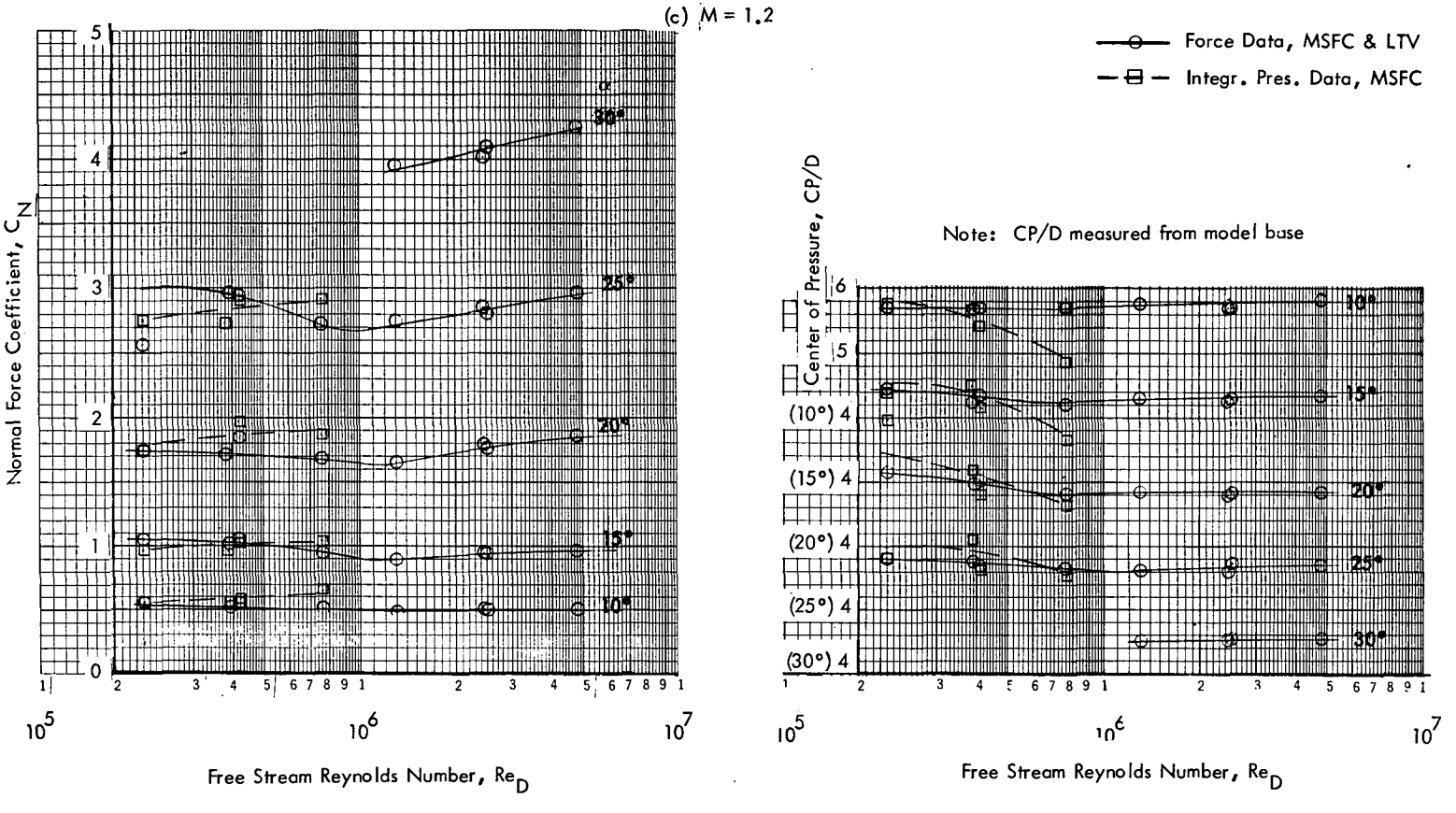

Figure 5. Ogive-Cylinder - Frustum-Cylinder Normal Force and Center of Pressure (continued)

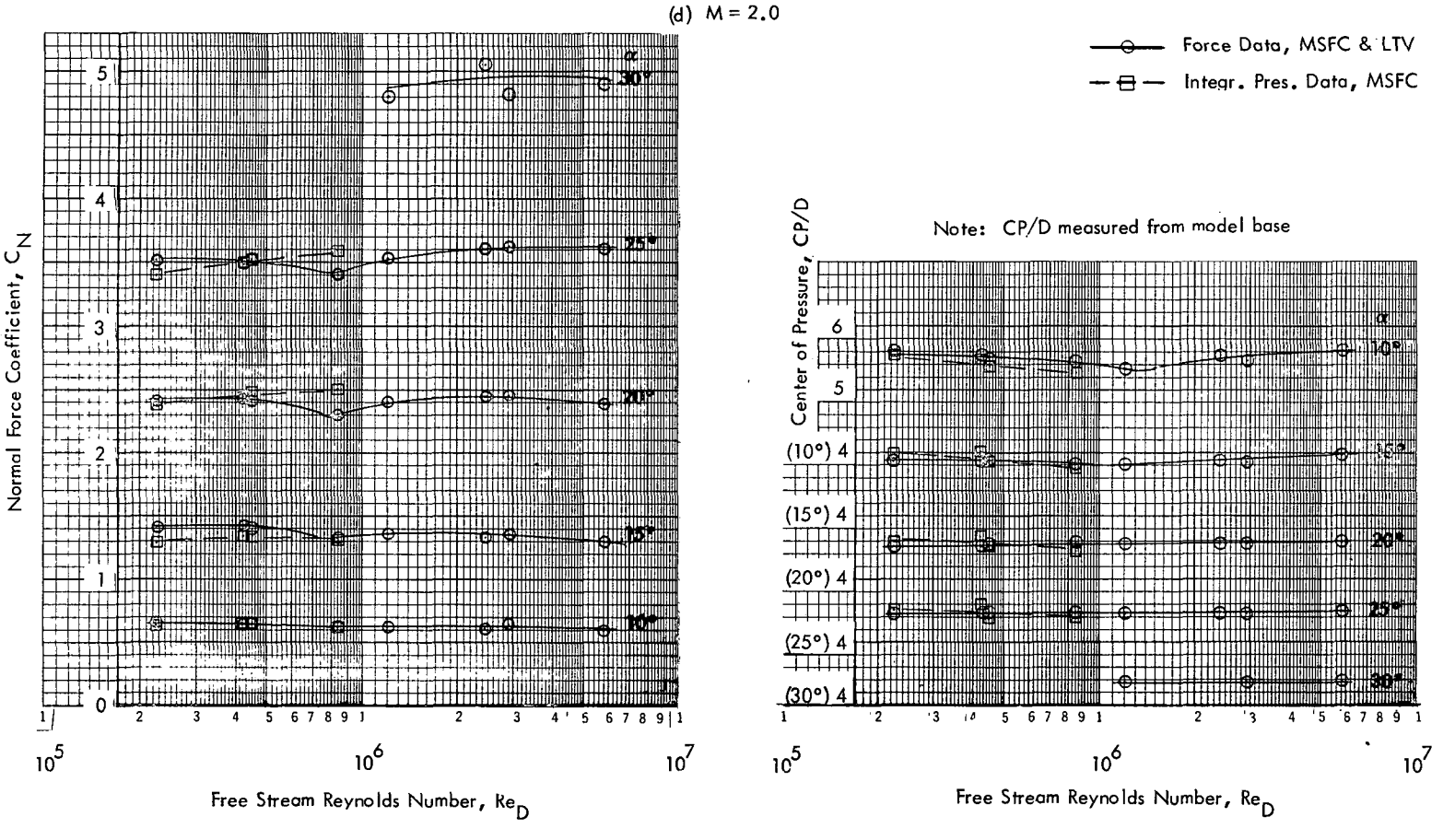

Figure 5. Ogive-Cylinder - Frustum-Cylinder Normal Force and Center of Pressure (concluded)

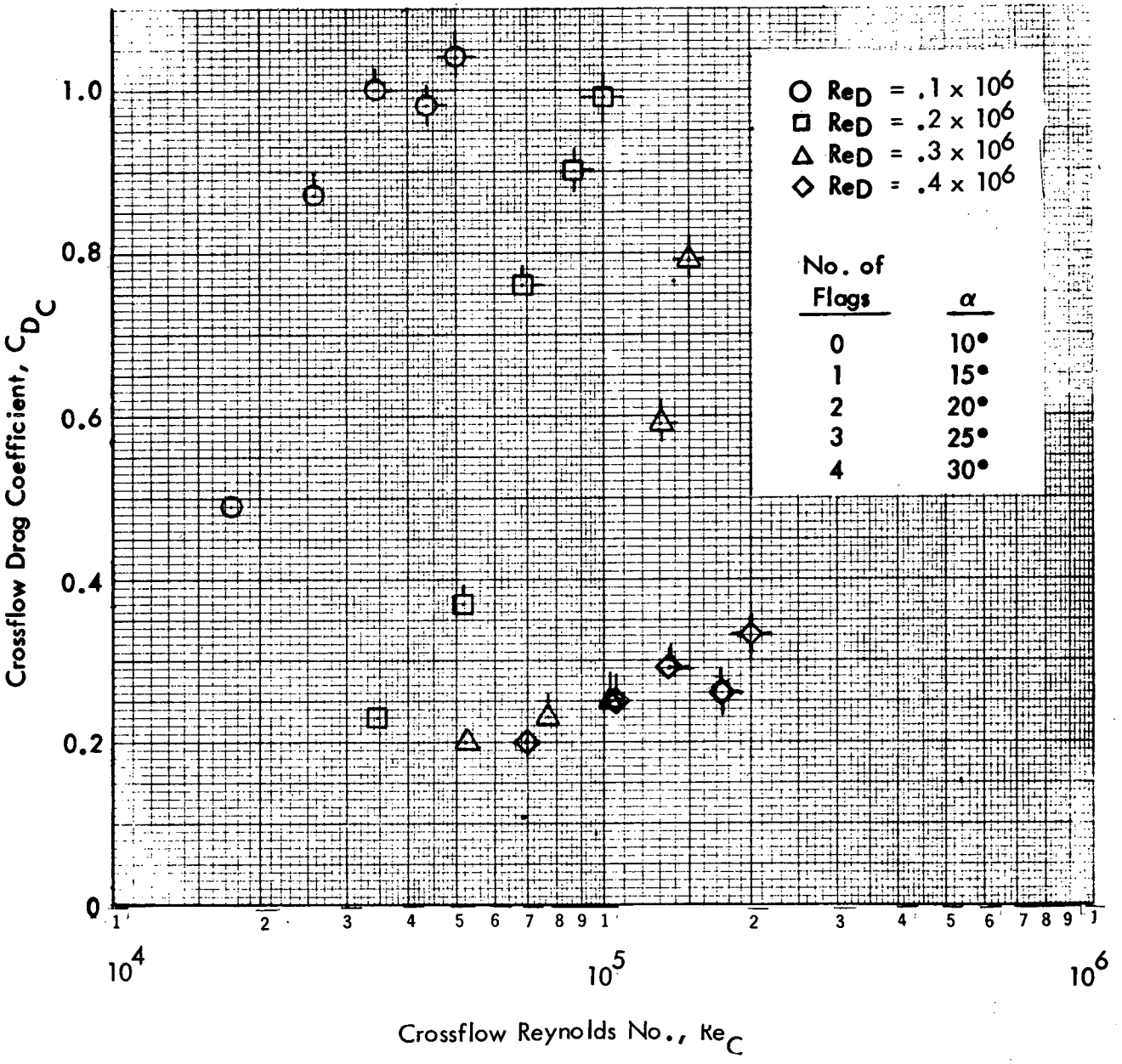

Figure 6. Correlation of Ogive/Cylinder Crossflow Drag Coefficient as a Function of Crossflow Reynolds Number, M = 0.4

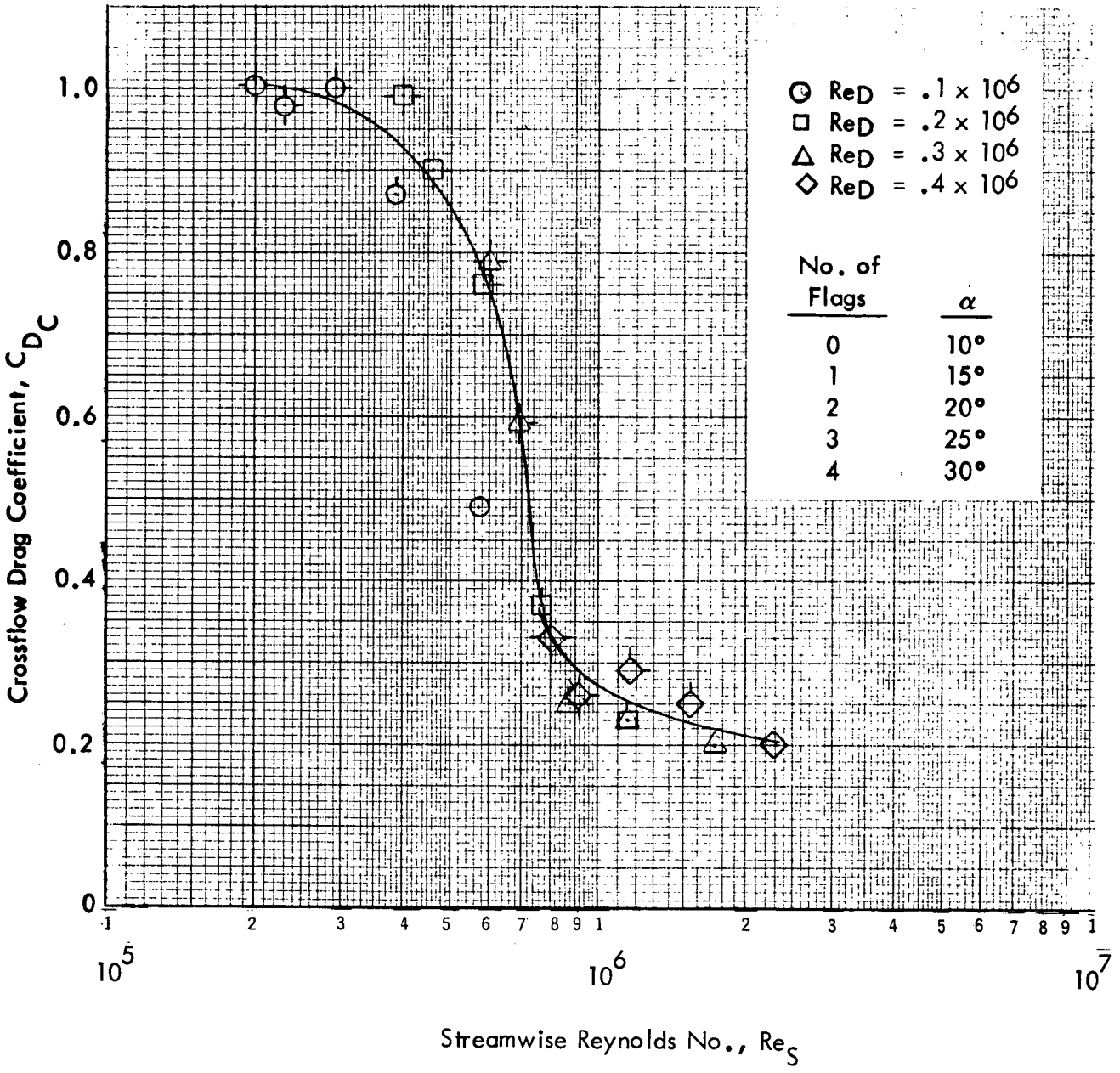

Figure 7. Correlation of Ogive/Cylinder Crossflow Drag Coefficient as a Function of Streamwise Reynolds Number, M = 0.4

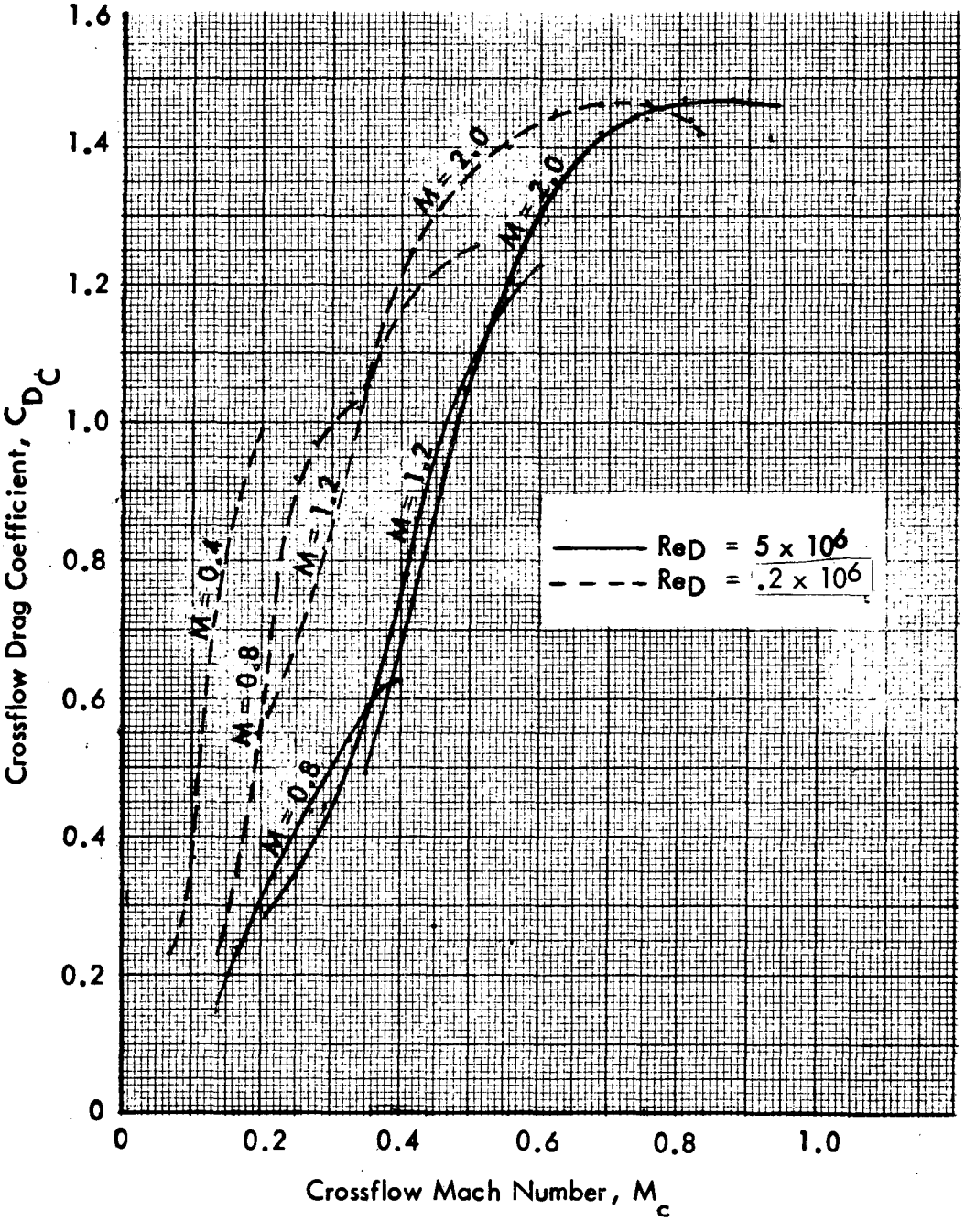

Figure 8. Effect of Compressibility on Ogive-Cylinder Crossflow Drag Characteristics

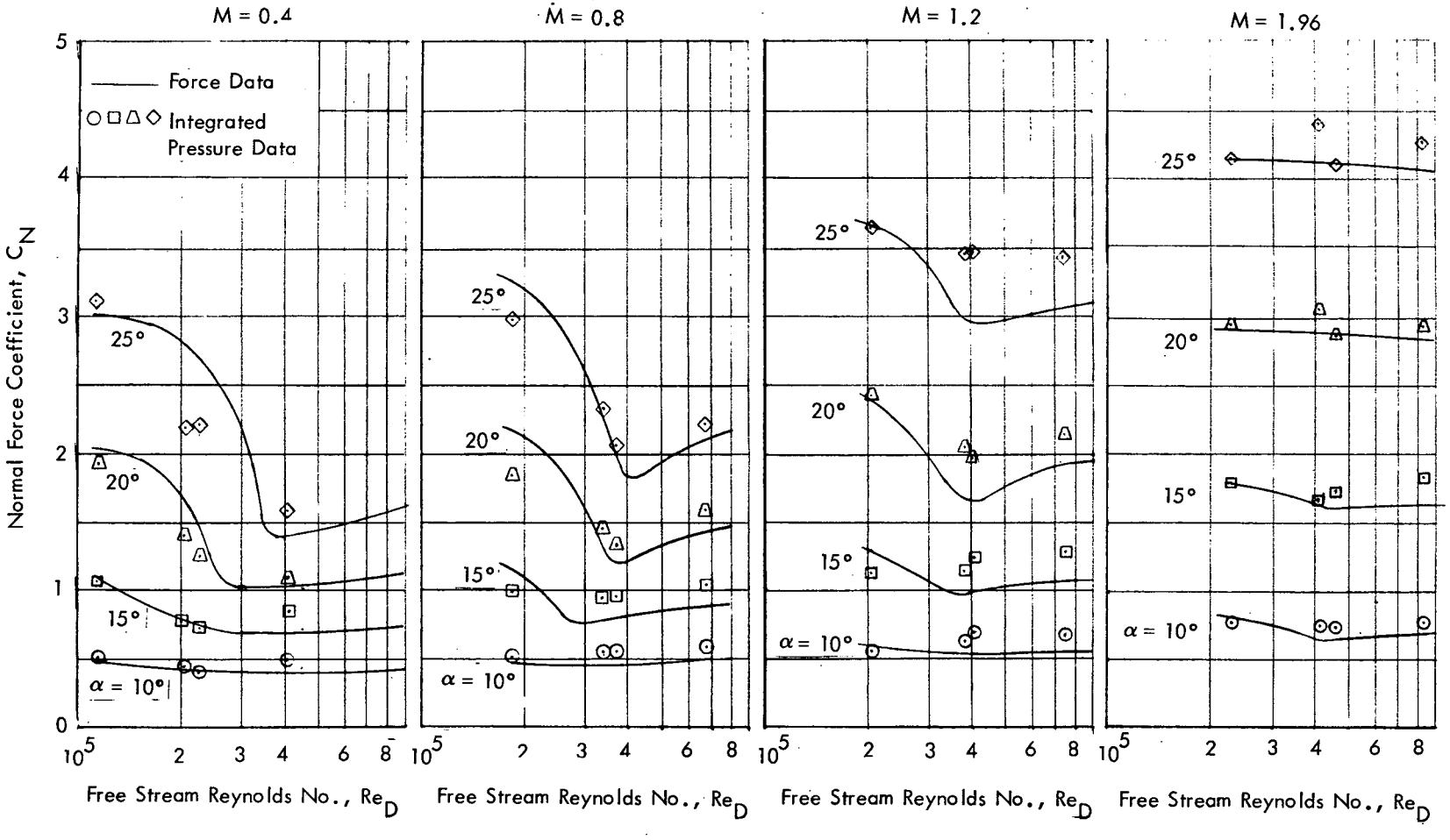

Figure 9. Comparison of Ogive-Cylinder Normal Force Characteristics, Force/Integrated Pressure Data

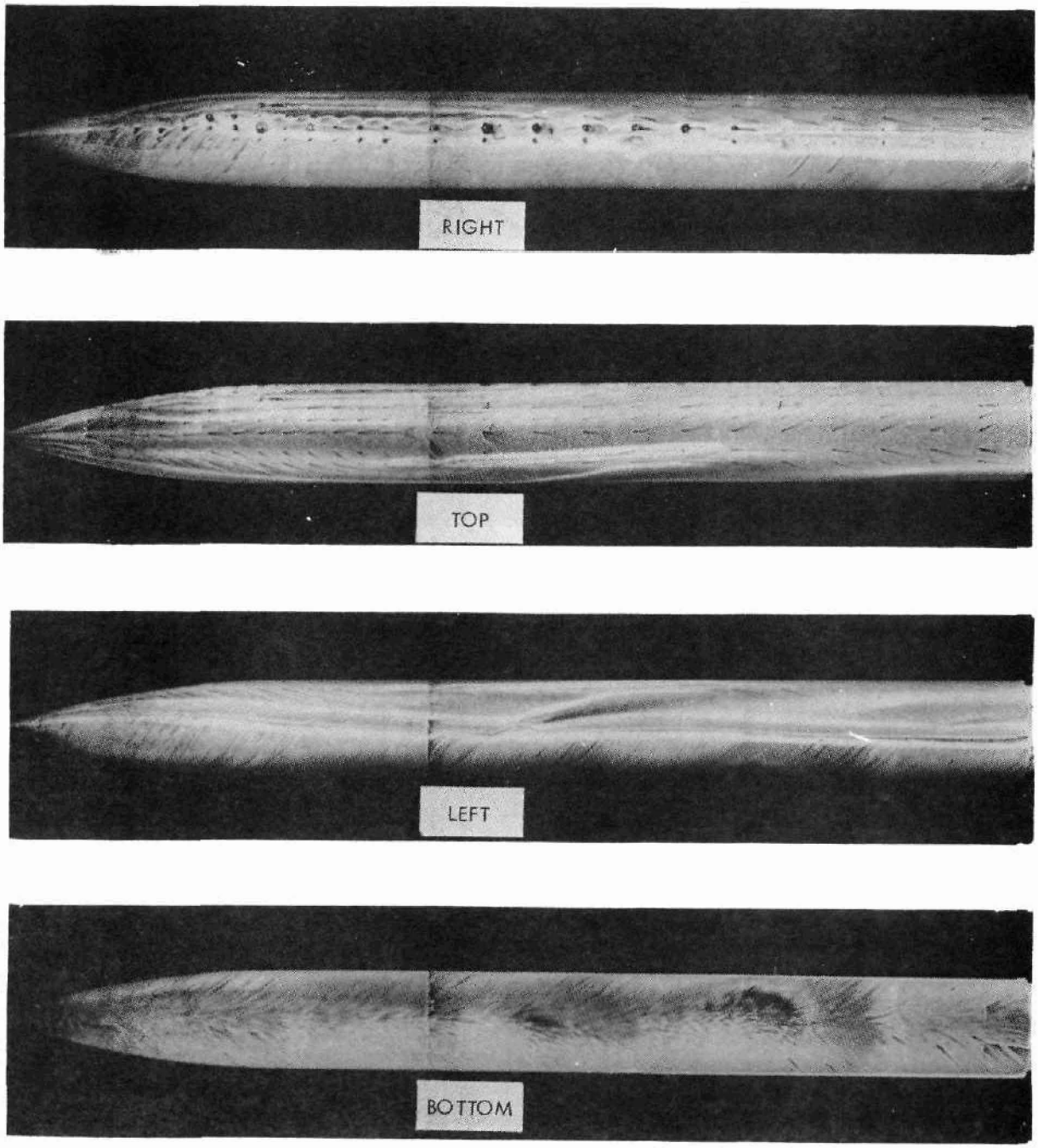

$M = 0.4,\ \alpha = 24.5°,\ \phi_m = 0,\ Re_D = .23 \times 10^6$

Figure 10. Effect of Orifices on Surface Flow Patterns

$M = 0.4 \quad \alpha = 24.5°$

$Re_D = .23 \times 10^6$

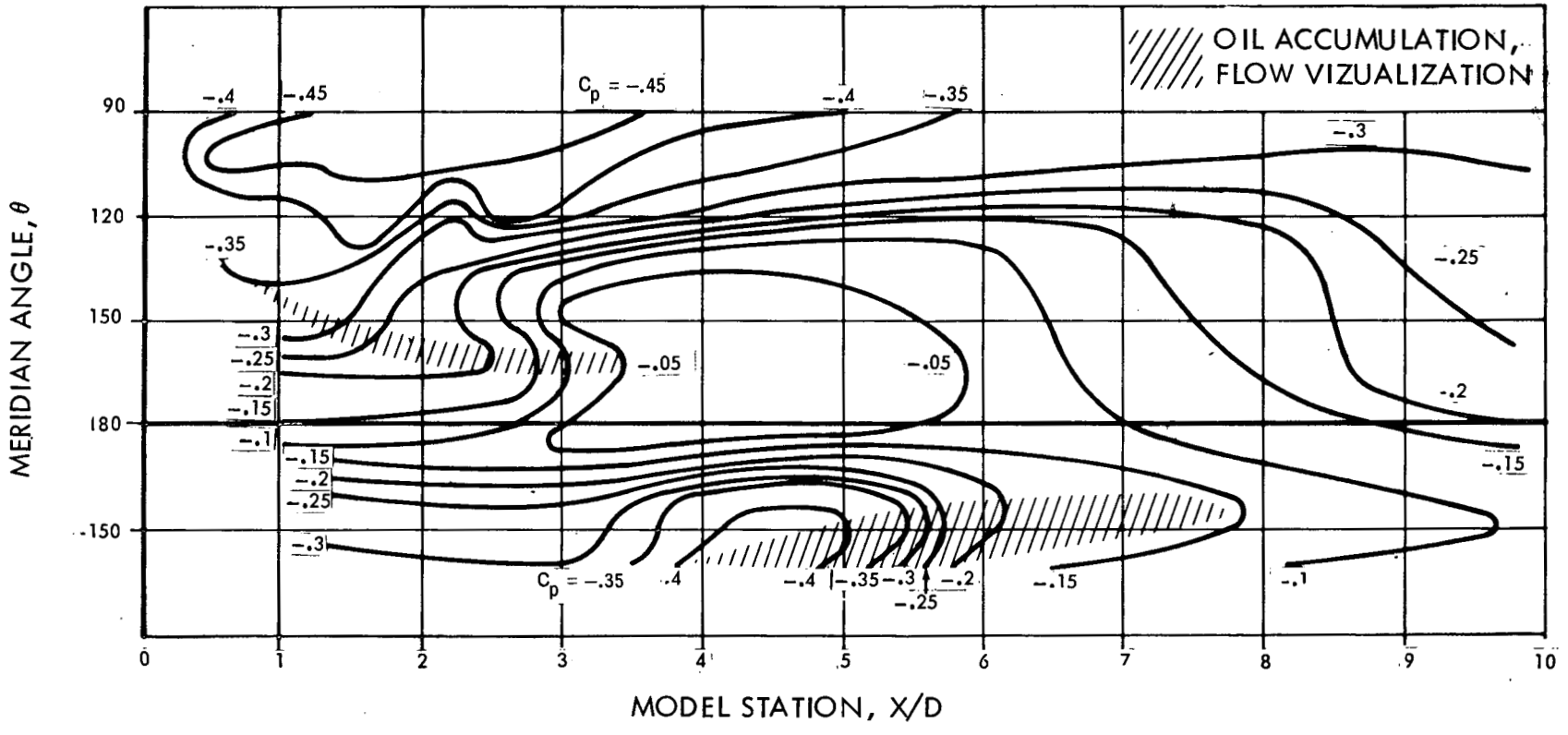

Figure 11. Surface Pressures on Lee Side of Ogive-Cylinder

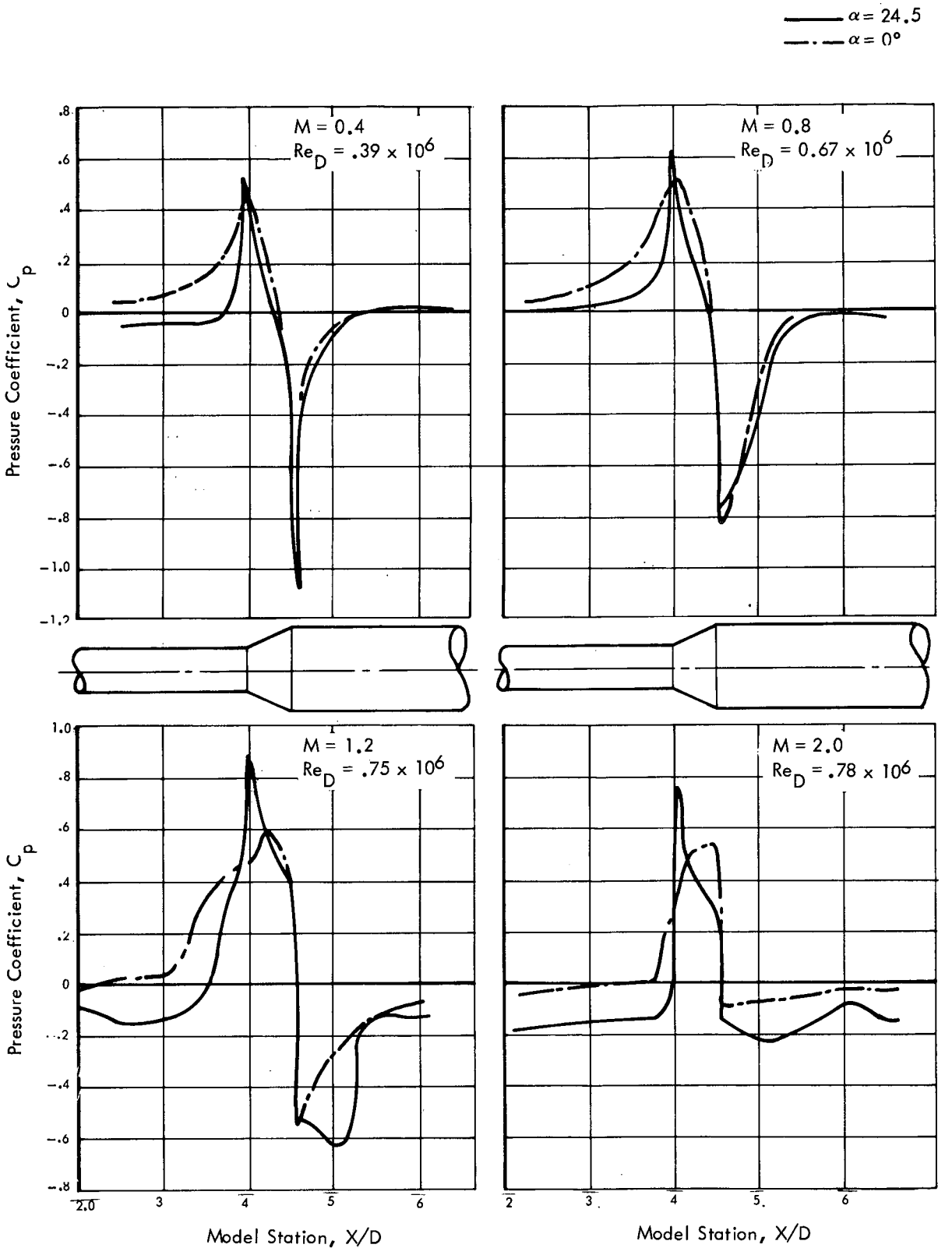

Figure 12. Pressure Distribution Along Leeward Meridian, O/C/F/C

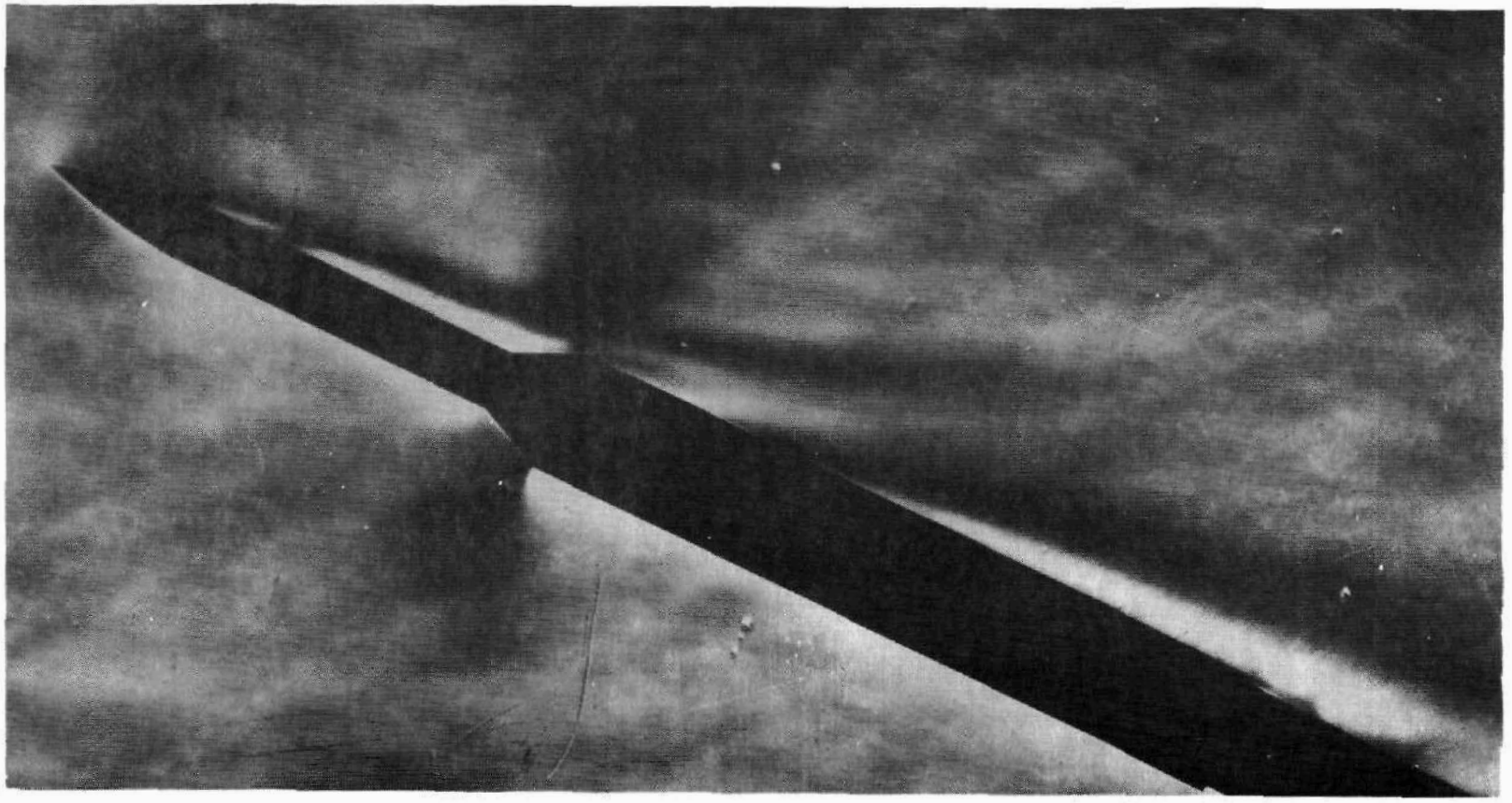

Figure 13. Schlieren Photograph of Flow Around Ogive-Cylinder-Frustum Cylinder, $M = 0.8$, $Re_D = .67 \times 10^6$, $\alpha = 24.5°$

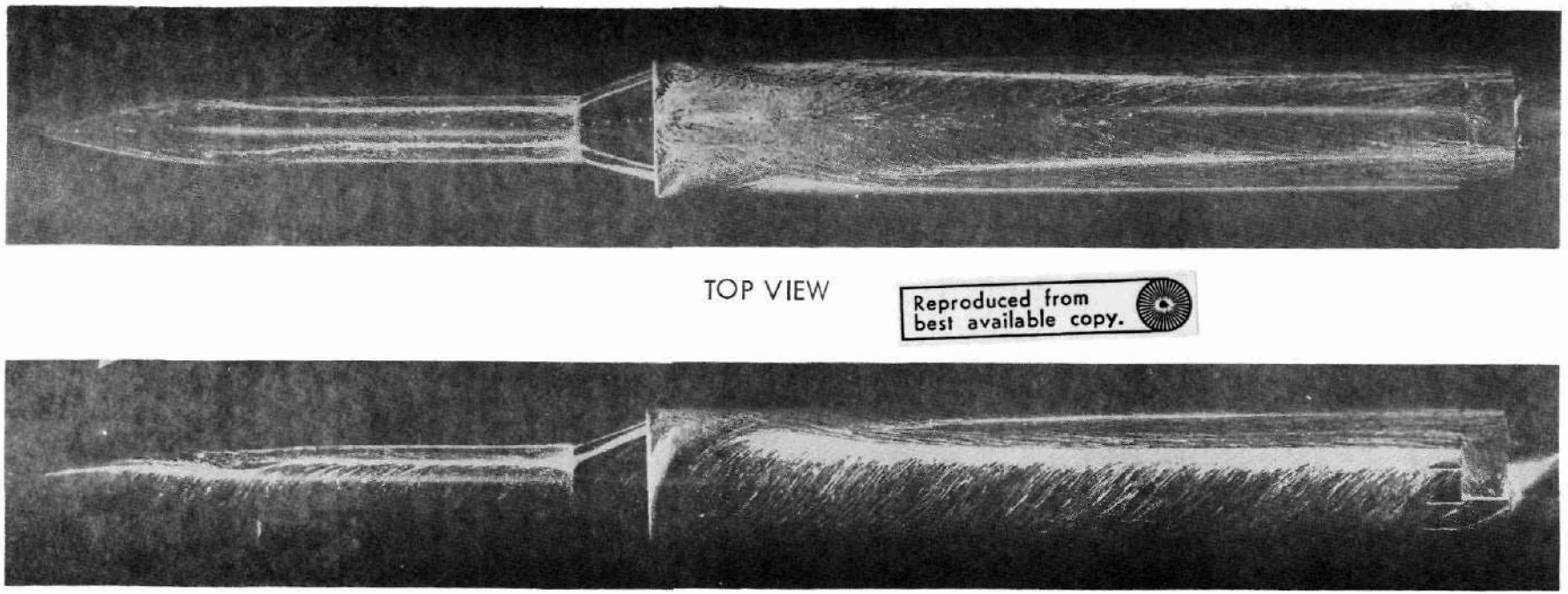

TOP VIEW

α = 24.5° SIDE VIEW

Figure 14. Surface Flow Visualization, Ogive-Cylinder-Frustum-Cylinder, $M = 0.8$, $Re_D = .67 \times 10^6$

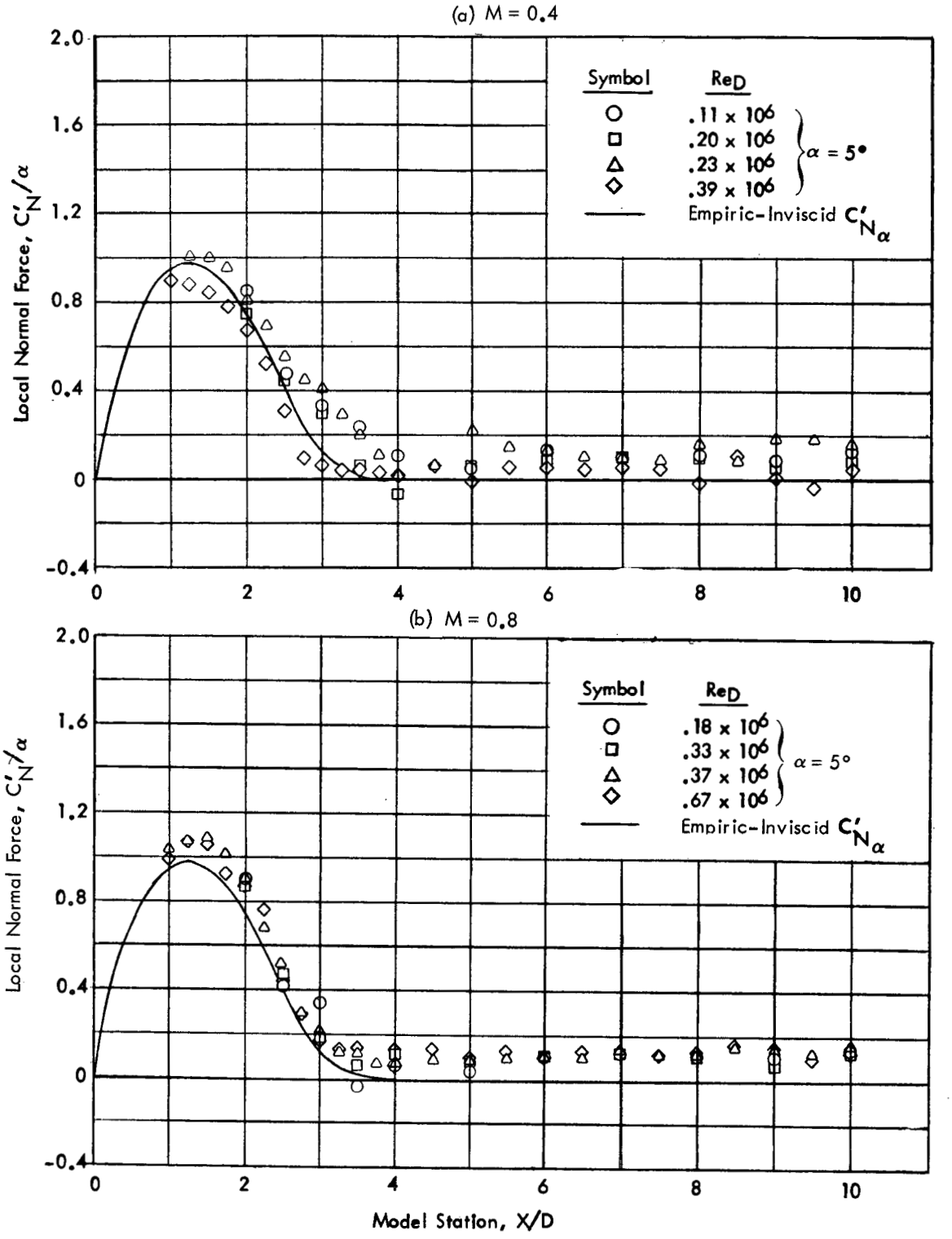

Figure 15. Local Normal Force Distribution, Ogive-Cylinder

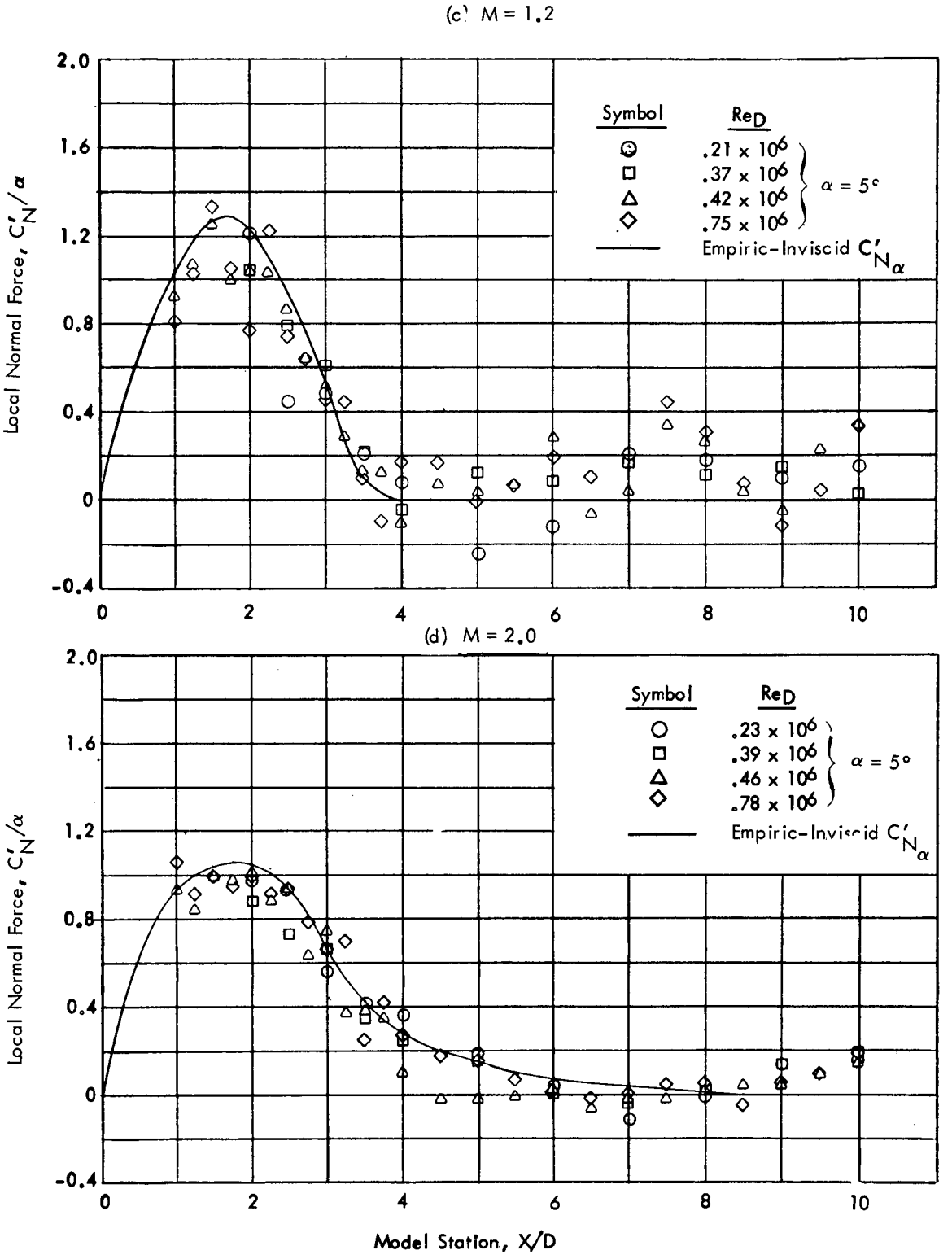

Figure 15. Local Normal Force Distribution, Ogive-Cylinder (concluded)

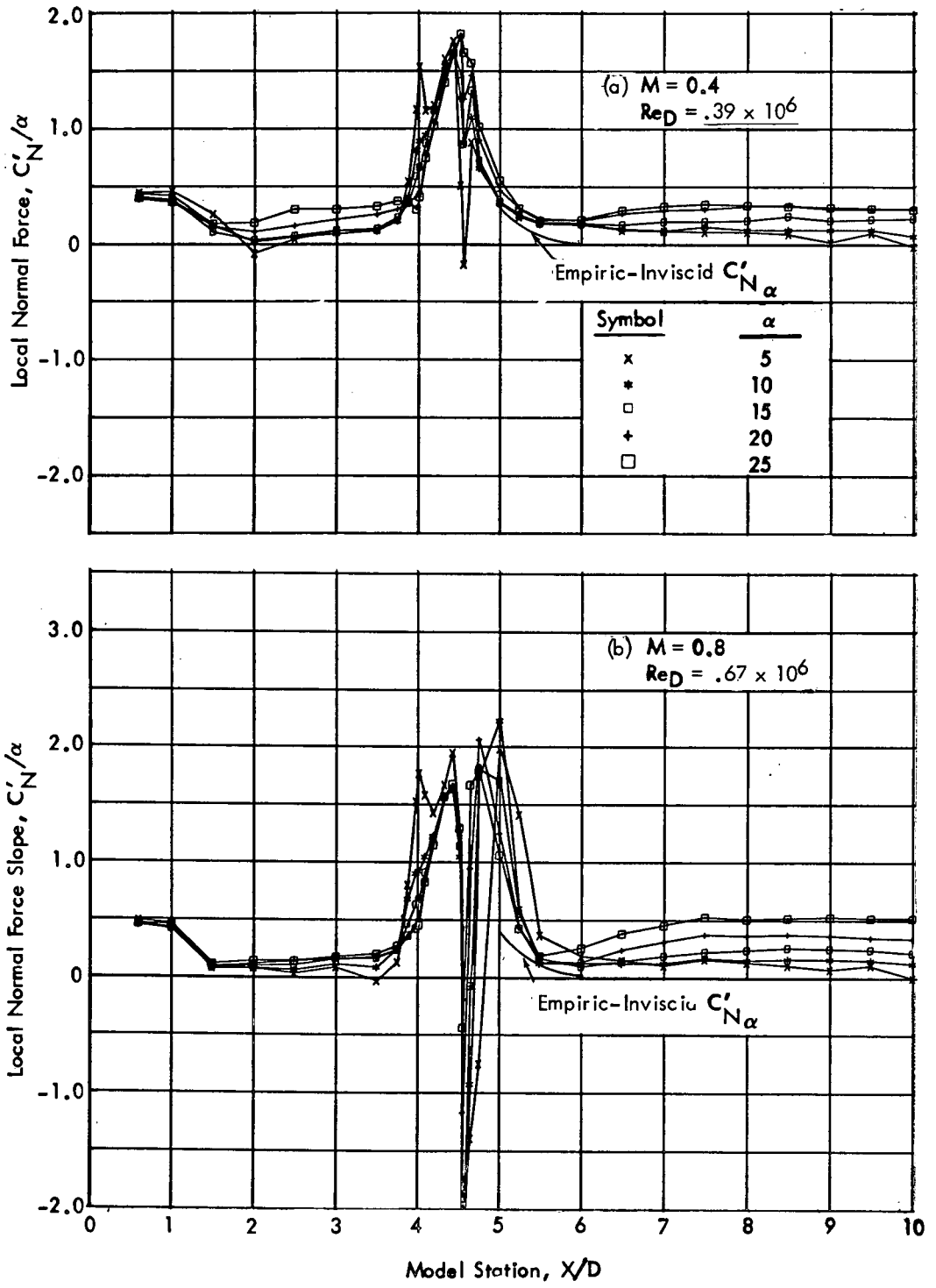

Figure 16. Local Normal Force Distributions, Ogive-Cylinder-Frustum-Cylinder

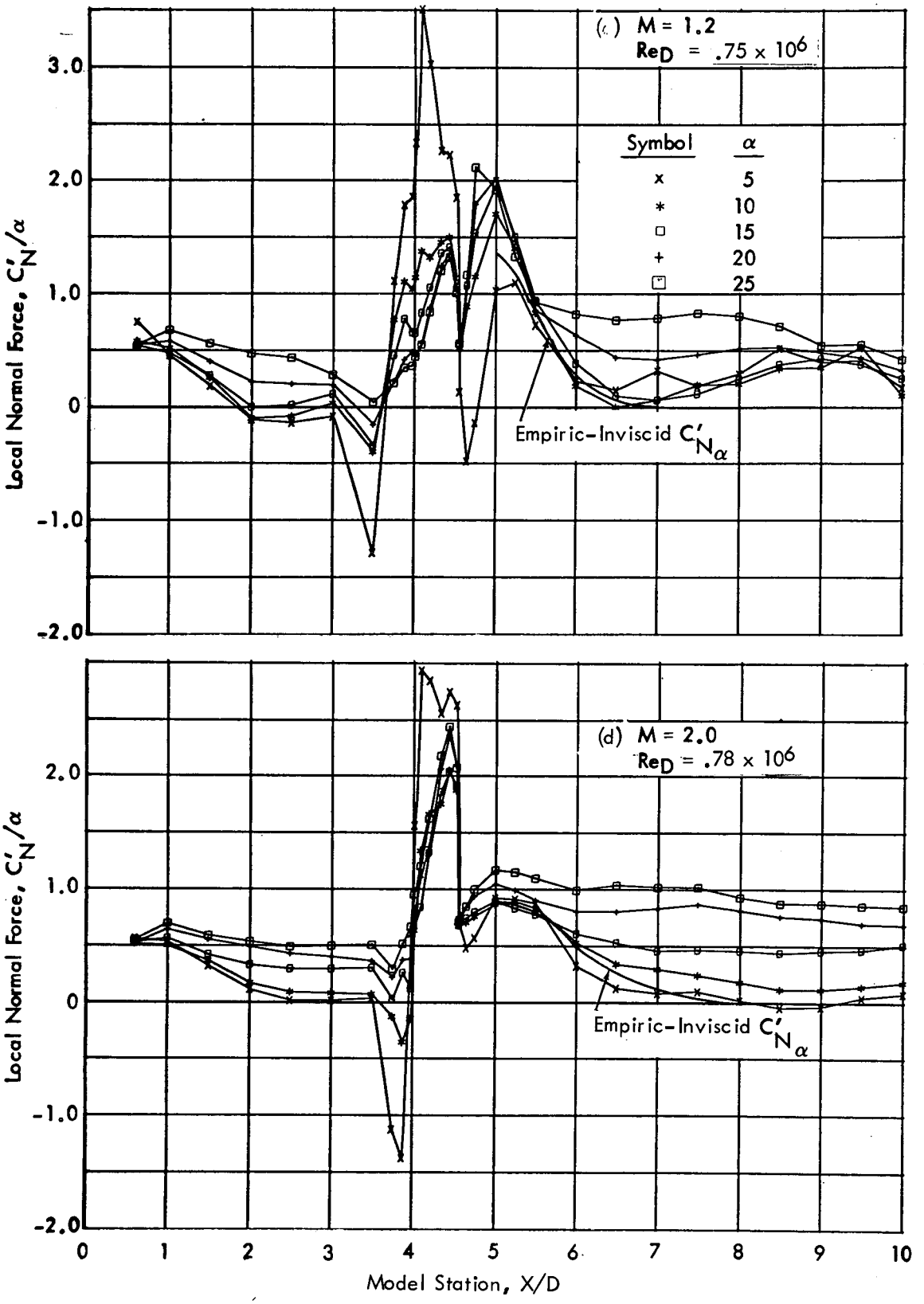

Figure 16. Local Normal Force Distributions, Ogive-Cylinder-Frustum-Cylinder (concluded)

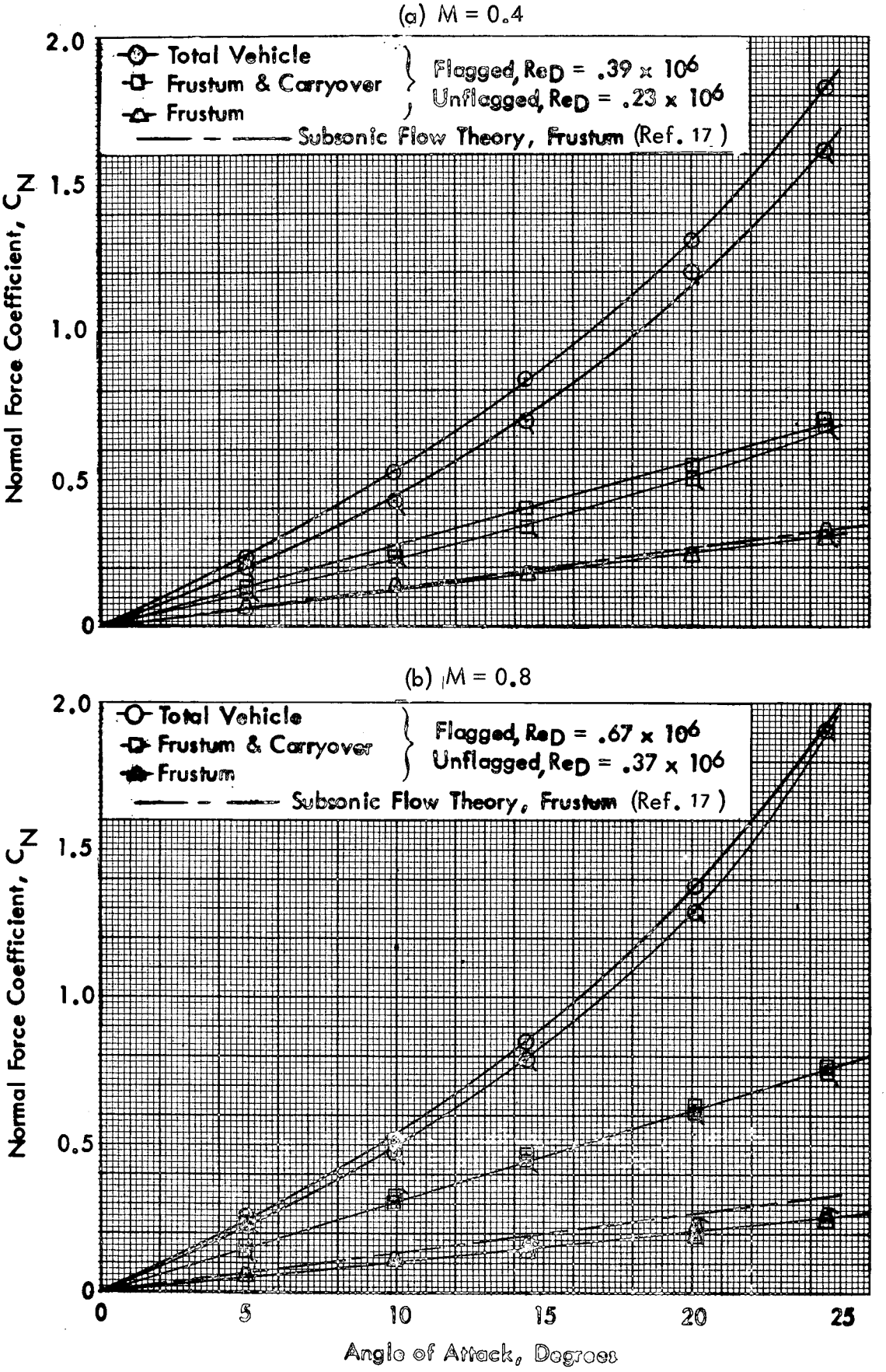

Figure 17. Component Normal Force Coefficients, O/C/F/C

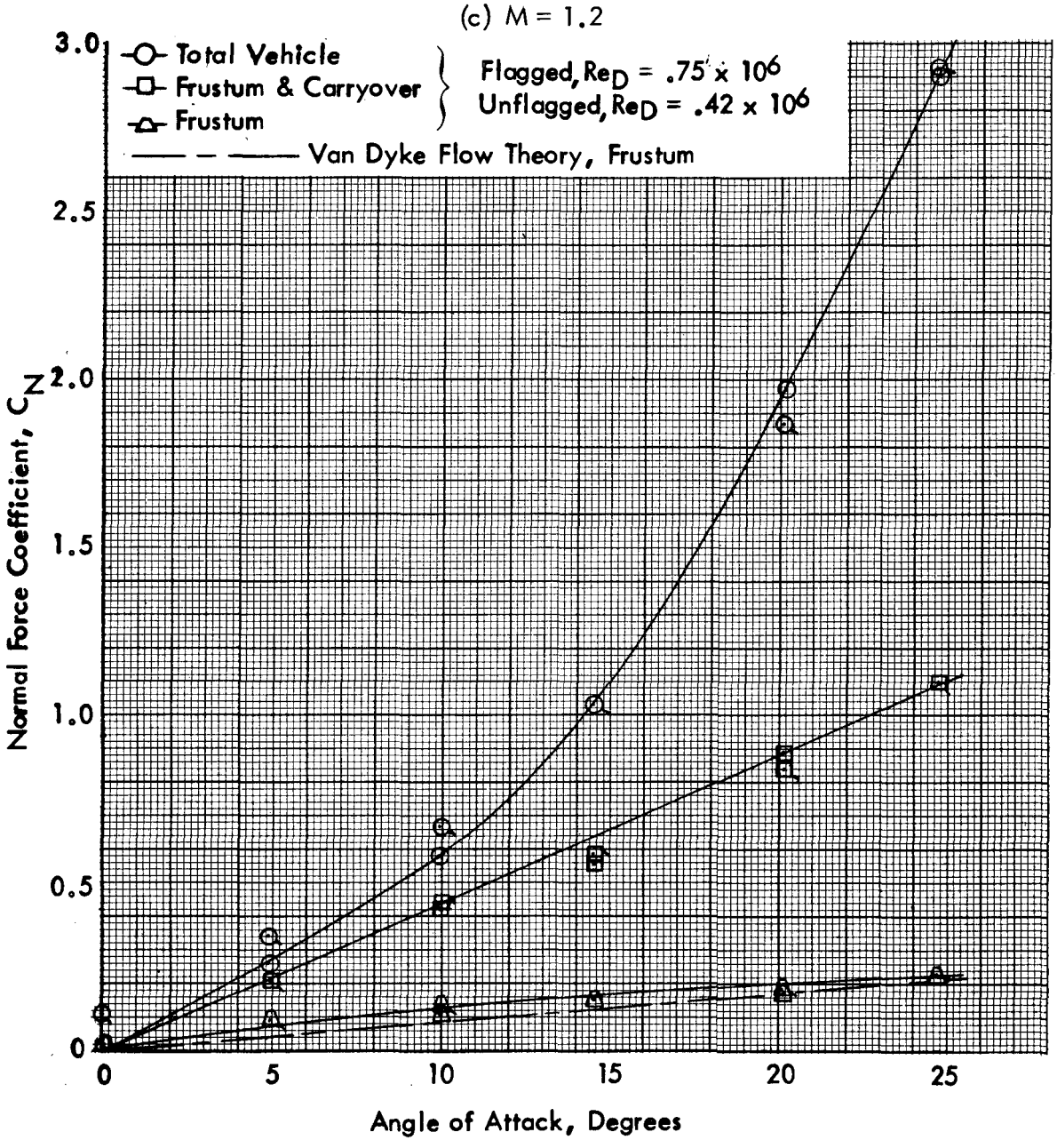

Figure 17. Component Normal Force Coefficients, O/C/F/C (continued)

(d) M = 2.0

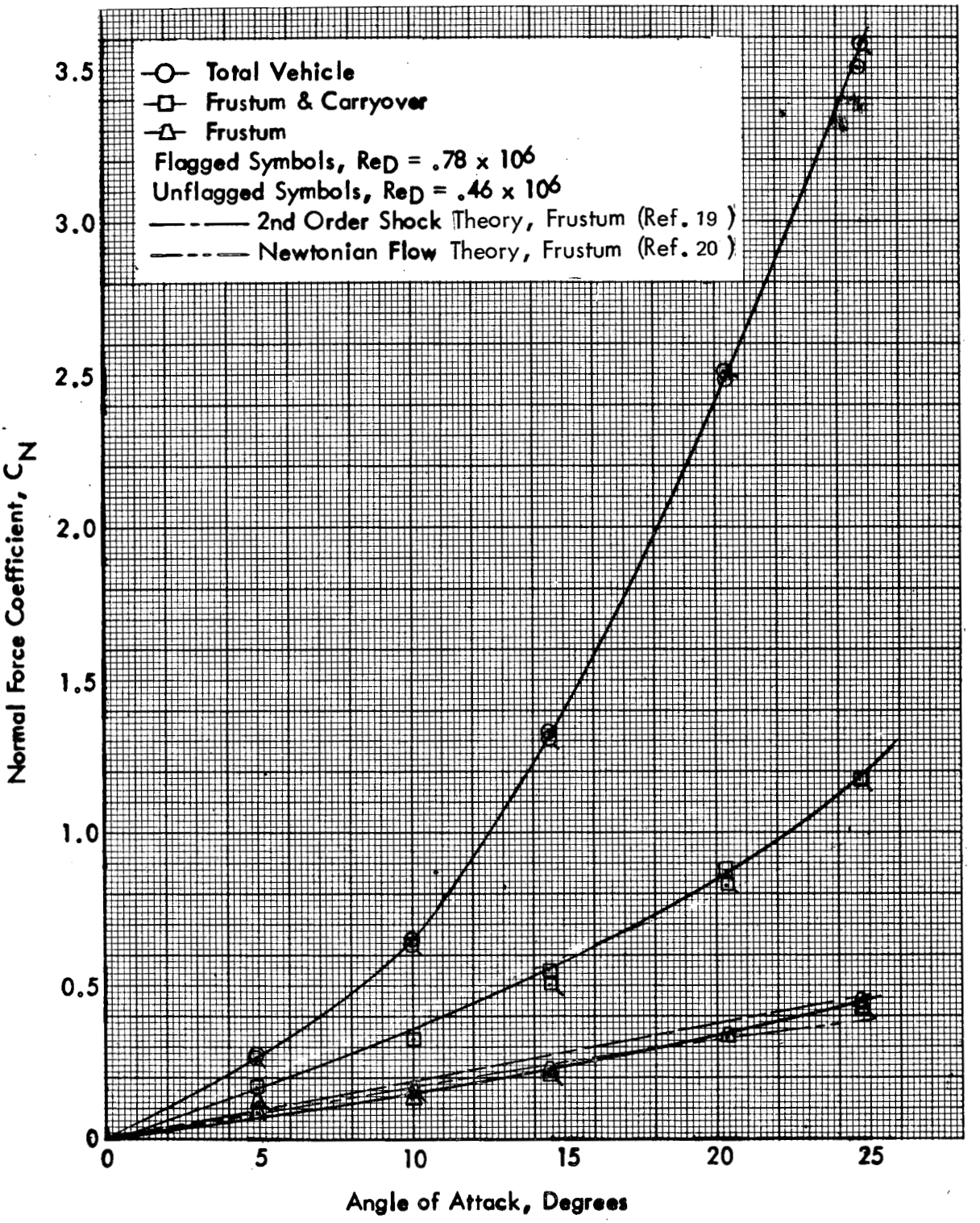

Figure 17. Component Normal Force Coefficients, O/C/F/C (concluded)

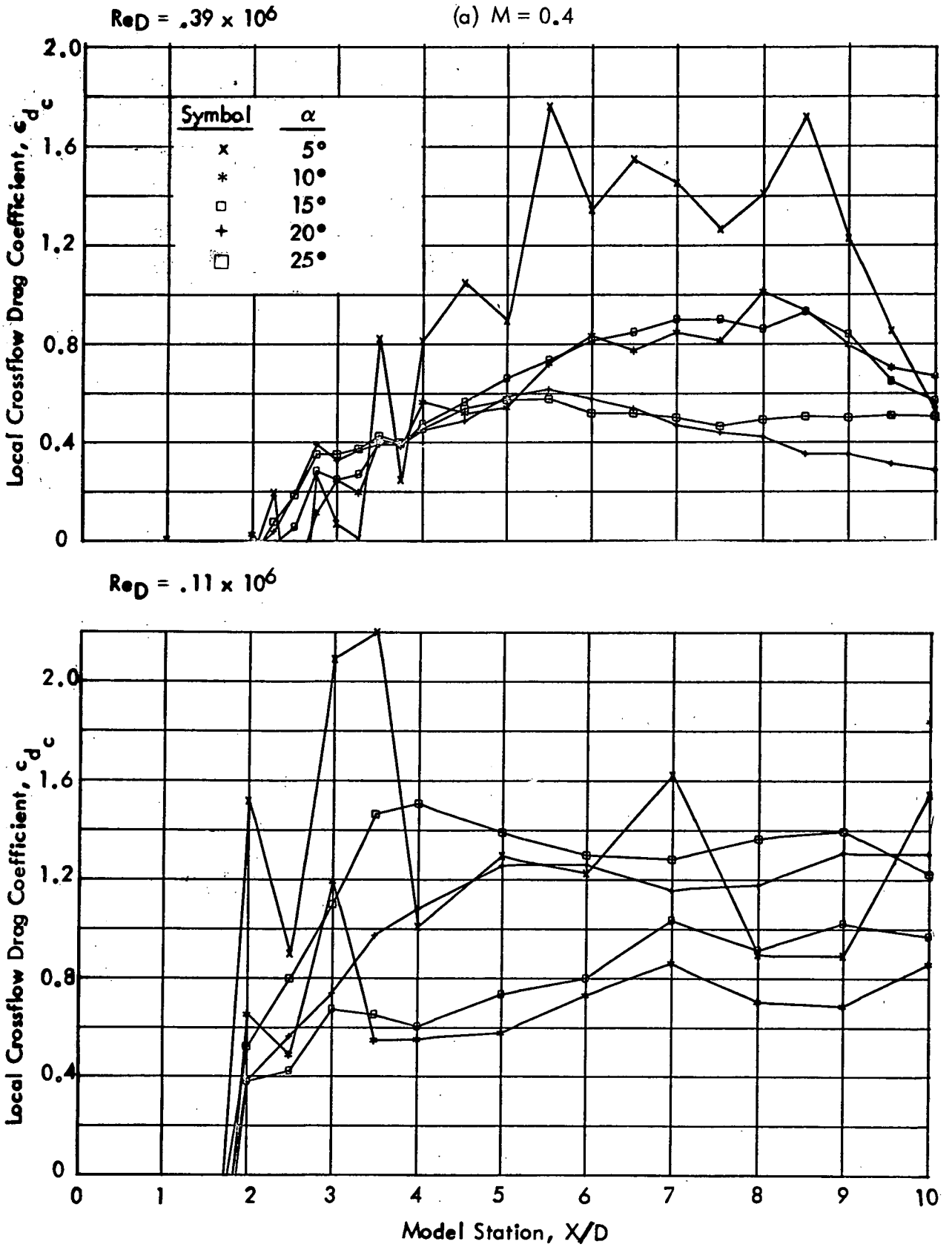

Figure 18. Local Crossflow Drag Coefficient vs. Model Station, Ogive-Cylinder Configuration

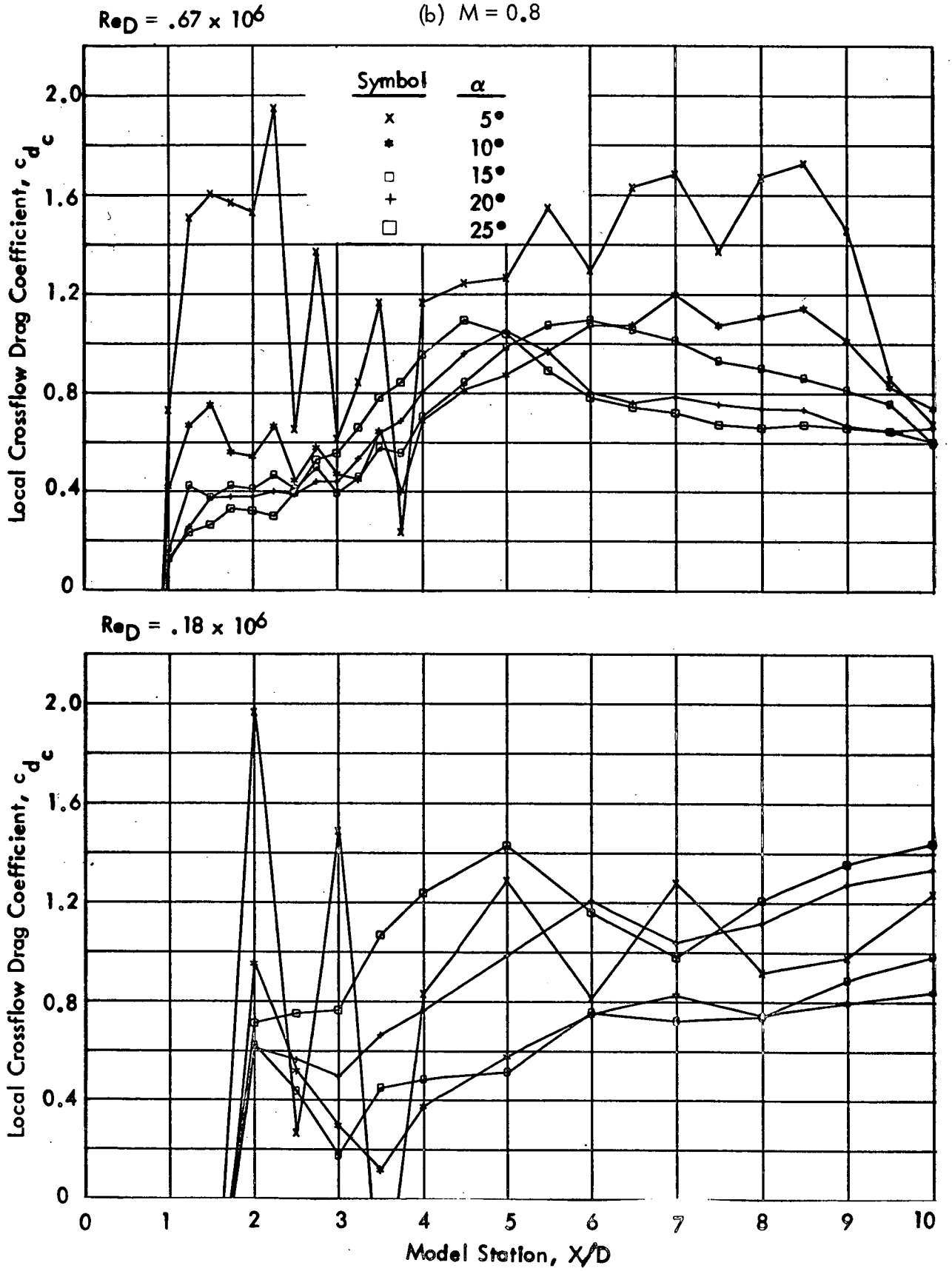

Figure 18. Local Crossflow Drag Coefficient vs. Model Station, Ogive-Cylinder Configuration (continued)

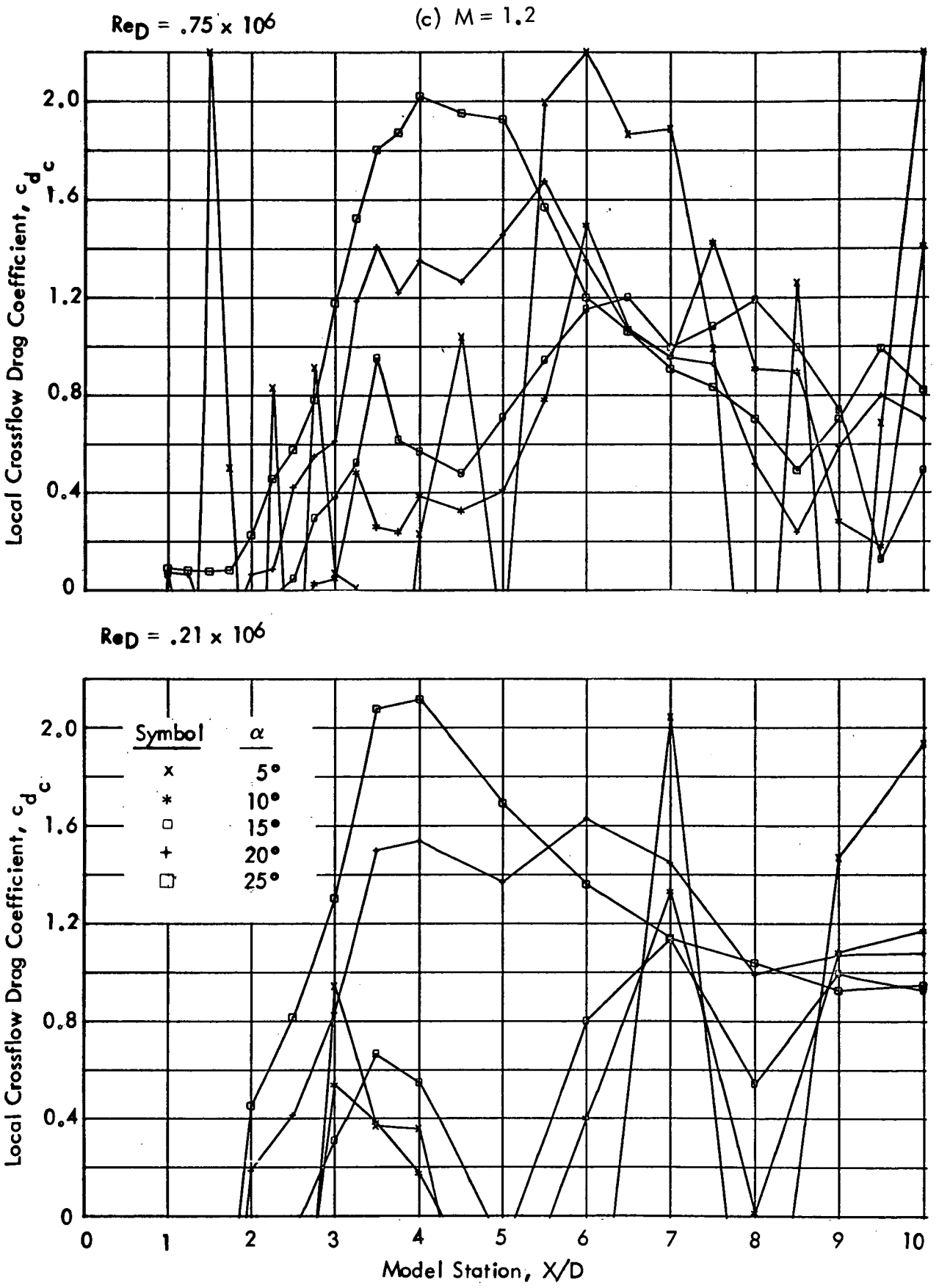

Figure 18. Local Crossflow Drag Coefficient vs. Model Station, Ogive-Cylinder Configuration (continued)

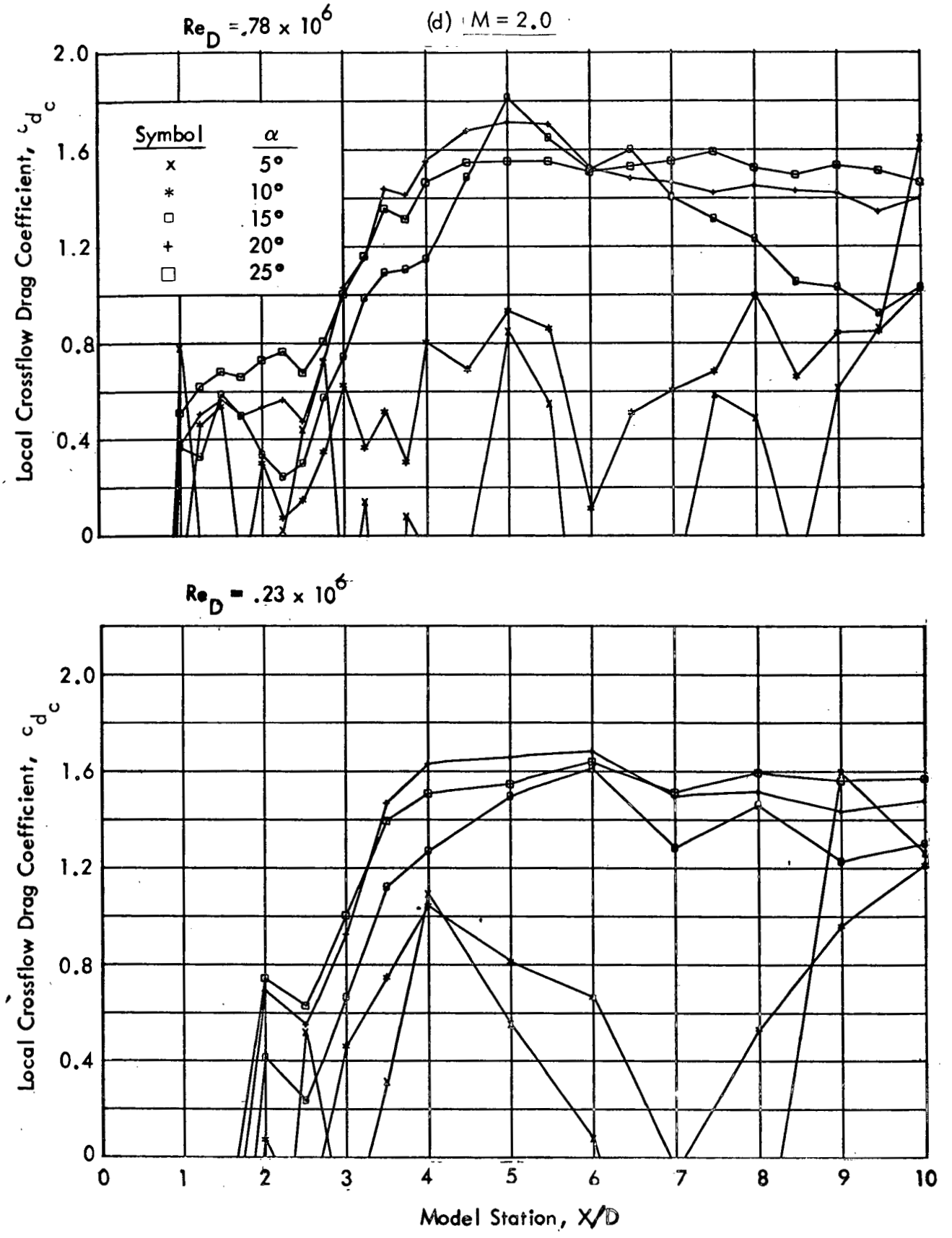

Figure 18. Local Crossflow Drag Coefficient vs. Model Station, Ogive-Cylinder Configuration (concluded)

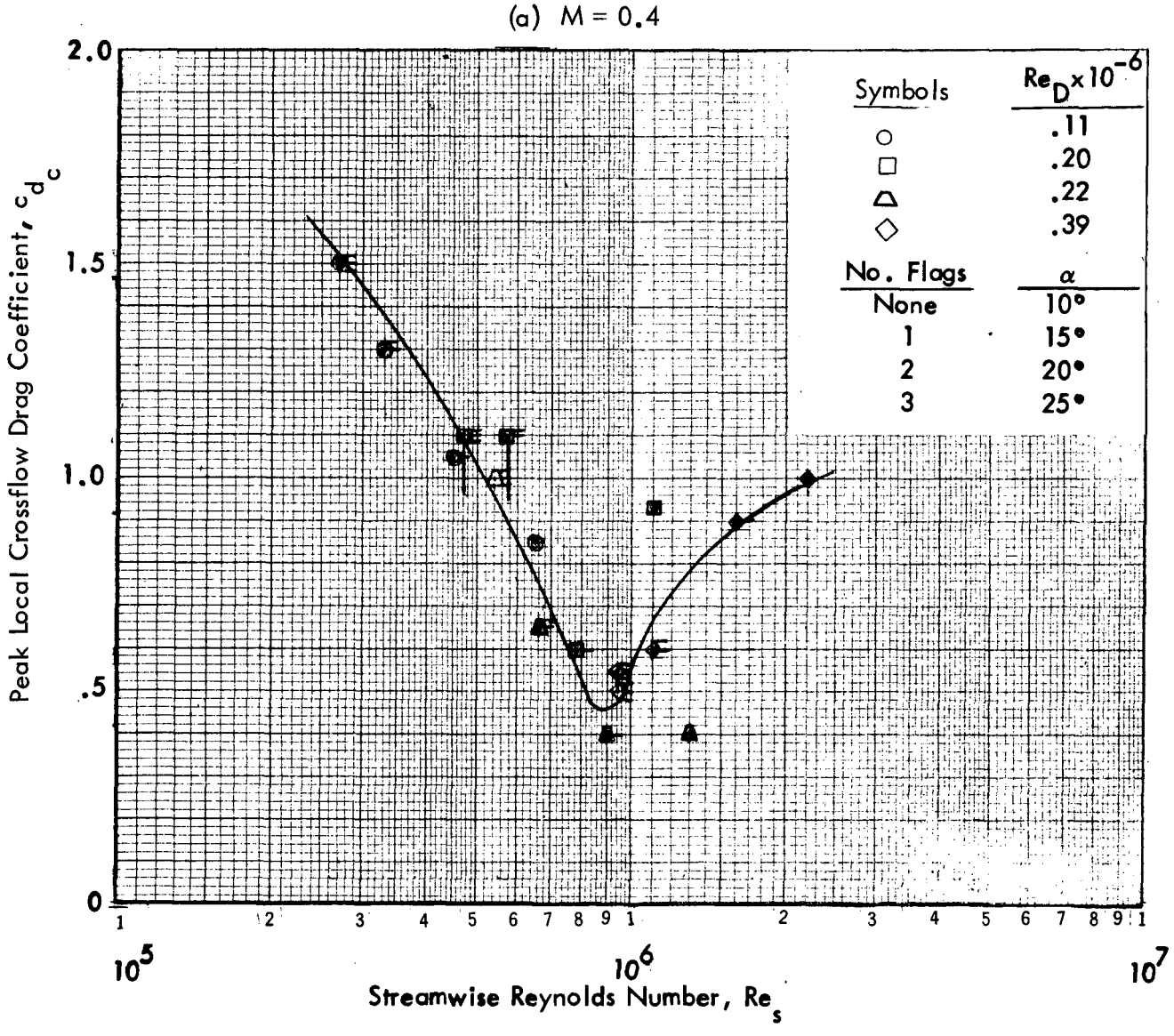

Figure 19. Correlation of Peak Local Crossflow Drag Coefficient, Ogive-Cylinder

(b) M = 0.8

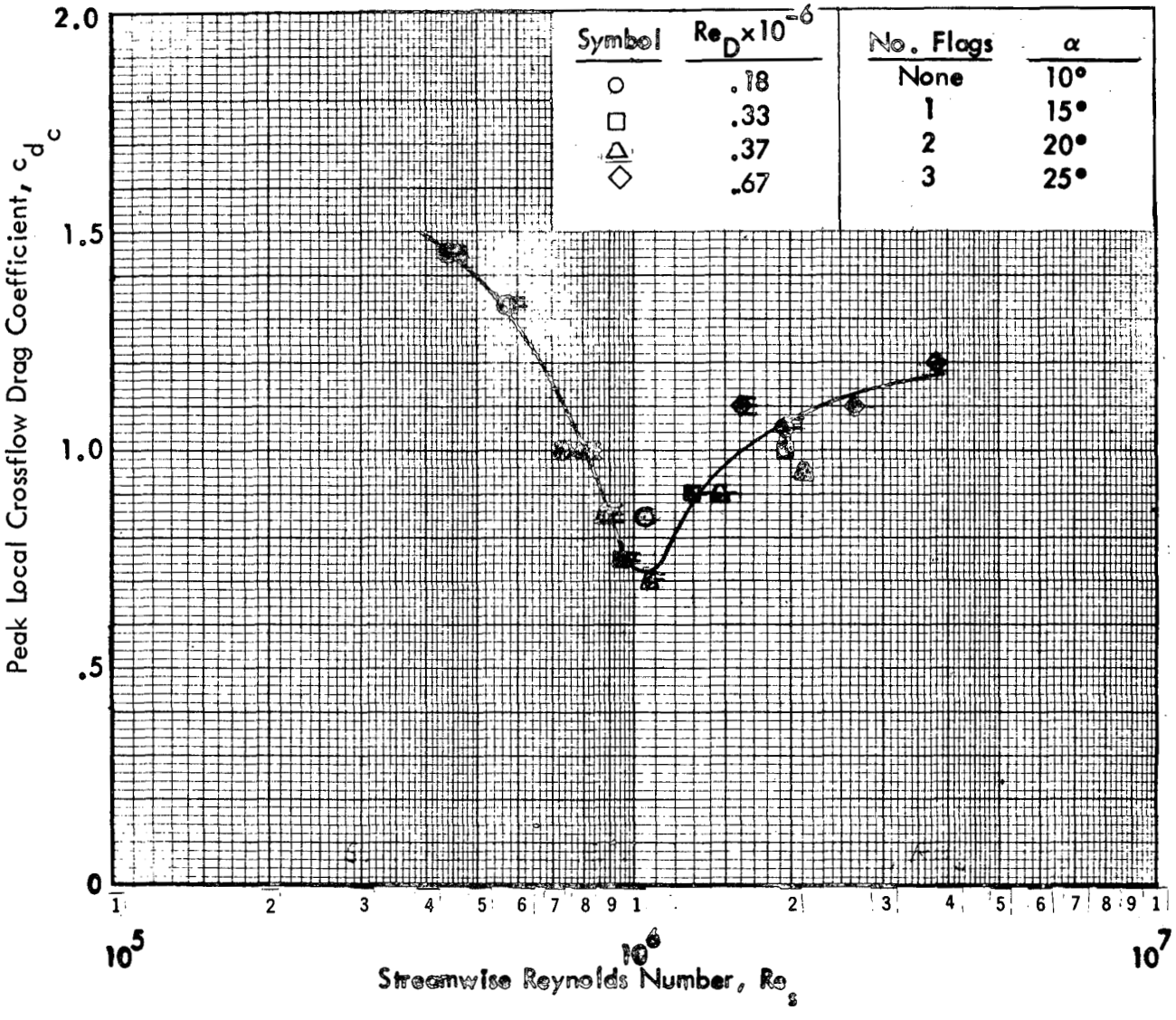

Figure 19. Correlation of Peak Local Crossflow Drag Coefficient, Ogive-Cylinder (concluded)

$Re_D \times 10^{-6}$

Sym.	M 0.4	0.8	1.2	1.96
△	.11	.18	.21	.23
◇	.20	.33	.38	.39
○	.23	.37	.42	.46
□	.39	.67	.75	.78

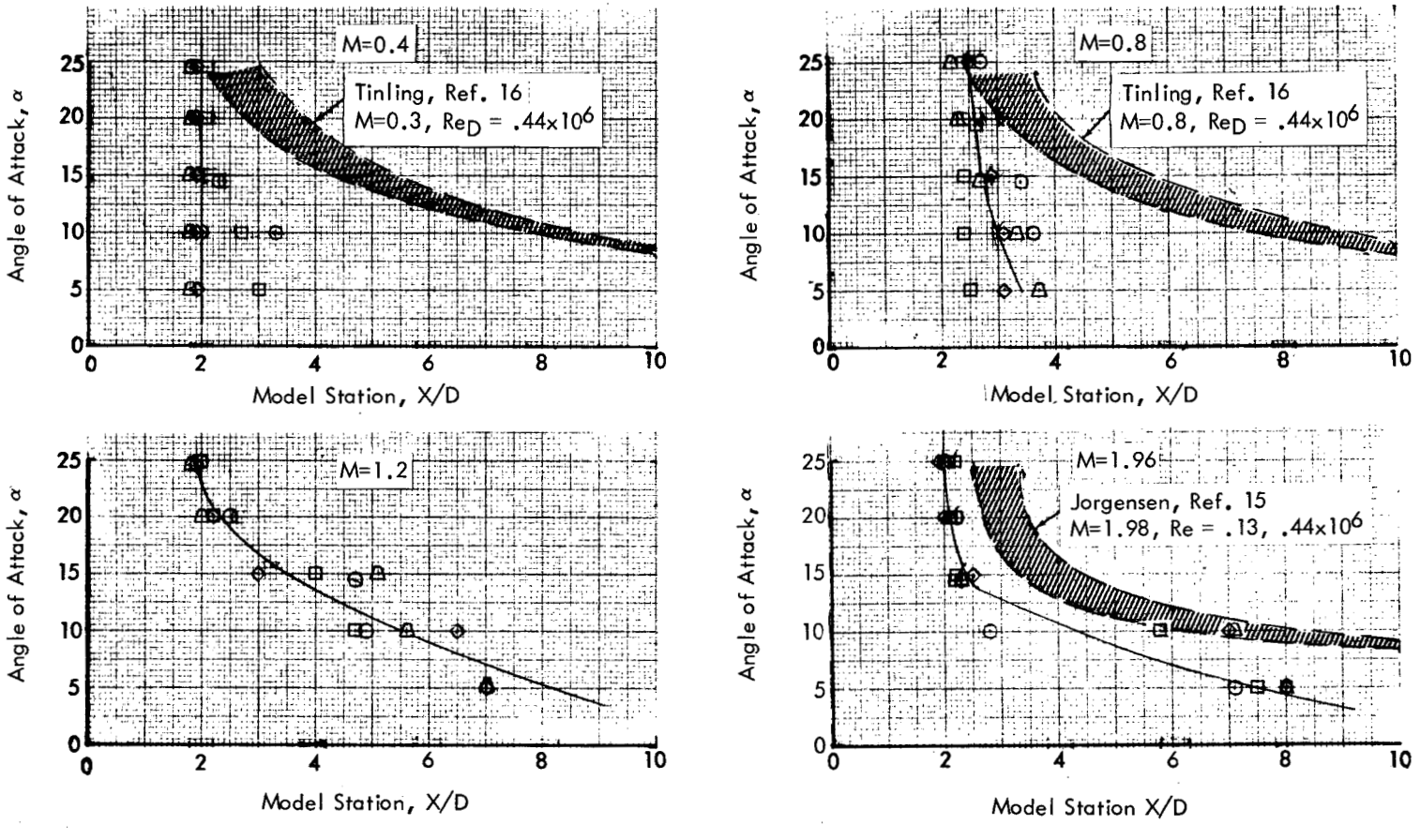

Figure 20. Axial Location of Initial Crossflow Separation, Ogive-Cylinder

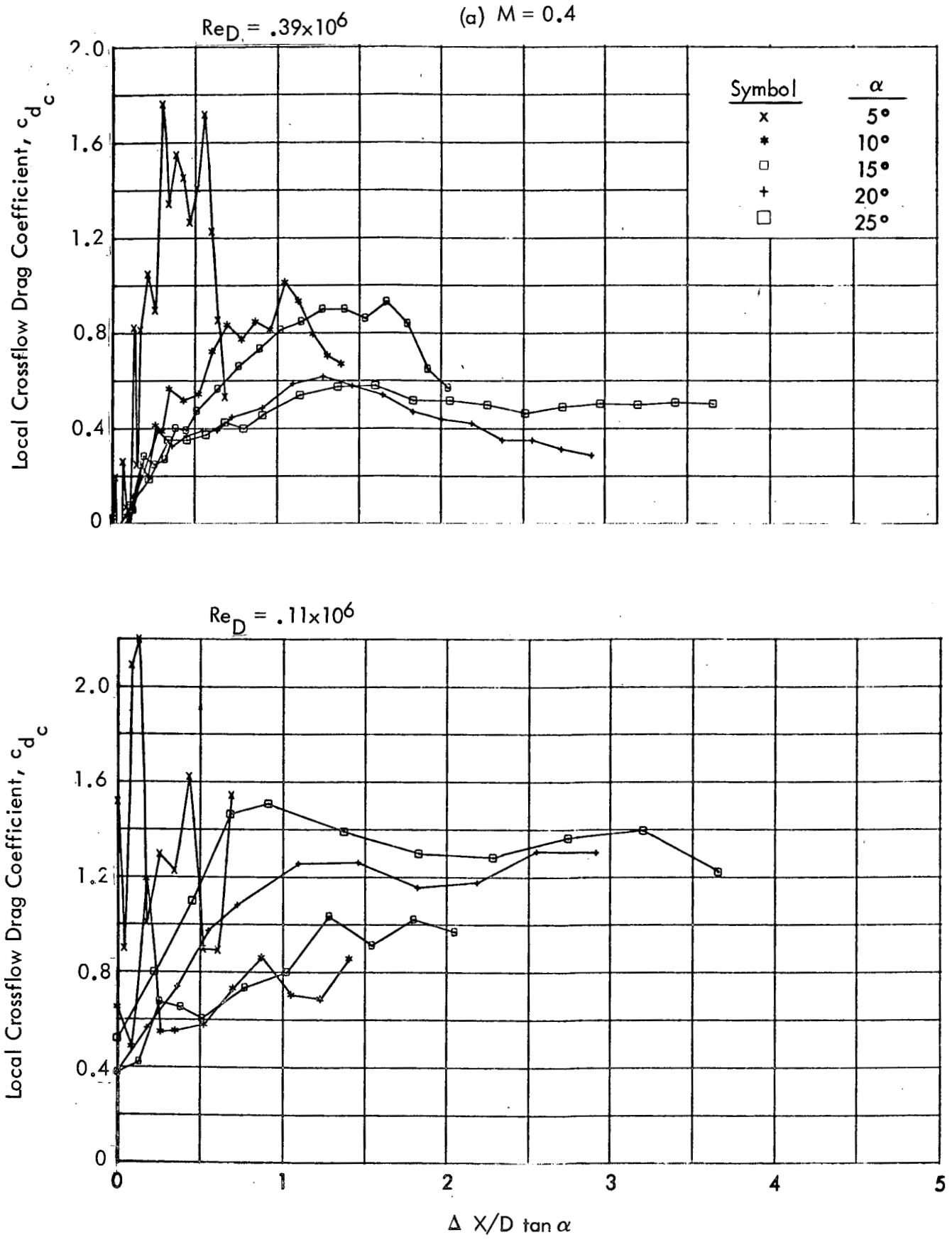

Figure 21. Local Crossflow Drag Coefficient vs Δ X/D tan α, Ogive-Cylinder Configuration

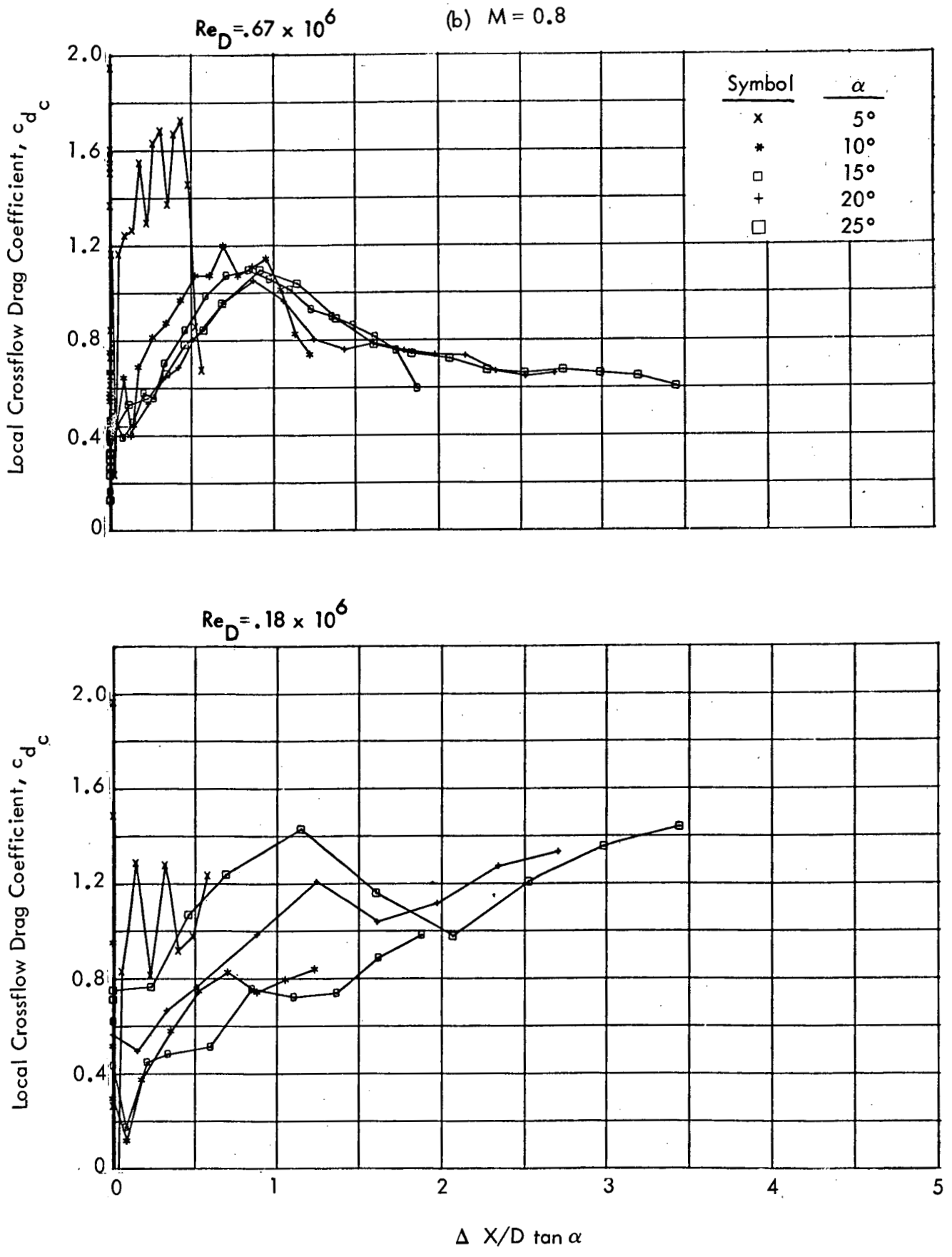

Figure 21. Local Crossflow Drag Coefficient vs Δ X/D tan α, Ogive-Cylinder Configuration (continued)

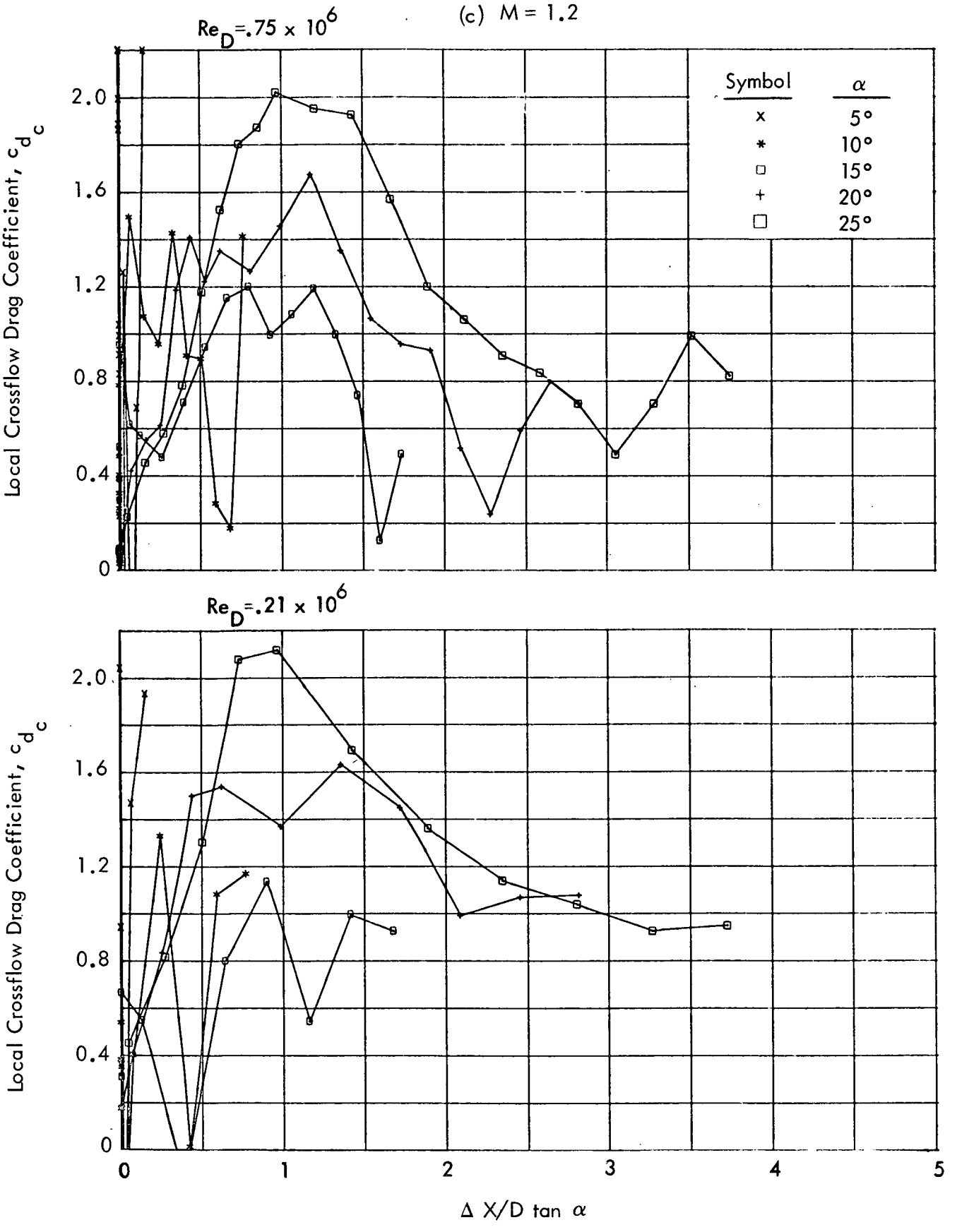

Figure 21. Local Crossflow Drag Coefficient vs Δ X/D tan α, Ogive-Cylinder Configuration (continued)

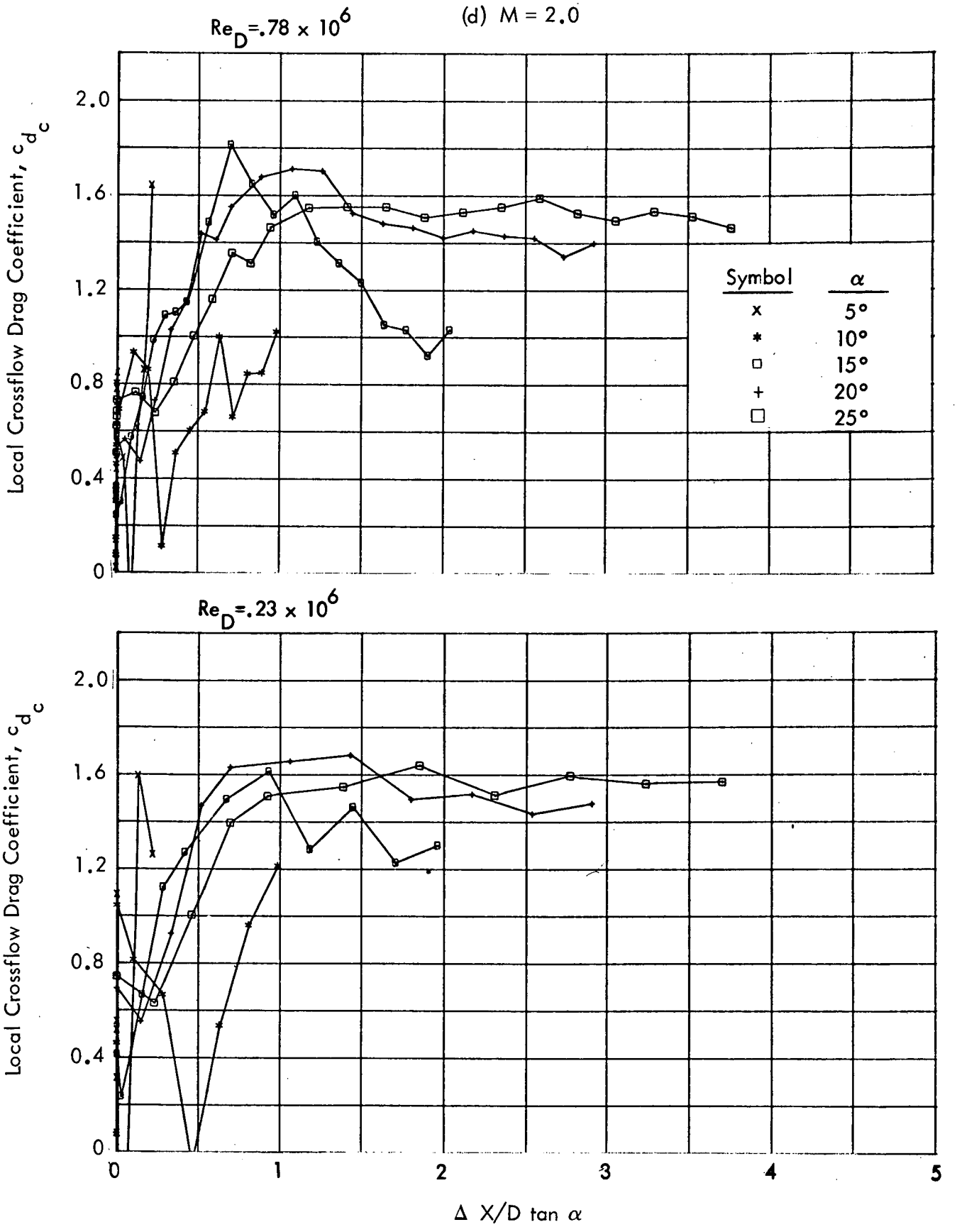

Figure 21. Local Crossflow Drag Coefficient vs Δ X/D tan α, Ogive-Cylinder Configuration (concluded)

(a) M = 0.4

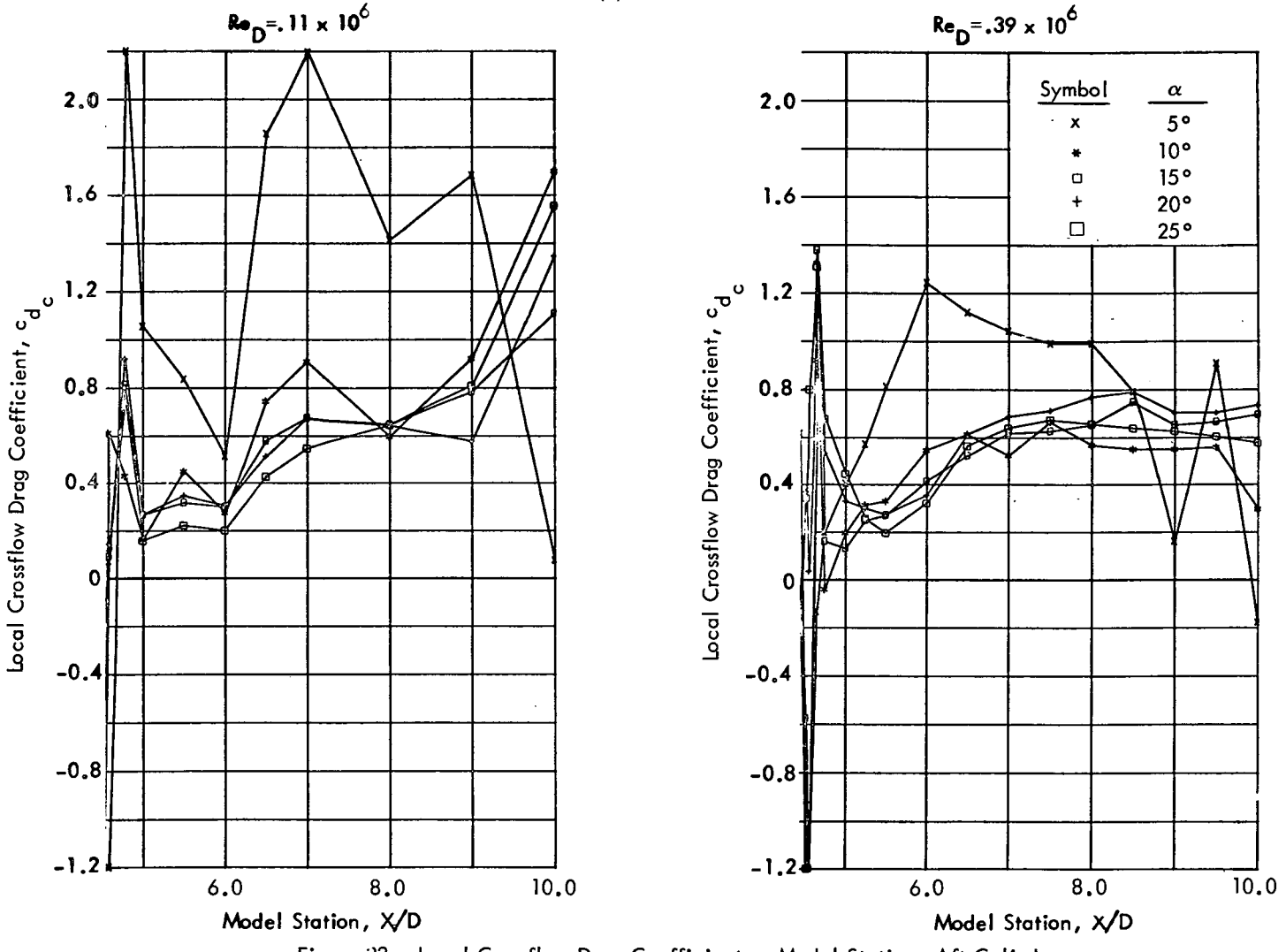

Figure 22. Local Crossflow Drag Coefficient vs Model Station, Aft Cylinder of O/C/F/C Configuration (Shee

(b) M = 0.8

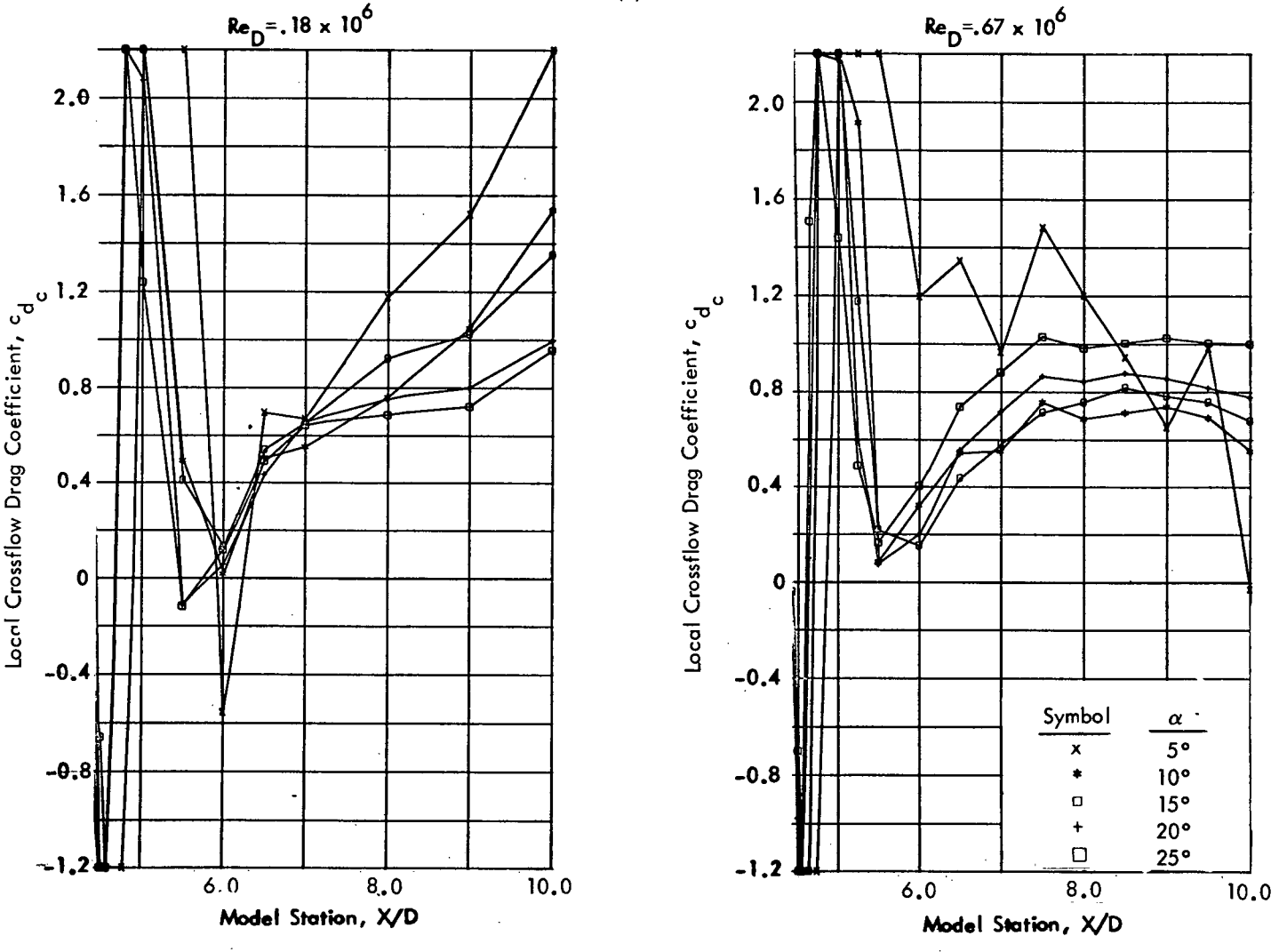

Figure 22. Local Crossflow Drag Coefficient vs Model Station, Aft Cylinder of O/C/F/C Configuration (continued)

(c) M = 1.2

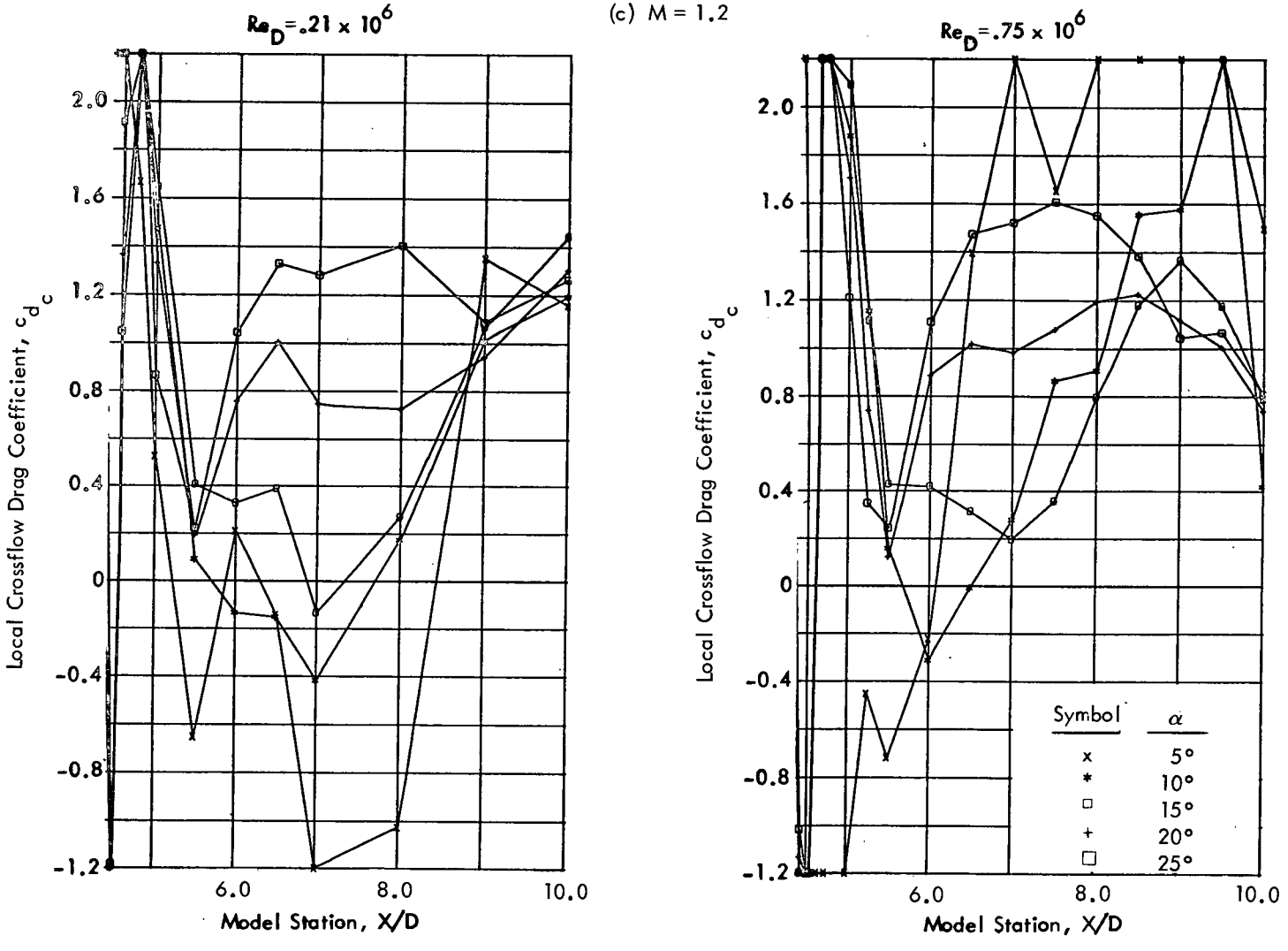

Figure 22. Local Crossflow Drag Coefficient vs Model Station, Aft Cylinder of O/C/F/C Configuration (continued)

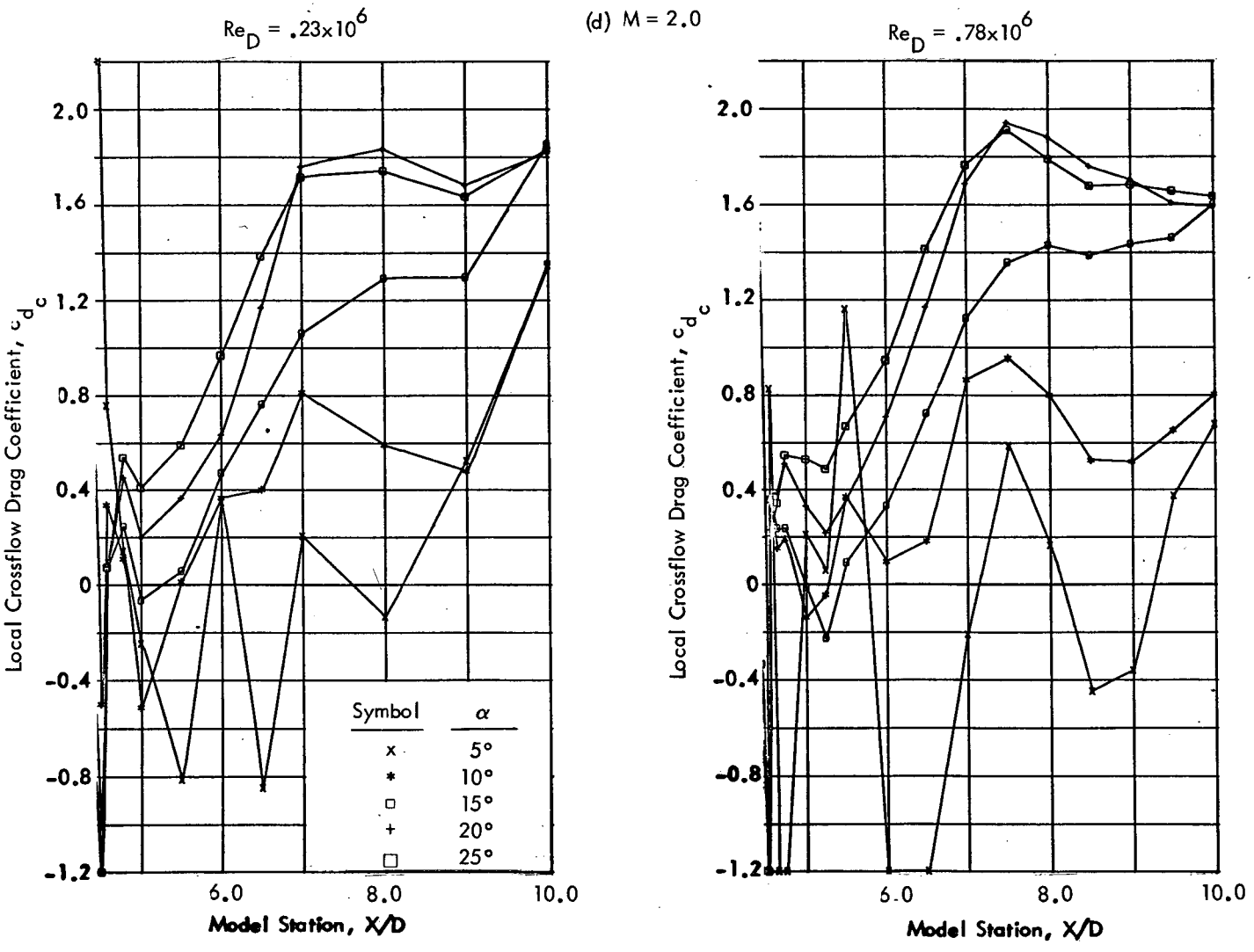

Figure 22. Local Crossflow Drag Coefficient vs Model Station, Aft Cylinder of O/C/F/C Configuration (concluded)

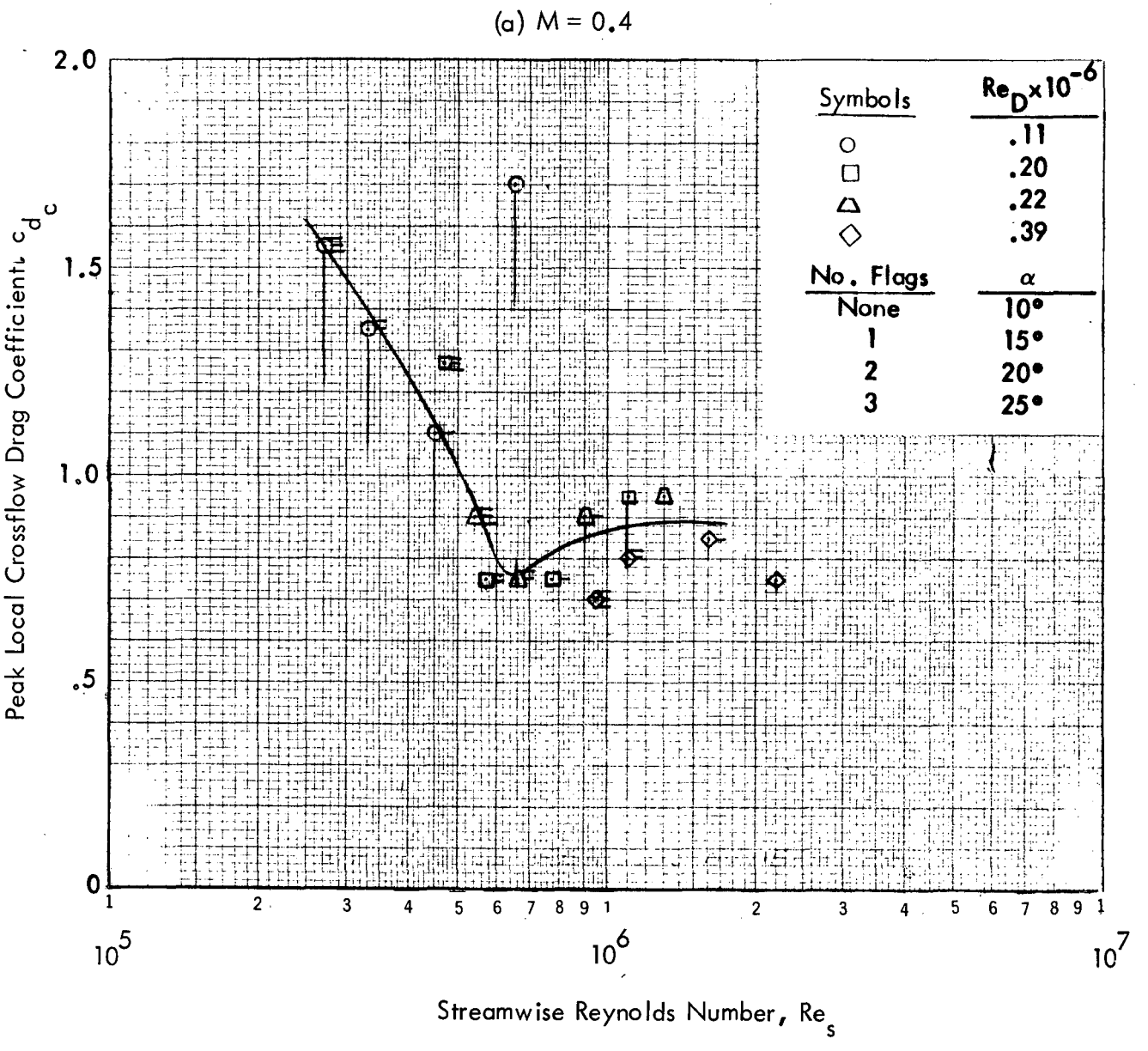

Figure 23. Correlation of Peak Local Crossflow Drag Coefficient, O/C/F/C Aft Cylinder

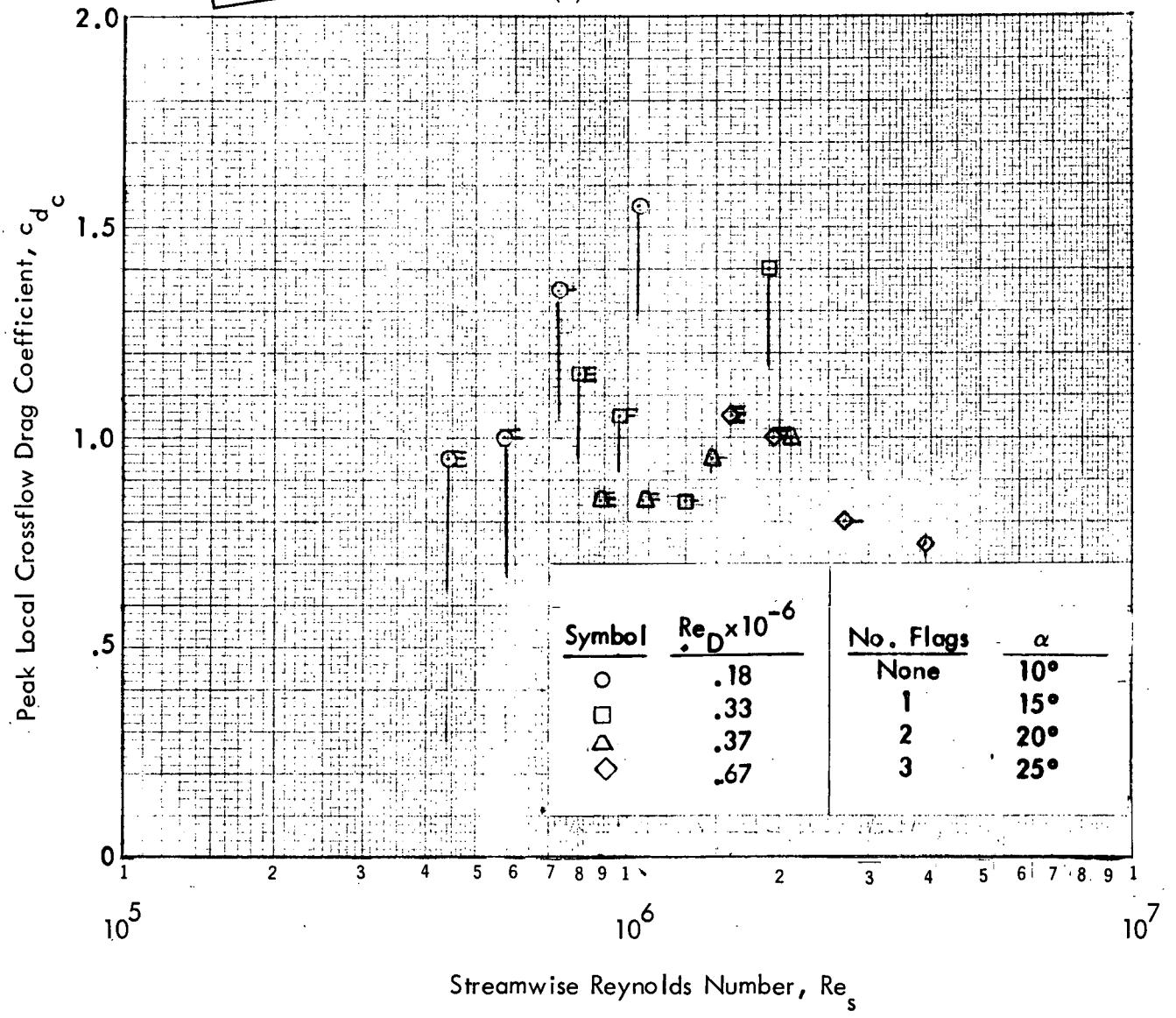

Figure 23. Correlation of Peak Local Crossflow Drag Coefficient, O/C/F/C Aft Cylinder (concluded)

$Re_D \times 10^{-6}$

Sym	M=.4	M=.8	M=1.2	M=1.96
△	.11	.18	.21	.23
◇	.20	.33	.38	.39
○	.23	.37	.42	.46
□	.39	.67	.75	.78

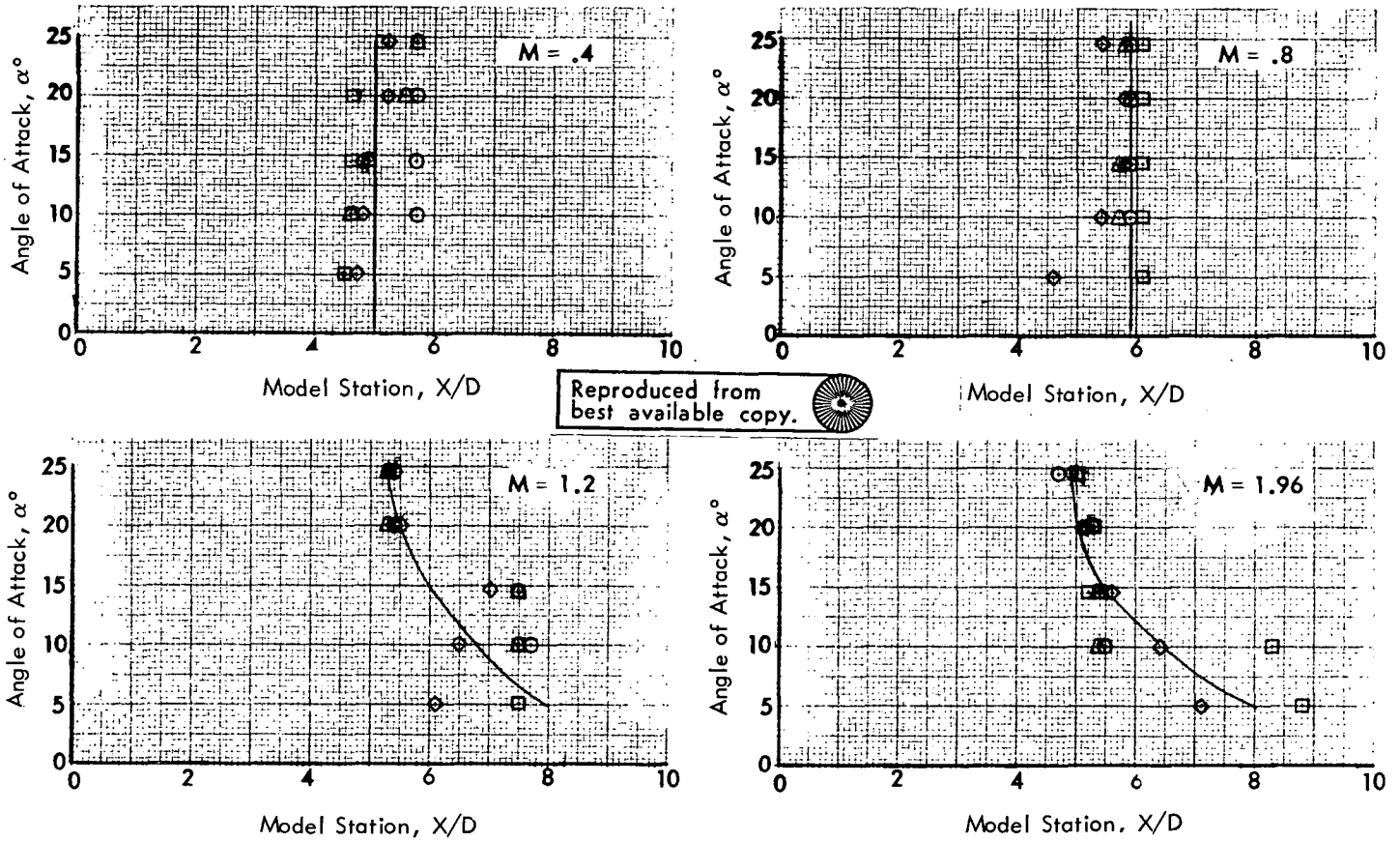

Figure 24. Axial Location of Initial Crossflow Separation, O/C/F/C Aft Cylinder

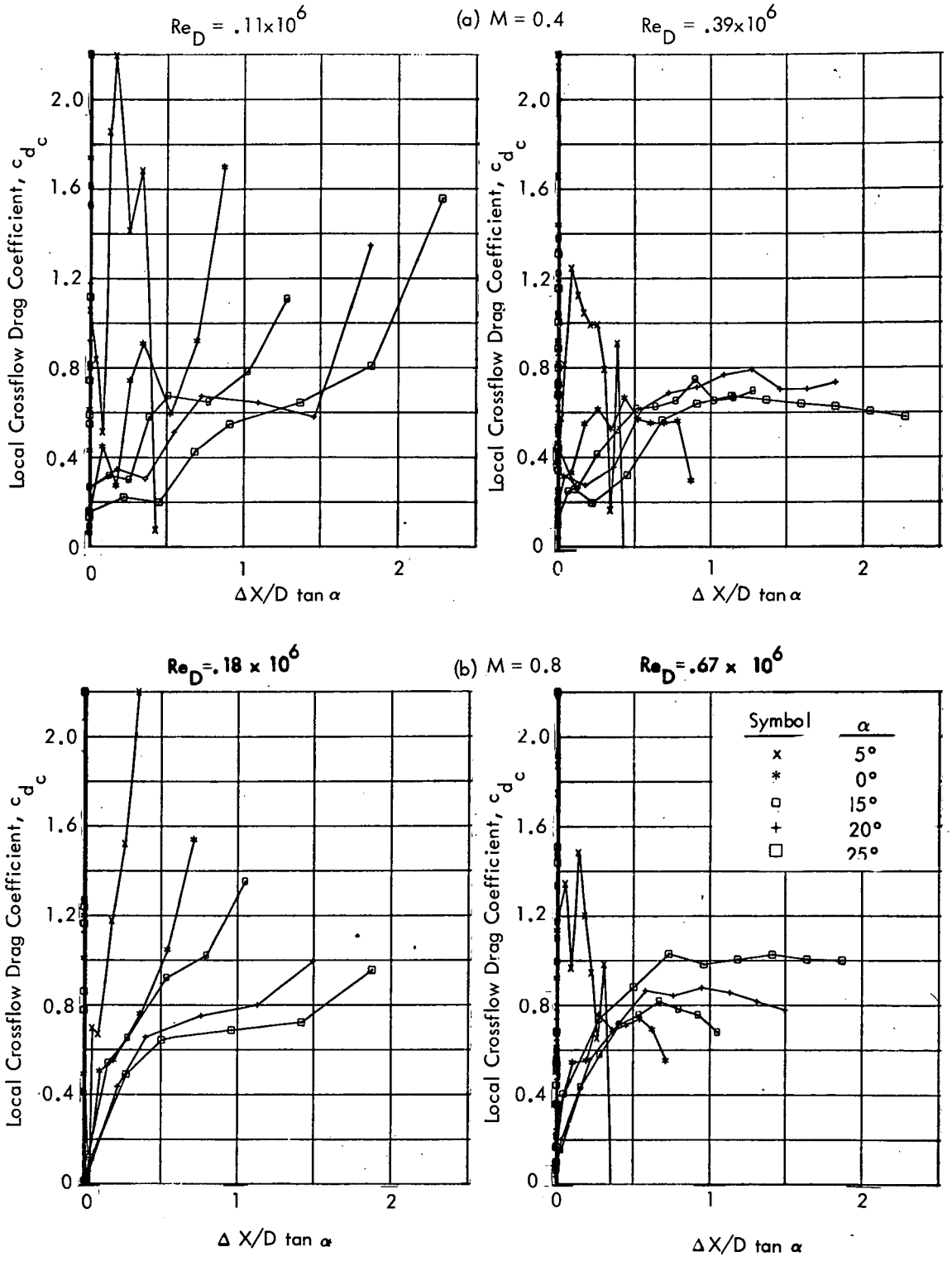

Figure 25. Local Crossflow Drag Coefficient vs Δ X/D tan α, O/C/F/C Aft Cylinder

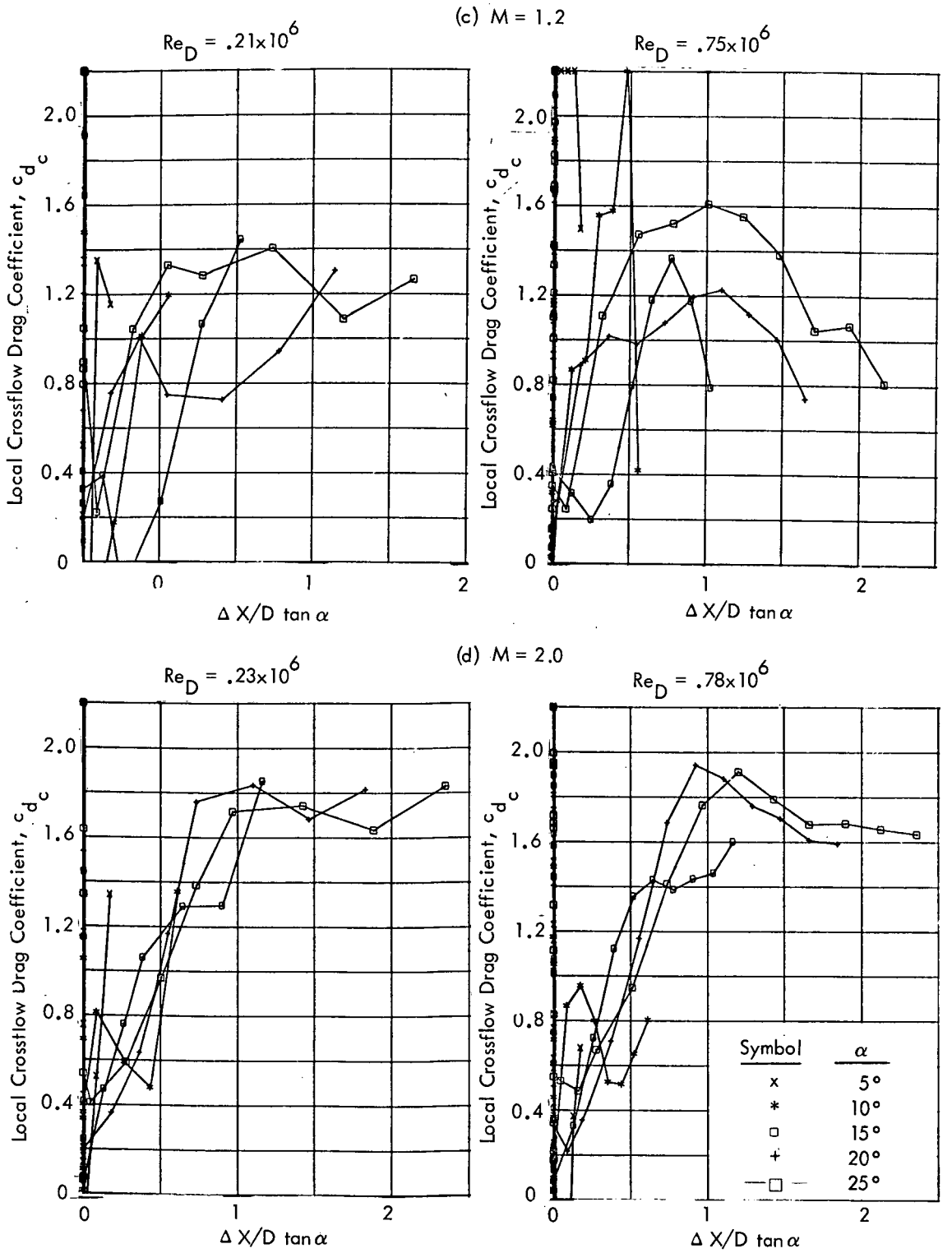

Figure 25. Local Crossflow Drag Coefficient vs Δ X/D tanα, O/C/F/C Aft Cylinder (concluded)

MSFC—RSA, Ala